

## 1

## General Properties of ZnO

In this chapter, crystal structure of ZnO encompassing lattice parameters, electronic band structure, mechanical properties, including elastic constants and piezoelectric constants, lattice dynamics, and vibrational processes, thermal properties, electrical properties, and low-field and high-field carrier transport is treated.

### 1.1

#### Crystal Structure

Most of the group II–VI binary compound semiconductors crystallize in either cubic zinc blende or hexagonal wurtzite (Wz) structure where each anion is surrounded by four cations at the corners of a tetrahedron, and vice versa. This tetrahedral coordination is typical of  $sp^3$  covalent bonding nature, but these materials also have a substantial ionic character that tends to increase the bandgap beyond the one expected from the covalent bonding. ZnO is a II–VI compound semiconductor whose ionicity resides at the borderline between the covalent and ionic semiconductors. The crystal structures shared by ZnO are *wurtzite* (B4), *zinc blende*<sup>1)</sup> (B3), and *rocksalt* (or Rochelle salt)<sup>2)</sup> (B1) as schematically shown in Figure 1.1. B1, B3, and B4 denote the *Strukturbericht*<sup>3)</sup> designations for the three phases. Under ambient conditions, the thermodynamically stable phase is that of wurtzite symmetry. The zinc blende ZnO structure can be stabilized only by growth on cubic substrates, and

- 1) The term zinc blende originated from compounds such as ZnS, which could be in cubic or hexagonal phase. But the term has been used ubiquitously for compound semiconductors with cubic symmetry. The correct term that should be used for the cubic phase of ZnO GaN is actually *sphalerite*. To be consistent with the diction throughout the literature even at the expense of bordering inaccuracy, the term zinc blende is used throughout this book.
- 2) Also called Seignette salt – named after Pier Seignette from La Rochelle, France, who first prepared potassium sodium tartrate tetrahydrate ( $KNaC_4H_4O_6 \cdot 4H_2O$ ) in 1675 and determined its structure.
- 3) *Strukturbericht*, the original crystallographic reports. From 1919 to 1939 (Vols 1–8), they were published in Germany. Since then, they have been published in the United States under the name *Structure Reports, Acta Crystallographica Section E*, by the International Union of Crystallography.

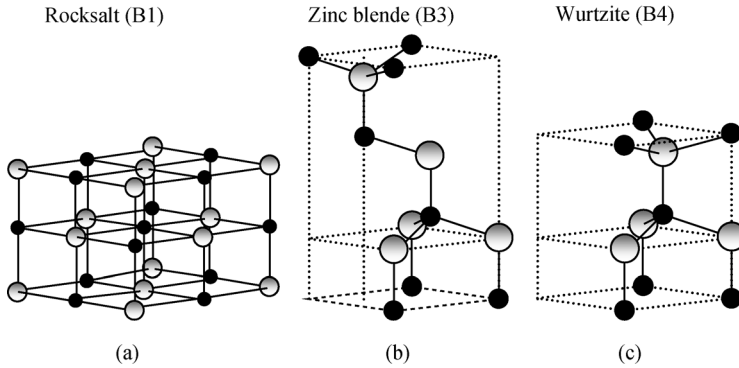


**Figure 1.1** Stick-and-ball representation of ZnO crystal structures: (a) cubic rocksalt (B1), (b) cubic zinc blende (B3), and (c) hexagonal wurtzite (B4). Shaded gray and black spheres denote Zn and O atoms, respectively.

the rocksalt or Rochelle salt (NaCl) structure may be obtained at relatively high pressures, as in the case of GaN.

The *wurtzite* structure has a hexagonal unit cell with two lattice parameters  $a$  and  $c$  in the ratio of  $c/a = \sqrt{8/3} = 1.633$  (in an ideal wurtzite structure) and belongs to the space group  $C_{6v}^4$  in the Schoenflies notation and  $P6_3mc$  in the Hermann–Mauguin notation. A schematic representation of the wurtzitic ZnO structure is shown in Figure 1.2. The structure is composed of two interpenetrating hexagonal close-packed (hcp) sublattices, each of which consists of one type of atom displaced with respect to each other along the threefold  $c$ -axis by the amount of  $u = 3/8 = 0.375$  (in an ideal wurtzite structure) in fractional coordinates. The internal parameter  $u$  is defined as the length of the bond parallel to the  $c$ -axis (anion–cation bond length or the

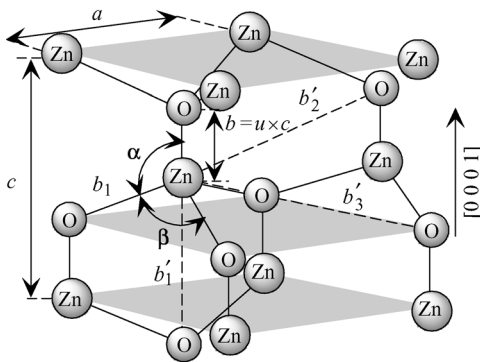


**Figure 1.2** Schematic representation of a wurtzitic ZnO structure with lattice constants  $a$  in the basal plane and  $c$  in the basal direction,  $u$  parameter, which is expressed as the bond length or the nearest-neighbor distance  $b$  divided by  $c$  (0.375 in ideal crystal),  $\alpha$  and  $\beta$  ( $109.47^\circ$  in ideal crystal) bond angles, and three types of second-nearest-neighbor distances  $b'_1$ ,  $b'_2$ , and  $b'_3$ .

nearest-neighbor distance) divided by the  $c$  lattice parameter. The basal plane lattice parameter (the edge length of the basal plane hexagon) is universally depicted by  $a$ ; the axial lattice parameter (unit cell height), perpendicular to the basal plane, is universally described by  $c$ . Each sublattice includes four atoms per unit cell, and every atom of one kind (group II atom) is surrounded by four atoms of the other kind (group VI), or vice versa, which are coordinated at the edges of a tetrahedron. The crystallographic vectors of wurtzite are  $\vec{a} = a(1/2, \sqrt{3}/2, 0)$ ,  $\vec{b} = a(1/2, -\sqrt{3}/2, 0)$ , and  $\vec{c} = a(0, 0, c/a)$ . In Cartesian coordinates, the basis atoms are  $(0, 0, 0)$ ,  $(0, 0, uc)$ ,  $a(1/2, \sqrt{3}/6, c/2a)$ , and  $a(1/2, \sqrt{3}/6, [u + 1/2]c/a)$ .

In a real ZnO crystal, the wurtzite structure deviates from the ideal arrangement, by changing the  $c/a$  ratio or the  $u$  value. The experimentally observed  $c/a$  ratios are smaller than ideal, as in the case of GaN, where it has been postulated that not being so would lead to zinc blende phase [1]. It should be pointed out that a strong correlation exists between the  $c/a$  ratio and the  $u$  parameter in that when the  $c/a$  ratio decreases, the  $u$  parameter increases in such a way that those four tetrahedral distances remain nearly constant through a distortion of tetrahedral angles due to long-range polar interactions. These two slightly different bond lengths will be equal if the following relation holds:

$$u = \left(\frac{1}{3}\right) \left(\frac{a^2}{c^2}\right) + \frac{1}{4}. \quad (1.1)$$

The nearest-neighbor bond lengths along the  $c$ -direction (expressed as  $b$ ) and off  $c$ -axis (expressed as  $b_1$ ) can be calculated as

$$b = cu \quad \text{and} \quad b_1 = \sqrt{\frac{1}{3}a^2 + \left(\frac{1}{2} - u\right)^2 c^2}. \quad (1.2)$$

In addition to the nearest neighbors, there are three types of second-nearest neighbors designated as  $b'_1$  (one along the  $c$ -direction),  $b'_2$  (six of them), and  $b'_3$  (three of them) with the bond lengths [2]

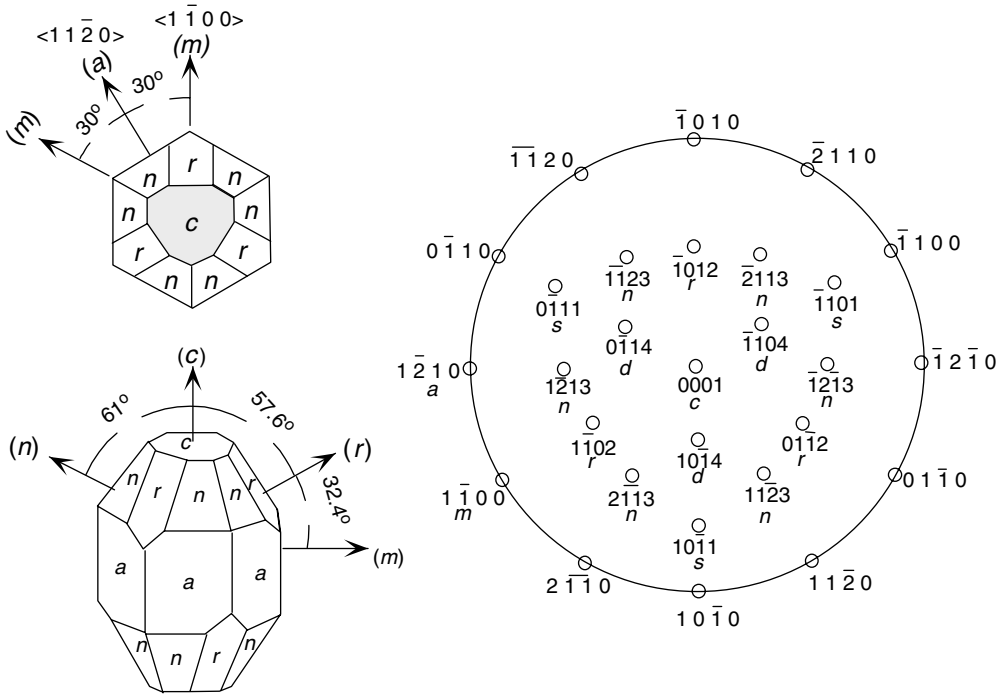
$$b'_1 = c(1-u), \quad b'_2 = \sqrt{a^2 + (uc)^2}, \quad \text{and} \quad b'_3 = \sqrt{\frac{4}{3}a^2 + c^2 \left(\frac{1}{2} - u\right)^2}. \quad (1.3)$$

The bond angles,  $\alpha$  and  $\beta$ , are given by [2]

$$\alpha = \pi/2 + \arccos \left[ \left( \sqrt{1 + 3(c/a)^2(-u + 1/2)^2} \right)^{-1} \right], \quad (1.4)$$

$$\beta = 2\arcsin \left[ \left( \sqrt{4/3 + 4(c/a)^2(-u + 1/2)^2} \right)^{-1} \right].$$

The lattice parameters are commonly measured at room temperature by X-ray diffraction (XRD), which happens to be the most accurate one, using the Bragg law. In ternary compounds, the technique is also used for determining the composition;



Common crystallographic planes in sapphire			Angles between common planes		
Plane name	Miller index	<i>d</i> spacing			
<i>a</i>	(11 $\bar{2}$ 0)	2.379 Å	(0001) ^ (1 $\bar{1}$ 02)	<i>c</i> ^ <i>r</i>	57° 35'
<i>m</i>	(10 $\bar{1}$ 0)	1.375 Å	(0001) ^ (11 $\bar{2}$ 3)	<i>c</i> ^ <i>n</i>	61° 11'
<i>c</i>	(0001)	2.165 Å	(0001) ^ (10 $\bar{1}$ 1)	<i>c</i> ^ <i>s</i>	72° 23'
<i>r</i>	(1 $\bar{1}$ 02)	1.740 Å	(0001) ^ (11 $\bar{2}$ 1)	<i>c</i> ^	79° 37'
<i>n</i>	(11 $\bar{2}$ 3)	1.147 Å	(0001) ^ (1120)	<i>c</i> ^ <i>a</i>	90° 00'
<i>s</i>	(10 $\bar{1}$ 1)	1.961 Å	(0001) ^ (10 $\bar{1}$ 0)	<i>c</i> ^ <i>m</i>	90° 00'
			(1120) ^ (10 $\bar{1}$ 0)	<i>c</i> ^ <i>m</i>	30° 00'

Figure 1.3 Labeling of planes in hexagonal symmetry (for sapphire).

however, strain and relevant issues must be taken into consideration as the samples are in the form of epitaxial layers on foreign substrates. The accuracy of the X-ray diffraction and less than accurate knowledge of elastic parameters together allow determination of the composition to only within about 1% molar fraction. In addition to composition, the lattice parameter can be affected by free charge, impurities, stress, and temperature [3]. Because the *c/a* ratio also correlates with the difference of the electronegativities of the two constituents, components with the greatest differences show largest departure from the ideal *c/a* ratio [4].

The nomenclature for various commonly used planes of hexagonal semiconductors in two- and three-dimensional versions is presented in Figures 1.3 and 1.4. The Wz ZnO lacks an inversion plane perpendicular to the *c*-axis; thus, surfaces have either a group II element (Zn, Cd, or Mg) polarity (referred to as Zn polarity) with a

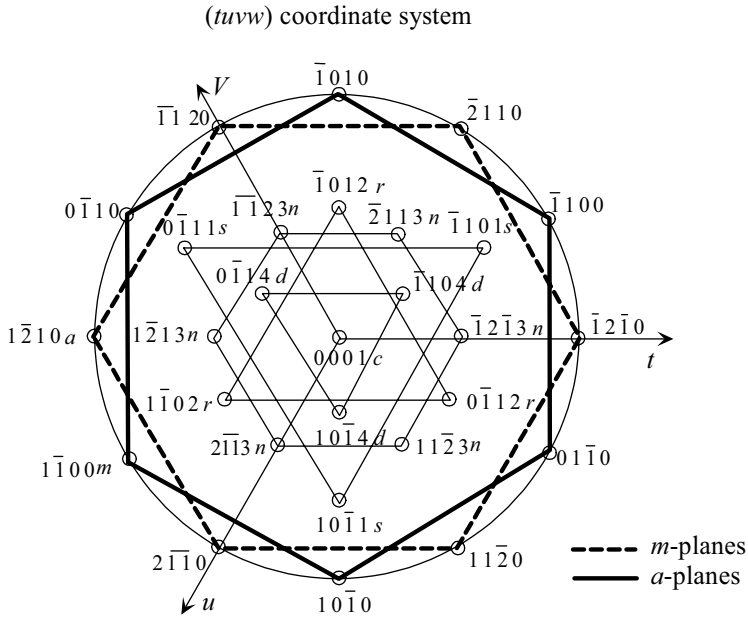


**Figure 1.4** A magnified view of labeling of planes in hexagonal symmetry in the (*uvw*) coordinate system with *w* representing the unit vector in the *c*-direction. The lines simply show the symmetry only. If the lines connecting *m*-points among each other and *a*-points among each other were to be interpreted as the projection of those planes on the *c*-plane, the roles would be switched in that the lines connecting the *m*-points would actually represent the *a*-planes and lines connecting the *a*-points would actually represent the *m*-planes, which are normal to the plane of the page.

designation of (0001) or (0001)*A* plane or an *O* polarity with a designation of (000  $\bar{1}$ ) or (000  $\bar{1}$ )*B* plane. The distinction between these two directions is essential due to polarization charge. Three surfaces and directions are of special importance, which are (0001), (11  $\bar{2}$ 0), and (1  $\bar{1}$ 00) planes and the directions associated with them,  $\langle 0001 \rangle$ ,  $\langle 11 \bar{2}0 \rangle$ , and  $\langle 1 \bar{1}00 \rangle$ , as shown in Figure 1.5. The (0001), or the basal plane, is the most commonly used surface for growth. The other two are important in that they represent the primary directions employed in reflection high-energy electron diffraction (RHEED) observations in MBE growth, apart from being perpendicular to one another.

The *zinc blende* ZnO structure is metastable and can be stabilized only by heteroepitaxial growth on cubic substrates, such as ZnS [5], GaAs/ZnS [6], and Pt/Ti/SiO<sub>2</sub>/Si [7], reflecting topological compatibility to overcome the intrinsic tendency of forming wurtzite phase. In the case of highly mismatched substrates, there is usually a certain amount of zinc blende phase of ZnO separated by crystallographic defects from the wurtzite phase. The symmetry of the zinc blende structure is given by space group  $F43m$  in the Hermann–Mauguin notation and  $T_d^2$  in the Schoenflies notation and is composed of two interpenetrating face-centered cubic (fcc) sublattices shifted along the body diagonal by one-quarter of the length of

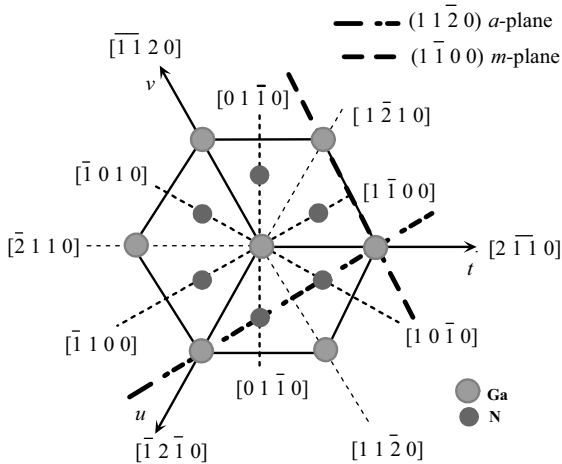


**Figure 1.5** Orientations that are commonly used in wurtzite phase, namely, the  $(1\ 1\ \bar{2}\ 0)$  and  $(1\ \bar{1}\ 0\ 0)$  planes and associated directions are shown as projections on the  $(000\ 1)$  basal plane.

the body diagonal. There are four atoms per unit cell and every atom of one type (group II) is tetrahedrally coordinated with four atoms of other type (group VI), and vice versa.

Because of the tetrahedral coordination of wurtzite and zinc blende structures, the 4 nearest neighbors and 12 next-nearest neighbors have the same bond distance in both structures. Stick-and-ball stacking models for 2H wurtzitic and 3C zinc blende polytypes of ZnO crystals are shown in Figure 1.6. The wurtzite and zinc blende structures differ only in the bond angle of the second-nearest neighbors and, therefore, in the stacking sequence of close-packed diatomic planes. The wurtzite structure consists of triangularly arranged alternating biatomic close-packed  $(000\ 1)$  planes, for example, Zn and O pairs; thus, the stacking sequence of the  $(000\ 1)$  plane is AaBbAaBb... in the  $\langle 000\ 1 \rangle$  direction, meaning a mirror image but no in-plane rotation with the bond angles. In contrast, the zinc blende structure along the  $[1\ 1\ 1]$  direction exhibits a  $60^\circ$  rotation and, therefore, consists of triangularly arranged atoms in the close-packed  $(1\ 1\ 1)$  planes along the  $\langle 1\ 1\ 1 \rangle$  direction that causes a stacking order of AaBbCcAaBbCc... The point with regard to rotation is very well illustrated in Figure 1.6b. Upper and lower case letters in the stacking sequences stand for the two different kinds of constituents.

Like other II–VI semiconductors, wurtzite ZnO can be transformed to the *rocksalt* (NaCl) structure at relatively modest external hydrostatic pressures. The reason for this is that the reduction of the lattice dimensions causes the interionic Coulomb interaction to favor the ionicity more over the covalent nature. The space group symmetry of the rocksalt type of structure is  $Fm\bar{3}m$  in the Hermann–Mauguin notation and  $O_h^5$  in the Schoenflies notation, and the structure is sixfold coordinated. However, the rocksalt structure cannot be stabilized by the epitaxial growth. In ZnO, the pressure-induced phase transition from the wurtzite (B4) to the rocksalt (B1)

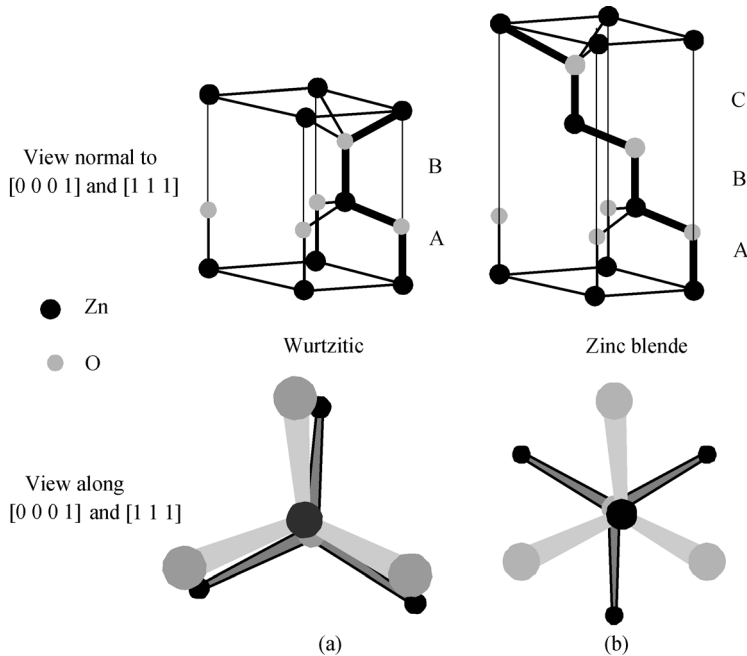


**Figure 1.6** Stick-and-ball stacking model of crystals with (a, both top and bottom) 2H wurtzitic and (b, both top and bottom) 3C zinc blende polytypes. The bonds in an A-plane ( $1\ 1\ \bar{2}\ 0$ ) are indicated with heavier lines to accentuate the stacking sequence. The figures on top depict the three-dimensional view. The figures at the bottom indicate the projections on the  $(0001)$  and  $(111)$  planes for wurtzitic and cubic phases, respectively. Note the rotation in the case of zinc blende along the  $\langle 111 \rangle$  direction.

phase occurs in the range of 10 GPa associated with a large decrease in volume of about 17% [8]. High-pressure cubic phase has been found to be metastable for long periods of time even at ambient pressure and above 100 °C [8]. Energy-dispersive X-ray diffraction (EDXD) measurements using synchrotron radiation have shown that the hexagonal wurtzite structure of ZnO undergoes a structural phase transformation with a transition pressure  $p_T = 10$  GPa and completed at about 15 GPa [9, 10]. The measured lattice-plane spacings as a function of pressure for the B1 phase are shown in Figure 1.7. Accordingly, a large fraction of the B1 phase is retained when the pressure is released indicating the metastable state of the rocksalt phase of ZnO even at zero pressure.

In contrast, using *in situ* X-ray diffraction [11], and later EDXD [12], this transition was reported to be reversible at room temperature. EDXD spectra recorded at pressures ranging from 0.1 MPa to  $56 \pm 1$  GPa at room temperature with increasing and decreasing pressures show a clear wurtzite-to-rocksalt transition starting at  $9.1 \pm 0.2$  GPa with increasing pressure. The two phases coexist over a pressure range of 9.1–9.6 GPa, as shown in Figure 1.8. The structural transition is complete at 9.6 GPa resulting in a 16.7% change in the unit cell volume. Upon decompression, it was observed that ZnO reverts to the wurtzite structure beginning at  $1.9 \pm 0.2$  GPa,

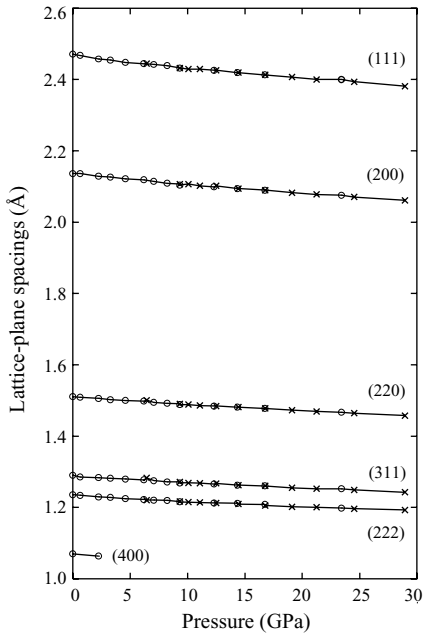


**Figure 1.7** Lattice-plane spacing as functions of pressure for the ZnO B1 phase. Crosses denote increasing pressure and circles decreasing pressure. Miller indices  $hkl$  are indicated for each set of data. (Courtesy of J.M. Recio [10].)

below which only a single wurtzite phase is present. Consequently, the phase hysteresis is substantial. Similar hysteresis was also reported for this transition using X-ray diffraction and Zn Mössbauer spectroscopy [13]. The transition pressure was measured to be 8.7 GPa for increasing pressure whereas it was 2.0 GPa for decreasing pressure.

On the theoretical side, there have been several first-principles studies of compressive parameters of dense ZnO, such as the linear combination of Gaussian-type orbitals (LCGTO), the Hartree–Fock (HF) method [20], the full-potential linear muffin-tin orbital (FP-LMTO) approach to density functional theory (DFT) within the local density approximation (LDA) and generalized gradient approximation (GGA) [14], linear augmented plane wave (LAPW) LDA [13], HF [15], correlated HF perturbed ion (HF-PI) models [10], LCGTO-LDA and GGA methods [10], and the extended ionic model [16]. A critical comparison between experimental and theoretical results can be made for ZnO as the structural and compressive parameters are measured because the dense solid adopts simple structures. These calculations have mostly been limited to the same pressure range as the experiments, and reasonable agreements are realized. Both experimental and theoretical results are summarized in Table 1.1 for comparison.

In addition to the commonly observed and calculated phase transition of ZnO from B4 to B1 at moderate pressures (maximum pressure attained in any experiment on

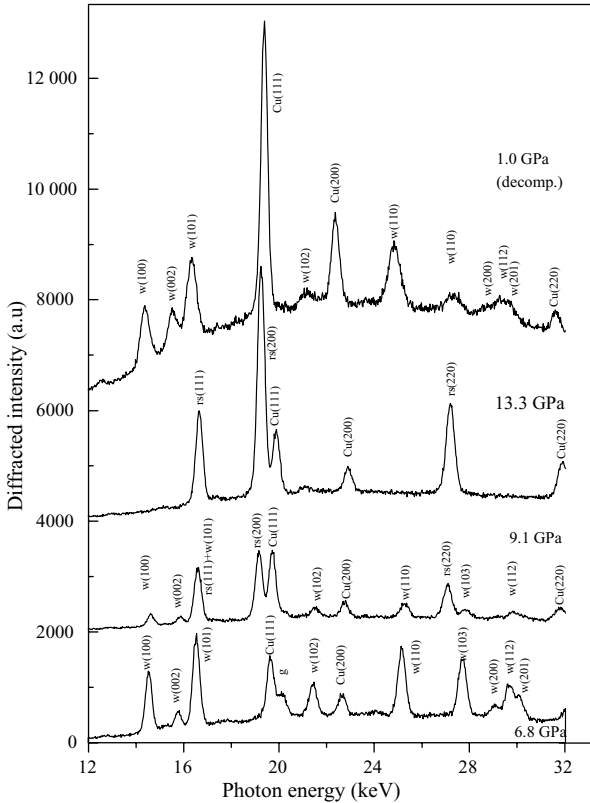


**Figure 1.8** Examples of EDXRD spectra indicating the coexistence of the wurtzite and rocksalt phases around  $9.1 \pm 0.2$  GPa (increasing pressure) and the emergence of the wurtzite phase  $P < 1.9 \pm 0.2$  GPa upon decompression. Spectra are presented in cascade for clarity.

Labels w and rs refer to wurtzite and rocksalt, respectively. X-ray diffraction lines from the Cu pressure gauge and the gasket material are labeled as Cu and g, respectively. (Courtesy of S. Desgreniers [12].)

ZnO to date is 56 GPa where the B1 phase remained stable), it has been suggested [17] that at sufficiently high pressures ZnO would undergo a phase transformation from the sixfold-coordinated B1 (cubic NaCl) to the eightfold-coordinated B2 (cubic CsCl) structure, in analogy to the alkali halides and alkaline earth oxides. The transition pressure from B1 phase to B2 phase was predicted at  $p_{T2} = 260$  and 256 GPa by employing local density approximation and generalized gradient – corrected local density – approximation, respectively [18], whereas atomistic calculations based on an interatomic pair potential within the shell model approach resulted in a higher value of  $p_{T2} = 352$  GPa [19]. However, these theoretical predictions are still awaiting experimental confirmation.

The ground-state total energy of ZnO in wurtzite, zinc blende, and rocksalt structures has been calculated as a function of the unit cell volume using first-principles periodic Hartree–Fock linear combination of atomic orbitals (LCAO)

Table 1.1 Theoretical and experimental compressive parameters of ZnO.

	Experimental results					Theoretical calculations				
	Ref. [8]	Ref. [9]	Ref. [11]	Ref. [12]	Ref. [13]	Ref. [13]	Ref. [14]	Ref. [17]	Ref. [19]	Ref. [20]
Volume, wurtzite ( $\text{\AA}^3$ )	23.829	23.785		23.81	23.796		23.62	23.346	23.839	24.570
Volume, rocksalt ( $\text{\AA}^3$ )	19.60	19.60	19.40	19.60	19.484		19.08	19.515	19.041	19.799
Volume change, $\Delta V/V$ (%)	16.7	18.0		17.68	18.13	17.9	18.8	16.41	20.3	19.42
Transition pressure, $p_T$ (GPa)	9.5	10.0	9.0	9.1	8.7	14.5	8.0	9.32	10.45	8.57

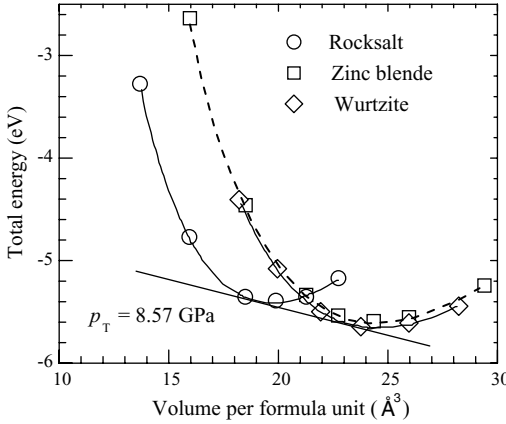


**Figure 1.9** Total energy versus volume (both per ZnO formula unit) for the three phases: zinc blende (squares), wurtzite (diamonds), and rocksalt (circles). The zero of energy is the sum of the total energies of an isolated Zn and an isolated O atom. The hexagonal/cubic phase transition occurs at  $p_T = 8.57$  GPa. (After Ref. [20].)

theory [20]. The total energy data versus volume for the three phases are shown in Figure 1.9 along with the fits to the empirical functional form of the third-order Murnaghan equation, which is used to calculate the derived structural properties:

$$E(V) = E_0 - \frac{B_0 V_0}{B' - 1} + \frac{B_0 V}{B'} \left[ \frac{(V_0/V)^{B'}}{B' - 1} + 1 \right], \quad (1.5)$$

where  $E_0$ ,  $V_0$ , and  $B_0$  are the total energy, volume per ZnO formula unit, and bulk modulus at zero pressure ( $P$ ), respectively, and  $B' = dB/dP$  is assumed to be constant.

In this calculation, although  $E_0$  represents the sum of the total energies of isolated neutral Zn and O atoms, the absolute value of the energy at the minimum of each curve was considered as a rough estimate of the equilibrium cohesive energy of the corresponding ZnO phases. The total energy (or roughly the cohesive energy per bond) in wurtzite variety was calculated to be  $-5.658$  eV for wurtzite,  $-5.606$  eV for zinc blende, and  $-5.416$  eV for rocksalt phases. The density functional theory using two different approximations, namely, the local density and the generalized gradient approximations, in the exchange correlation function was also employed to calculate the total energy and electronic structure of ZnO [18]. In these calculations, cohesive energies were obtained by subtracting the total energy per ZnO formula unit of the solid at its equilibrium lattice constant from the energy of the corresponding isolated atoms. The cohesive energies of ZnO obtained by using the LDA are  $-9.769$ ,  $-9.754$ , and  $-9.611$  eV for wurtzite, zinc blende, and rocksalt structures, respectively. The best agreement with the experimental value of  $-7.52$  eV, which is deduced from experimental Zn heat vaporization, ZnO enthalpy of formation, and  $O_2$  binding energy for the wurtzite phase [21], was achieved using the GGA technique. The GGA

gives  $-7.692$ ,  $-7.679$ , and  $-7.455$  eV cohesive energies for wurtzite, zinc blende, and rocksalt phases, respectively. In these two techniques, although the calculated energy difference  $\Delta E_{\text{W-ZB}}$  between wurtzite and zinc blende lattice is small (about  $-15$  and  $-13$  meV atom $^{-1}$  for LDA and GGA, respectively), whereas it is relatively large,  $\sim 50$  meV atom $^{-1}$ , for Hartree-Fock approximation, the wurtzite form is energetically favorable compared to zinc blende and rocksalt forms.

Because none of the three structures described above possesses inversion symmetry, the crystal exhibits crystallographic polarity, which indicates the direction of the bonds; that is, close-packed (1 1 1) planes in zinc blende and rocksalt (Rochelle salt) structures and corresponding (0 0 1) basal planes in the wurtzite structure differ from (1  $\bar{1}$   $\bar{1}$ ) and (0 0  $\bar{1}$ ) planes, respectively. The convention is that the [0 0 1] axis points from the face of the O plane to the Zn plane and is the positive  $z$ -direction. In other words, when the bonds along the  $c$ -direction are from cation (Zn) to anion (O), the polarity is referred to as Zn polarity. By the same argument, when the bonds along the  $c$ -direction are from anion (O) to cation (Zn), the polarity is referred to as O polarity. Many properties of the material depend also on its polarity, for example, growth, etching, defect generation and plasticity, spontaneous polarization, and piezoelectricity. In wurtzite ZnO, besides the primary polar plane (0 0 1) and associated direction  $\langle 0 0 1 \rangle$ , which is the most commonly used surface and direction for growth, many other secondary planes and directions exist in the crystal structure.

## 1.2

### Lattice Parameters

Lattice parameters of ZnO have been investigated over many decades [22–30]. The lattice parameters of a semiconductor usually depend on the following factors: (i) free electron concentration acting via deformation potential of a conduction band minimum occupied by these electrons, (ii) concentration of foreign atoms and defects and their difference of ionic radii with respect to the substituted matrix ion, (iii) external strains (e.g., those induced by substrate), and (iv) temperature. The lattice parameters of any crystalline material are commonly and most accurately measured by high-resolution X-ray diffraction (HRXRD) using the Bond method [31] for a set of symmetrical and asymmetrical reflections. Table 1.2 tabulates measured and calculated lattice parameters,  $c/a$  ratio, and  $u$  parameter reported by several groups for ZnO crystallized in wurtzite, zinc blende, and rocksalt structures for comparison.

The room-temperature lattice constants determined by various experimental measurements and theoretical calculations for the wurtzite ZnO are in good agreement with each other. The lattice constants mostly range from 3.2475 to 3.2501 Å for the  $a$ -parameter and from 5.2042 to 5.2075 Å for the  $c$ -parameter. The data produced in earlier investigations, reviewed by Reeber [30], are also consistent with the values given in Table 1.2. The  $c/a$  ratio and  $u$  parameter vary in a slightly wider range, from 1.593 to 1.6035 and 0.383 to 0.3856, respectively. The deviation from that of the ideal wurtzite crystal is probably due to lattice stability and ionicity. It has been reported that free charge is the dominant factor responsible for expanding

**Table 1.2** Measured and calculated lattice constants and the  $u$  parameter of ZnO.

Wurtzite				
$a$ (Å)	$c$ (Å)	$c/a$	$u$	Reference
		1.633	0.375	Ideal
3.2496	5.2042	1.6018	0.3819	<sup>a</sup>
3.2501	5.2071	1.6021	0.3817	<sup>b</sup>
3.286	5.241	1.595	0.383	<sup>c</sup>
3.2498	5.2066	1.6021		<sup>d</sup>
3.2475	5.2075	1.6035		<sup>e</sup>
3.2497	5.206	1.602		<sup>f</sup>
		1.593	0.3856	<sup>g</sup>
		1.600	0.383	<sup>h</sup>
Zinc blende (sphalerite actually)				
4.619 <sup>c</sup> , 4.60 <sup>g</sup> , 4.463 <sup>i</sup> , 4.37 <sup>i</sup> , 4.47 <sup>i</sup>				
Rocksalt (Rochelle salt)				
4.271 <sup>a</sup> , 4.283 <sup>d</sup> , 4.294 <sup>e</sup> , 4.30 <sup>g</sup> , 4.280 <sup>j</sup> , 4.275 <sup>k</sup> , 4.058 <sup>k</sup> , 4.316 <sup>k</sup> , 4.207 <sup>k</sup> , 4.225 <sup>l</sup>				

<sup>a</sup>Measured by using XRD [13].<sup>b</sup>Measured by using XRD [4].<sup>c</sup>Calculated by using *ab initio* periodic LCAO method, based mainly on the Hartree–Fock Hamiltonian, with an all-electron Gaussian-type basis set [32].<sup>d</sup>Measured by using EDXD [12].<sup>e</sup>Measured by using XRD [9].<sup>f</sup>Measured by using XRD [30].<sup>g</sup>Calculated by using first-principles periodic Hartree–Fock LCAO program [20].<sup>h</sup>Calculated by using *ab initio* quantum mechanical level through the Berry phase scheme applied to delocalized crystalline orbitals and through the definition of well-localized Wannier functions [33].<sup>i</sup>Measured by using RHEED, XRD, and TEM [6].<sup>j</sup>Measured by using XRD [8].<sup>k</sup>Measured by using EDXD and calculated by using Coulomb Hartree–Fock perturbed ion, GGA, and LDA methods [10].<sup>l</sup>Calculated by using first-principles periodic Hartree–Fock [15].

the lattice proportional to the deformation potential of the conduction band minimum and inversely proportional to the carrier density and bulk modulus. The point defects such as zinc antisites, oxygen vacancies, and extended defects, such as threading dislocations, also increase the lattice constant, albeit to a lesser extent in the heteroepitaxial layers.

For the zinc blende polytype of ZnO, the calculated lattice constants based on modern *ab initio* technique are predicted to be 4.60 and 4.619 Å. Zinc blende ZnO films have been grown by using ZnS buffer layers [6]. The lattice constant was estimated to be 4.463, 4.37, and 4.47 Å by using the spacing of RHEED pattern, albeit spotty, comparing the XRD peak position, and examining the transmission electron microscopy (TEM) images, respectively. These values are far from wurtzite phase indicating the formation of zinc blende ZnO. The lattice constant measured with the RHEED technique is in very good agreement with the theoretical predictions.

High-pressure phase transition from the wurtzite to the rocksalt structure decreases the lattice constant down to the range of 4.271–4.294 Å. The experimental values obtained by X-ray diffraction are in close agreement. The predicted lattice parameters of 4.058–4.316 Å, using various calculation techniques such as the HF-PI, GGA, and HF, are about 5% smaller or larger than the experimental values. The dispersion in the calculated values is larger than the measured ones.

The ideal relationship between the  $c/a$  axial ratio and the  $u$  oxygen positional parameter is preserved as the wurtzite ZnO lattice becomes denser while approaching the structural transition pressure [12]. The change in the  $c/a$  axial ratio was measured up to  $\sim 10$  GPa, and a pressure coefficient of  $d(c/a)/dP = -0.0005$   $0.0001 \text{ GPa}^{-1}$  was obtained from a linear fit (giving  $c/a = 1.6021$  at atmospheric pressure) to the experimental data. Even though the variation with pressure seems within the experimental error, this pressure coefficient is in agreement with the previously published experimental ( $-0.0007 \text{ GPa}^{-1}$ ) [13] and predicted ( $-0.0005 \text{ GPa}^{-1}$ ) [20] values. The effect of pressure-induced change in the axial ratio on the  $u$  parameter against a possible breakdown of the ideal relationship between the axial ratio and  $u$  was isolated by recording pressure dependence variation of X-ray diffraction intensity.

### 1.3

#### Electronic Band Structure

The band structure of a given semiconductor is pivotal in determining its potential utility. Consequently, an accurate knowledge of the band structure is critical if the semiconductor in question is to be incorporated in the family of materials considered for device applications. Several theoretical approaches with varying degrees of complexity have been employed to calculate the band structure of ZnO for its wurtzite, zinc blende, and rocksalt polytypes. Besides, a number of experimental data have been published regarding the band structure of the electronic states of wurtzite ZnO. X-ray or UV reflection/absorption or emission techniques have conventionally been used to measure the electronic core levels in solids. These methods basically measure the energy difference by inducing transitions between electronic levels (e.g., transitions from the upper valence band states to the upper conduction band states and from the lower valence band states) or by exciting collective modes (e.g., the upper core states to the lower edge of the conduction band and to excitations of plasmons). Another important method for the investigation of the energy region is based on the photoelectric effect extended to the X-ray region, namely, photoelectron spectroscopy (PES). The peaks in emission spectrum correspond to electron emission from a core level without inelastic scattering, which is usually accompanied by a far less intense tail region in the spectrum. Additionally, angle-resolved photoelectron spectroscopy (ARPES) technique together with synchrotron radiation excitation have been recognized as a powerful tool that enables the determination of experimental bulk and surface electronic band structures under the assumptions of  $k$ -conservation and single

nearly free-electron-like final band [34]. After the first theoretical work on band structure calculation of ZnO proposed by Rössler using Green's function (Korringa–Kohn–Rostoker (KKR) method) [35] in 1969, several experimental works [36–39] have been performed on the wurtzite ZnO, which proved Rössler's predicted bulk electronic structure to be far from satisfactory. The first experimental data related to the energy levels of core electrons in ZnO were obtained by using X-ray induced photoemission spectroscopy [36]. Consequently, the location of the Zn 3d level in ZnO was unambiguously determined and the discrepancy between the measured values and the theoretically determined energy values was found to be dependent on angular momentum. UV photoemission measurements on hexagonal ZnO cleaved in vacuum showed the Zn 3d core level at about 7.5 eV below the valence band maximum [37, 38], which is 3 eV lower than the value predicted by Rössler's band calculation. This assignment is in good agreement with X-ray photoemission measurements that produced 8.5 eV [40] and 8.81 eV [39]. In the ensuing years, local density approximation and tight-binding methods were carried out [41–44] by considering the Zn 3d states as core levels to simplify calculations. Satisfactory agreement with qualitative valence band dispersions was achieved with this assumption. However, quantitative disagreements remained and the location of the Zn 3d states could not be predicted. With the advent of new computer capabilities, theoretical works began to include the effect of Zn 3d level in the calculations and thus considering them as valence band states [45–48]. These methods enable an estimation of the position of the Zn 3d states and also take into account their non-negligible influence on the s- and p-derived valence bands.

Angle-resolved photoelectron spectroscopy has been employed to study the electronic structure of the ZnO (0001) [49]. Recording both normal and off-normal emission spectra gives valuable information about bulk and surface states as well as the Zn 3d states. Figure 1.10 shows some of the normal emission spectra recorded at photon energies ranging from 20 to 50 eV and the information extracted from these data for bulk band structure. In these measurements, the binding energies were referred to the Fermi level and the intensities were normalized to the photon flux. Among all the spectra displayed, seven features were observed, labeled from A to G. The dispersions of the four valence bands observed in the (0001) direction were compared with theory based on LDA calculations, which consider the Zn 3d electrons as part of the valence band [45] and good agreement was realized. It should also be noted that the Zn 3d states were observed to separate into two groups of four and six bands, which show dispersion with  $k$ , which is in agreement with theoretical results, but the locations of these states (about 10.5 eV below Fermi level) were not accurately predicted.

The polar (0001)-Zn and (000 $\bar{1}$ )-O surfaces and the nonpolar (10 $\bar{1}$ 0) surface ( $m$ -plane) have also been the object of experimental and theoretical investigations. Of these surfaces, the nonpolar (10 $\bar{1}$ 0) surface is of particular interest from the viewpoint of surface chemistry, because the surface is terminated with the same number of O and Zn atoms. The low-energy electron diffraction (LEED) studies have revealed that the surface undergoes relaxation, which is characterized by downward shift (spatially) of both surface Zn and O atoms, with a greater shift for the Zn atom

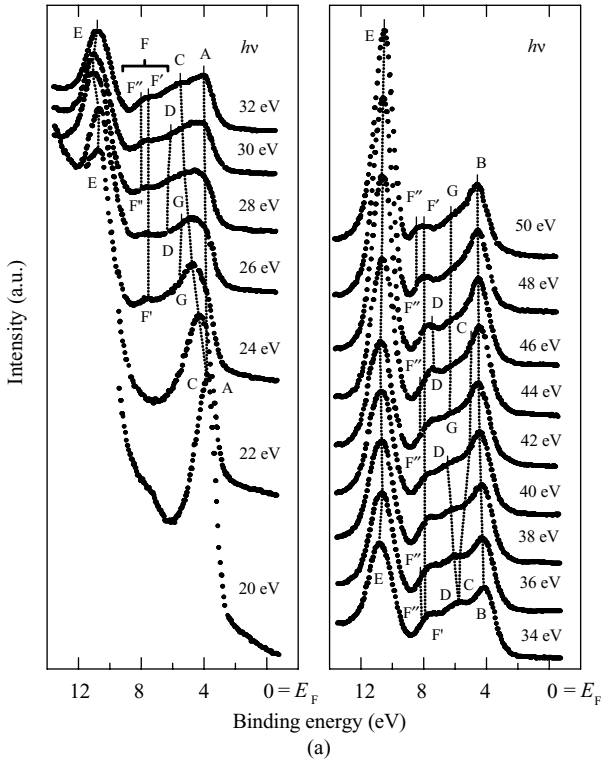


**Figure 1.10** (a) Normal emission spectra for photon energies ranging between 20 and 50 eV. The spectra were normalized with respect to the photon flux. (b) Bulk band structure of ZnO,  $\Gamma A$  corresponding to  $0.6 \text{ \AA}^{-1}$ . (After Ref. [49].) The dashed lines are the LDA calculation results reproduced from Schröer *et al.* [45].

than the O atom, resulting in the Zn–O bond rotation by  $6.2^\circ$  [50] or  $11.5^\circ$  [51] with respect to the ideal surface plane. Such a surface relaxation should influence the energetic position as well as the dispersion width of the surface dangling bond bands of the occupied O 2p and unoccupied Zn 4s states. Besides, several theoretical studies have indicated that, upon relaxation, the O 2p dangling bond state is stabilized while the Zn 4s dangling bond state shifts up in energy [43, 47, 52]. The theoretically determined position of these dangling bond bands, especially the occupied O 2p dangling bond band, relative to the bulk bands projected onto the (1 0 1 0) surface varies depending on the method employed in the calculations.

Surface states have been revealed in ARPES studies of both polar and nonpolar ZnO surfaces. In one particular study [53], two surface-induced features at the  $\Gamma$ ,  $M$ , and  $X$  points of the surface Brillouin zone (BZ) have been identified and assigned to the O 2p-derived dangling bond state and the Zn–O backbond state. Similarly, the

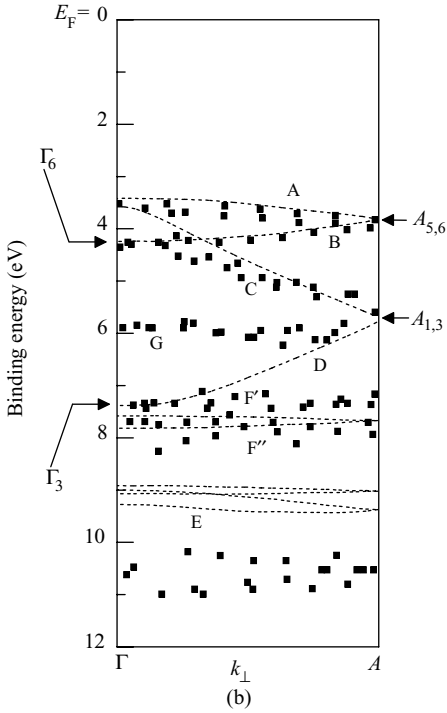
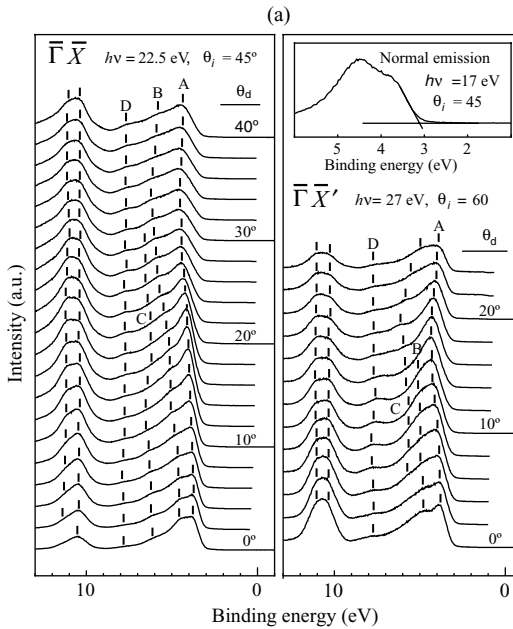


Figure 1.10 (Continued)

off-normal ARPES spectra recorded in the  $\bar{\Gamma}\bar{M}$ ,  $\bar{\Gamma}\bar{K}$ , and  $\bar{K}\bar{M}$  directions, for 20, 34, and 44 eV photon energies and emission angles ranging between 0 and 30° revealed two surface states on the (0001) surface [49]. One of these states, with a 7.5 eV binding energy as predicted by theory, was interpreted as arising from the “backbondings” of the Zn 4s–O 2p mixed bulk states. The other state at 4.5 eV below the Fermi level, which was not predicted by theoretical calculations, was related to Zn 4p–O 2p-derived states. However, in another ARPES study on ZnO (10 $\bar{1}$ 0) surface [54], where the valence band structure along the  $\Gamma M$  axis of the bulk BZ was revealed, no surface-related states were identified and all the observed peaks were attributed to the bulk band transitions.

Detailed ARPES study has been performed to investigate the two-dimensional band structure of the O 2p dangling bond state on the ZnO (10 $\bar{1}$ 0) surface along the selected high-symmetry axes of the surface BZ, that is, the  $\bar{\Gamma}\bar{X}$  and  $\bar{\Gamma}\bar{X}'$  axes [55]. The energetic position relative to the projected bulk bands and the dispersion of the dangling bond band were determined and compared well with the calculated band structures [47, 52]. Figure 1.11 shows off-normal emission spectra taken at various detection angles along the [1 $\bar{2}$ 10] ( $\bar{\Gamma}\bar{X}$ ) and [0001] ( $\bar{\Gamma}\bar{X}'$ ) azimuths and measured dispersion of the O 2p dangling bond state and the bulk band related states along the  $\bar{\Gamma}\bar{X}$  and  $\bar{\Gamma}\bar{X}'$  axes together with theoretical calculations for comparison.



**Figure 1.11** (a) Off-normal emission spectra of the clean surface recorded at  $h\nu = 22.5$  eV and  $\theta_i = 45^\circ$  along the  $[1\ 2\ 1\ 0]$  ( $\bar{\Gamma}\bar{X}$ ) direction and at  $h\nu = 27$  eV and  $\theta_i = 60^\circ$  along the  $[000\ 1]$  ( $\bar{\Gamma}\bar{X}'$ ) direction. The incidence plane of the light was parallel to the  $[1\ 2\ 1\ 0]$  direction for both detection directions. The spectra are shown with a  $2^\circ$  interval. Peak positions, indicated by vertical bars, were determined from the second derivative of the spectra. The position of the valence band maximum was determined from the normal emission spectrum taken at  $h\nu = 17$  eV by extrapolating the onset of the

valence band emission as shown in the inset of the right panel. (Courtesy of K. Ozawa [55].) (b) Measured dispersion of the O 2p dangling bond state (open circles) and the bulk band related states (filled circles) along the  $\bar{\Gamma}\bar{X}$  and  $\bar{\Gamma}\bar{X}'$  axes. (Courtesy of K. Ozawa [55].) Hatched area corresponds to the projected bulk band region and a bold dashed line indicates the O 2p dangling bond bands, both of which have been calculated by using the  $sp^3$  model by Wang and Duke [52]. Thin dashed lines located above the projected bulk bands are the dangling bond bands obtained from the LDA calculations [47].

From photon energy dependent measurements and K and O<sub>2</sub> adsorption studies, it has been found that the surface-localized O 2p dangling bond state exists at 3.7 eV below the Fermi level at the  $\bar{\Gamma}$  point in the surface Brillouin zone and shifts to the higher binding energy side by 0.8 and 0.5 eV along the  $\bar{\Gamma}\bar{X}$  and  $\bar{\Gamma}\bar{X}'$  axes, respectively. Measurements on K and O<sub>2</sub> exposed ZnO (1 0 1 0) surfaces helped to identify which peaks in the angle-resolved photoelectron spectra were associated with the states localized at the surface. The O 2p dangling bond band was found located below the upper edge of the projected bulk bands along these two high-symmetry axes. The empirical tight-binding calculations, which emphasize the ionic [43] and covalent [52] characters of the Zn–O bonds, predict that the gap state by the O 2p dangling bond is not formed at least along the  $\bar{\Gamma}\bar{X}$  and  $\bar{\Gamma}\bar{X}'$  axes. On the contrary, calculations using LDA [47] indicate that the dangling bond band is formed within the gap above the

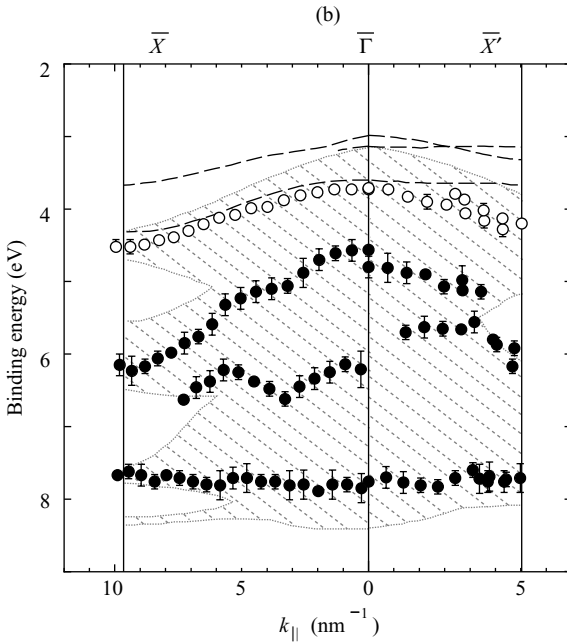


**Figure 1.11** (Continued)

upper edge of the projected bulk bands along the major high-symmetry axes of the surface BZ. Therefore, it has been concluded that the experimental study is consistent qualitatively with the band structure given by two empirical tight-binding approaches.

The theoretical calculation of the band structure of ZnO mostly involves the local density approximation [45, 56–58], which is very demanding because of the cationic d electrons. If the d electrons are treated as core electrons, the calculated lattice constant underestimates the experimental values by as much as 18% for wurtzite ZnO, while inclusion of the d electrons in the valence band yields very accurate lattice constants. However, even if the d electrons are properly taken into account, the results of standard LDA calculations show distinct shortcomings, such as strongly underestimated bandgap and overestimated occupied cationic d bands, which are roughly 3 eV high in energy compared to those of the experiment. In addition, their interactions with the anion p valence bands are artificially enlarged, resulting in overestimated dispersion and bandwidth of the latter and shifting them unphysically close to the conduction bands. For example, the LDA underestimates the ZnO bandgap to be as low as  $E_g^{\text{LDA}} = 0.23$  eV as opposed to  $E_g^{\text{Exp}} = 3.37$  eV. However, by carrying out the plane-wave GW calculations deliberately with the experimental lattice constants and simply treating the d electrons as core electrons very close results have been obtained for the anion p valence bands and for the bandgap energies even though no assertion concerning the d band positions could be made [59]. As an

alternative approach for treating the II–VI semiconductors, approximate incorporation of the dominant self-interaction corrections has been suggested [48]. It has been shown that self-interaction corrections to LDA can be very important for a quantitative description of a system with strongly localized states such as 3d electrons. The results along with the LDA calculations without the corrections and the O 2p valence bands in more detail with ARPES data are shown in Figure 1.12 for comparison. The left panel in Figure 1.12a shows the standard LDA result, which reveals the above-mentioned shortcomings. The right panel shows the band structure as calculated with self-interaction corrected pseudopotential (SIC-PP) approach included in the LDA. It has been observed that the d bands are shifted down in energy considerably and concomitantly the bandgap is opened drastically. The dispersion and bandwidth of the O 2p are also changed. Compared to experimental data, the standard LDA result is obscured by the artificially high-lying bands leading to strong p–d interactions with the O 2p bands. The SIC-PP results are in better agreement with experiments. The calculated and measured energy gaps, the position of the cation d band, and anion valence bandwidths of ZnO are given in Table 1.3. Based on this table, the LDA-SIC-PP approximation gives close agreement with the

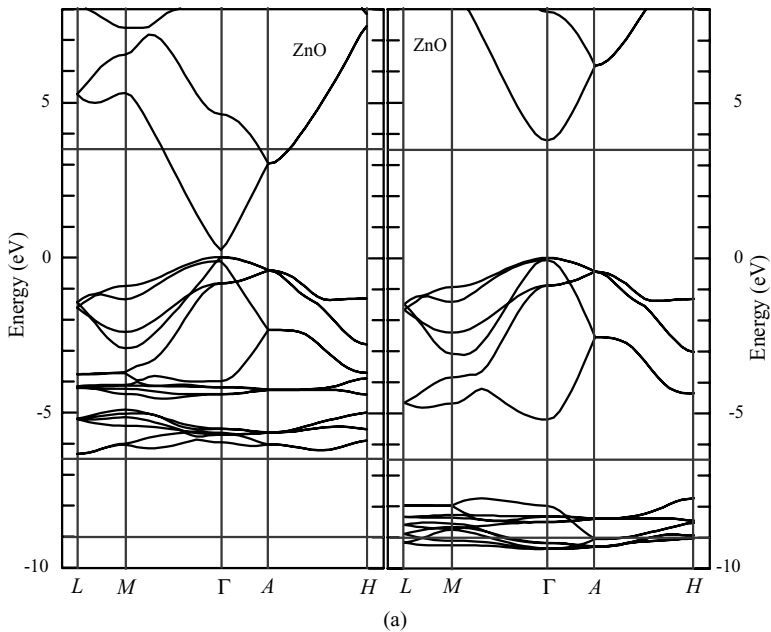


**Figure 1.12** (a) LDA bulk band structure of ZnO as calculated by using a standard pseudopotential (PP) (left panel) and by using SIC-PP (right panel). The horizontal dashed lines indicate the measured gap energy and d-band width. (b) Comparison of calculated and measured valence bands of ZnO. The left panel shows the standard LDA, while the right panel shows SIC-PP results. (Courtesy of J. Pollmann [48].)

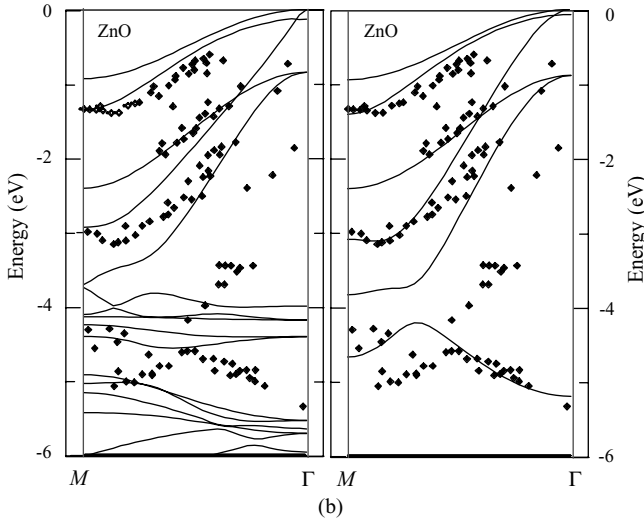


**Figure 1.12** (Continued)

experimental results for bandgap and bandwidth compared to the standard LDA method. However, the d bands result in energy roughly 1 eV too low compared to the experimental value. This deviation was attributed to the measured exciton energies influenced by electronic relaxations, which is expected to be mostly pronounced for the highly localized cationic semicore d states.

The band structure of ZnO reveals three very closely spaced valence bands (usually referred to as the A, B, and C bands, or the heavy-hole, light-hole, and crystal field split-off bands, respectively, resulting from the spin-orbit coupling and crystal field splitting) near the zone center ( $\Gamma$  point), the details of which will be discussed in Chapter 3. Figure 1.13 shows the valence band structure of ZnO near the  $\Gamma$  point calculated using the atomic sphere approximation (ASA) and linearized muffin-tin orbital (LMTO) methods within the LDA [60]. The splitting energies between the A, B, and C bands have been calculated to be small, with  $E_{AB} = 10$  meV and  $E_{BC} = 34$

**Table 1.3** Calculated and measured energy gaps  $E_g$ , cation d-band positions  $E_d$ , and anion p valence bandwidths  $W_p$  (all in eV) of ZnO.

	LDA-PP	LDA-SIC-PP	Experiment
$E_g$	0.23	3.77	3.4
$E_d$	-5.1	-8.9	-7.8
$W_p$	-3.99	-5.2	-5.3

After Ref. [48]. LDA-PP: local density approximation – pseudopotential. LDA-SIC-PP: local density approximation – self-interaction corrected pseudopotential.

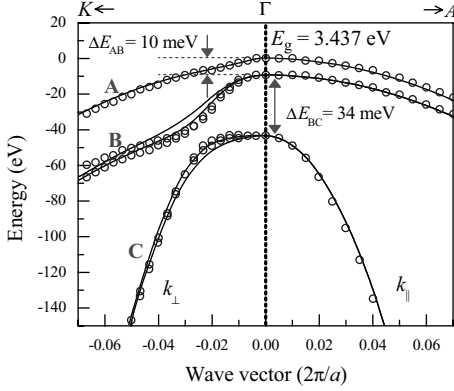


**Figure 1.13** Valence band structure of ZnO near the  $\Gamma$  point. The open circles represent the calculation results using the ASA-LMTO method including spin-orbit coupling. The solid lines are fits to the Rashba-Sheka-Pikus effective Hamiltonian. (After Ref. [60].)

meV [60], where the experimental bandgap is 3.437 eV [61]. The calculated splitting energies are in good agreement with the experimental values of  $E_{AB} = 9.5$  meV and  $E_{BC} = 39.7$  meV [61]. The valence band splitting energies measured for several bulk crystals are given in Table 3.1.

The lattice constants change with temperature, as will be discussed in Section 1.6.1, and with pressure as already mentioned in Section 1.2. Consequently, the electronic band structure changes with temperature and pressure. The bandgap (at  $\Gamma$  point) shrinks with increasing temperature and the dependence is given by the empirical relationship [62]

$$E_g(T) = E_g(T = 0) - \frac{\alpha T^2}{T + \beta}, \quad (1.6)$$

where the temperature coefficients are  $\alpha = -5.5 \times 10^{-4}$  eV K $^{-1}$  and  $\beta = -900$  K for temperatures up to 300 K [63]. The excitonic transition energies associated with the A, B, and C valence bands have also been shown to follow the same dependence with  $\alpha = -7.2 \times 10^{-4}$  eV K $^{-1}$  and  $\beta = -1077$  K [64]. Temperature dependence of the excitonic transitions in ZnO is further discussed in Section 3.2.5. With increasing hydrostatic pressure, the bandgap of wurtzite ZnO shows a sublinear increase [65]. The pressure dependence is well explained by a second-order polynomial, and the pressure coefficients measured at 6 K for the three bandgaps involving A, B, and C valence bands are given in Table 1.4.

To understand the transport phenomena and, for example, calculate the optical gain in semiconductors, the effective mass, which is one of the fundamental quantities in semiconductor physics, should be known for each of the electronic bands participating in the processes under investigation. The effective mass can be obtained from the electronic band structure calculations using the first-principles methods already

**Table 1.4** Pressure coefficients for energy gaps associated with the A, B, and C valence bands in single-crystal ZnO measured at 6 K.

	$E_g (P=0)$	$dE/dP$ (meV GPa <sup>-1</sup> )	$d^2E/dP^2$ (meV GPa <sup>-2</sup> )
A	$3.4410 \pm 0.0001$	$24.7 \pm 0.1$	$-0.28 \pm 0.01$
B	$4.4434 \pm 0.0001$	$25.3 \pm 0.1$	$-0.28 \pm 0.01$
C	$3.4817 \pm 0.0002$	$25.6 \pm 0.2$	$-0.28 \pm 0.01$

After Ref. [65].

mentioned above. The density functional theory within LDA, which is commonly used for this purpose, underestimates the effective masses in semiconductors as well as the bandgaps. The self-energy corrections using the GW approximation (GWA), however, have been shown to remove the LDA defects and result in quasiparticle effective masses in agreement with the experimental data [66]. Electron and hole effective masses derived from the calculated and measured energy band structures are listed in Table 1.5 [58, 60, 66–80].

The electronic band structure of the other phases of ZnO has also been calculated using various methods [18, 20, 82, 83]. For example, by utilizing both the LDA and the PBE96 forms of the GGA methods together with optimized Gaussian basis sets and by expanding the crystal orbitals and periodic electron density, the electronic structure for the B4 (wurtzite), B3 (zinc blende), B1 (rocksalt), and B2 (CsCl) phases has been calculated over a range of unit cell volumes [18]. Figures 1.14 and 1.15 show the calculated band structure and the total DOS (density of states) of ZnO for different phases. When wurtzite ZnO is compressed, it has been observed that the peak at the top of the upper valence band is slightly reduced in height and shifted down in energy, the O 2s- and Zn 3d-derived peaks are slightly broadened and shifted up in energy, and a splitting appears in the Zn 3d states. While transforming to the B1 structure at the transition pressure  $p_{T1}$ , significant changes have been observed; in particular, the peak near the valence band maximum is greatly reduced in height. The Zn 3d peak also becomes narrower, and the O 2s-derived states drop slightly in energy. Upon compression of the B1 phase ZnO through the wide pressure range from  $p_{T1}$  to  $p_{T2}$ , it has been observed that the upper valence band broadens greatly, the splitting of the Zn 3d peak in the DOS shows a large increase, and the O 2s-derived band moves down in energy and broadens. The fundamental bandgap also increases with increasing pressure in this range. With the B1 → B2 transition, the upper valence bandwidth remains almost unchanged but the peak near the valence band maximum reappears. The structure of the Zn 3d states changes radically with the O 2p-derived states because of heavy hybridization, and the O 2s-derived states broaden further and shift up in energy. From these observations of ZnO band structure with compression and changed atomic coordination, it has been argued that the key features are (a) changes in nearest-neighbor bond lengths as they affect overlaps and bandwidths and (b) changes in symmetry as they affect p–d hybridization and band repulsion. As the neighboring atoms approach each other with compression of the solid, basis

**Table 1.5** Calculated and measured conduction band (electron) and valence band (hole) effective masses for wurtzite ZnO and rocksalt MgO.

	ZnO (wurtzite)		MgO (rocksalt) Calculated
	Calculated	Experimental	
$m_{e\parallel}^*$	0.28 <sup>b</sup> , 0.21 <sup>d</sup> , 0.30 <sup>f</sup> , 0.181 <sup>g</sup> , 0.14 <sup>h</sup> , 0.14 <sup>i</sup> , 0.19 <sup>j</sup>	0.265 <sup>k</sup> , 0.24 <sup>n</sup> , 0.24 <sup>o</sup> , 0.3 <sup>p</sup> , 0.210 <sup>s</sup>	0.35 <sup>t</sup>
$m_{e\perp}^*$	0.24 <sup>c</sup> , 0.25 <sup>d</sup> , 0.177 <sup>g</sup> , 0.13 <sup>h</sup> , 0.14 <sup>i</sup> , 0.21 <sup>j</sup>	0.24(0.29) <sup>l</sup> , 0.28 <sup>n</sup> , 0.23(0.29) <sup>r</sup> , 0.242 <sup>s</sup>	
$m_{\text{hh}\parallel}^*$	0.67 <sup>a</sup> , 1.98 <sup>b</sup> , 2.74 <sup>e</sup> , 2.45 <sup>h</sup> , 2.27 <sup>i</sup> , 0.21 <sup>j</sup>	0.45 <sup>m</sup> , 0.59 <sup>o</sup>	1.60 [0 0 1] <sup>t</sup> , 2.77 [1 1 1] <sup>t</sup>
$m_{\text{hh}\perp}^*$	0.63 <sup>a</sup> , 0.54 <sup>e</sup> , 0.35 <sup>i</sup>	0.59 <sup>o</sup>	
$m_{\text{lh}\parallel}^*$	0.67 <sup>a</sup> , 3.03 <sup>e</sup> , 2.98 <sup>h</sup> , 3.23 <sup>i</sup> , 4.33 <sup>j</sup>	0.45 <sup>m</sup> , 0.59 <sup>o</sup>	0.35 [0 0 1] <sup>t</sup> , 0.31 [1 1 1] <sup>t</sup>
$m_{\text{lh}\perp}^*$	0.63 <sup>a</sup> , 0.55 <sup>e</sup> , 0.23 <sup>h</sup> , 0.30 <sup>i</sup>	0.59 <sup>o</sup>	
$m_{\text{ch}\parallel}^*$	0.25 <sup>a</sup> , 0.27 <sup>e</sup> , 0.17 <sup>h</sup> , 0.17 <sup>i</sup> , 0.33 <sup>j</sup>	0.31 <sup>o</sup>	
$m_{\text{ch}\perp}^*$	2 <sup>a</sup> , 1.12 <sup>e</sup> , 0.29 <sup>h</sup> , 0.54 <sup>i</sup> , 0.27 <sup>j</sup>	0.55 <sup>o</sup>	

$\perp$  and  $\parallel$  refer to the directions perpendicular and parallel, respectively, to the  $c$ -axis.

<sup>a</sup>Calculated by using the  $k$ - $p$  theory [67].

<sup>b</sup>Calculated by using the first-principles orthogonalized linear combination of atomic orbitals method in the local density approximation. The effective masses were found to be highly anisotropic and the values in the table are for  $\Gamma$ -A. Other values are 0.37 ( $\Gamma$ -K) and 0.32 ( $\Gamma$ -M) for the electron mass and 4.31 ( $\Gamma$ -K) and 4.94 ( $\Gamma$ -M) for the hole mass [58].

<sup>c</sup>Calculated from first principles: LMTO basis with the ASA and the self-energy correction within the Green function and the screened Coulomb potential approximation (GWA) [68].

<sup>d</sup>Calculated quasiparticle effective masses by using the density functional theory within the local density approximation including the correlation effects in the form of self-energy correction [66].

<sup>e</sup>Calculated by using the ASA and the LMTO density functional theory in the local density approximation [60].

<sup>f</sup>Calculated using the frozen-core projector augmented wave method based upon the DFT with the Perdew-Wang generalized gradient approximation for  $\Gamma$ -A. The electron effective masses were 0.31 and 0.32 for  $\Gamma$ -K and  $\Gamma$ -M, respectively [69].

<sup>g</sup>Calculated by using the  $k$ - $p$  and empirical pseudopotential methods [70].

<sup>h</sup>Calculated by using the density functional theory within the LDA.

<sup>i</sup>Generalized gradient approximation.

<sup>j</sup>LDA with the multiorbital mean-field Hubbard potential (LDA + U) [71].

<sup>k</sup>From infrared reflectivity measurements on indium-doped ZnO crystals grown from the vapor phase [72].

<sup>l</sup>From free carrier Faraday rotation for the high-frequency conduction band mass in hydrothermally grown undoped and indium-doped ZnO single crystals. The value in parentheses (0.29) is for the low-frequency polaron mass [73].

<sup>m</sup>From two-photon magnetoabsorption in ZnO single crystals [74].

<sup>n</sup>From cyclotron resonance on bulk ZnO grown by vapor-phase reaction method. The same study also reports electron effective masses of  $0.3m_0$  and  $0.34m_0$  obtained from Zeemann splitting measurements for  $m_{e\perp}^*$  and  $m_{e\parallel}^*$ , respectively [75].

<sup>o</sup>From Ref. [76].

<sup>p</sup>From far-infrared cyclotron resonance on hydrothermally grown  $n$ -ZnO (donors originate from O vacancies, excessive Zn and Li) [77].

<sup>r</sup>From infrared cyclotron resonance in  $n$ -type ZnO grown by seeded chemical vapor transport method (Eagle-Picher). The value in parentheses (0.29) is the effective polaron mass [78].

<sup>s</sup>Derived by comparing the experimental (ellipsometry on samples grown by chemical vapor transport and hydrothermal (Airtron Industries) methods) [81] and calculated imaginary parts of the dielectric function [79].

<sup>t</sup>From Ref. [80].

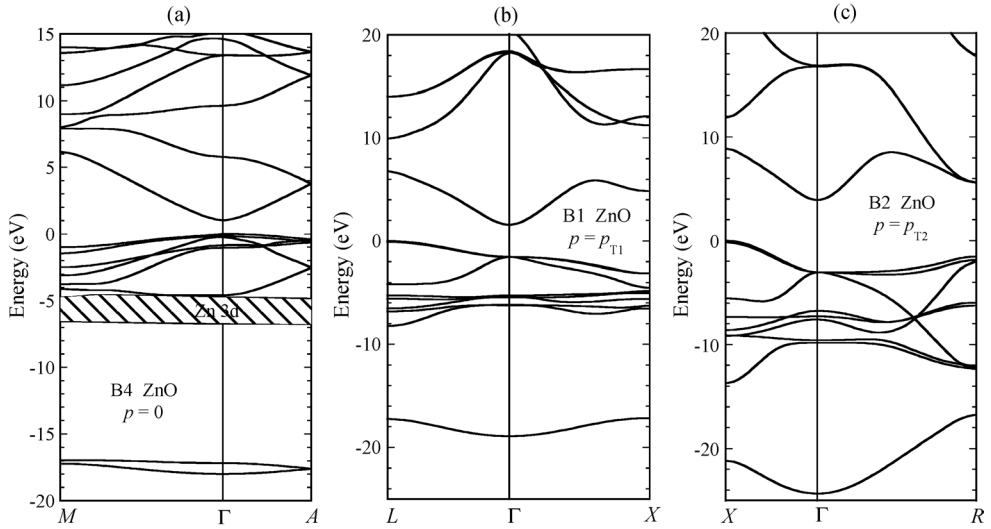


**Figure 1.14** Band structure for ZnO: (a) B4 structure at  $p = 0$ , (b) B1 structure at  $p = p_{T1}$ , (c) B2 structure at  $p = p_{T2}$ . (Courtesy of J.E. Jaffe [18].)

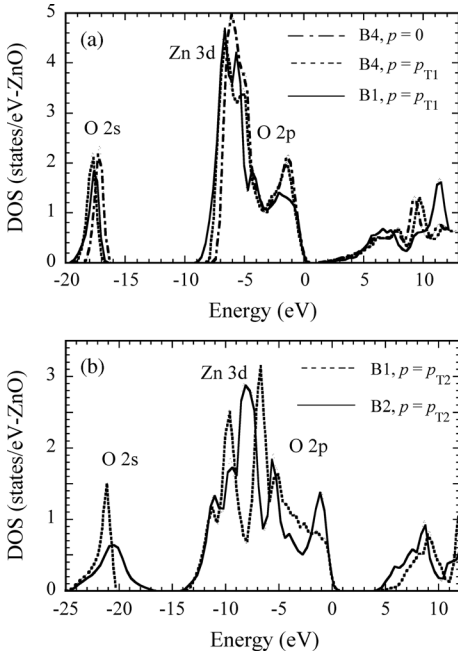


**Figure 1.15** Total density of states for ZnO in the (a) B4 structure at  $p = 0$  and  $p = p_{T1}$  and B1 structure at  $p = p_{T1}$ , and (b) B1 and B2 structures at  $p = p_{T2}$ . (Courtesy of J.E. Jaffe [18].)

functions (and orbitals in a Hückel-like picture [84]) overlap more strongly, producing increased dispersion of the electron bands in  $k$ -space and consequently increased bandwidths along the energy axis.

However, it has also been considered that when there is a phase transition to a structure of increased coordination, the nearest-neighbor bonds lengthen even though the density is increased. The behavior of the bandwidths up to  $p_{T_2}$  reflects these considerations. The band structures reveal further qualitative changes that occur with the change of symmetry at the structural transitions. Where the symmetry permits hybridization of O 2p- and Zn 3d-derived bands, there is an effective repulsion between them, which pushes the anion 2p states upward. In the tetrahedrally coordinated B4 phase, this repulsion is present throughout the Brillouin zone, but in the cubic B1 and B2 structures it is suppressed near the  $\Gamma$  point as a result of the inversion symmetry through the atomic center. Consequently, the high-energy valence bands are repelled upward near the zone boundaries but not at the zone center, so that the valence band maximum now occurs at the zone boundary. This accounts for the change in shape of the band edge seen in the total DOS plots. There is also a change in the form of the Zn 3d-derived bands, which are now narrowest near the gamma point as a result of the suppressed hybridization there. In the B2 structure, the Zn 3d and O 2p states are completely hybridized and cannot be disentangled.

#### 1.4

#### Mechanical Properties

The mechanical properties of materials involve various concepts such as hardness, stiffness, and piezoelectric constants, Young's and bulk modulus, and yield strength. The solids are deformed under the effect of external forces and the deformation is described by the physical quantity *strain*. The internal mechanical force system that resists the deformation and tends to return the solid to its undeformed initial state is described by the physical quantity *stress*. Within the elastic limit, where a complete recoverability from strain is achieved with removal of stress, stress  $\sigma$  is proportional to strain  $\epsilon$ . The generalized Hooke's law gives each of the stress tensor components as linear functions of the strain tensor components as

$$\sigma_{ij} = C_{ijkl}\epsilon_{kl}, \quad (1.7)$$

where  $C_{ijkl}$  are the elastic *stiffness* coefficients. The inverse relationship may also be written in terms of the elastic *compliance* coefficients  $S_{ijkl}$  as

$$\epsilon_{kl} = S_{ijkl}\sigma_{ij}. \quad (1.8)$$

Since both stress and strain are symmetric with respect to an interchange of the suffixes and the elastic coefficients form symmetric fourth-rank tensors, there are

21 independent elastic coefficients that can be formed into a symmetric  $6 \times 6$  matrix. In hexagonal crystals, due to additional symmetry, there remains only five independent stiffness constants:  $C_{11}$ ,  $C_{33}$ ,  $C_{12}$ ,  $C_{13}$ , and  $C_{44}$ . The stress–strain relations for the wurtzite crystal are therefore expressed as ( $c$ -axis is chosen to be the  $z$ -axis)

$$\begin{pmatrix} \sigma_{xx} \\ \sigma_{yy} \\ \sigma_{zz} \\ \sigma_{yz} \\ \sigma_{zx} \\ \sigma_{xy} \end{pmatrix} = \begin{pmatrix} C_{11} & C_{12} & C_{13} & 0 & 0 & 0 \\ C_{12} & C_{11} & C_{13} & 0 & 0 & 0 \\ C_{13} & C_{13} & C_{33} & 0 & 0 & 0 \\ 0 & 0 & 0 & C_{44} & 0 & 0 \\ 0 & 0 & 0 & 0 & C_{44} & 0 \\ 0 & 0 & 0 & 0 & 0 & (C_{11}-C_{12})/2 \end{pmatrix} \begin{pmatrix} \epsilon_{xx} \\ \epsilon_{yy} \\ \epsilon_{zz} \\ \epsilon_{yz} \\ \epsilon_{zx} \\ \epsilon_{xy} \end{pmatrix} \quad (\text{wurtzite}). \quad (1.9)$$

Similarly, the relations using the compliance matrix can be written as

$$\begin{pmatrix} \epsilon_{xx} \\ \epsilon_{yy} \\ \epsilon_{zz} \\ \epsilon_{yz} \\ \epsilon_{zx} \\ \epsilon_{xy} \end{pmatrix} = \begin{pmatrix} S_{11} & S_{12} & S_{13} & 0 & 0 & 0 \\ S_{12} & S_{11} & S_{13} & 0 & 0 & 0 \\ S_{13} & S_{13} & S_{33} & 0 & 0 & 0 \\ 0 & 0 & 0 & S_{44} & 0 & 0 \\ 0 & 0 & 0 & 0 & S_{44} & 0 \\ 0 & 0 & 0 & 0 & 0 & 2(S_{11}-S_{12}) \end{pmatrix} \begin{pmatrix} \sigma_{xx} \\ \sigma_{yy} \\ \sigma_{zz} \\ \sigma_{yz} \\ \sigma_{zx} \\ \sigma_{xy} \end{pmatrix} \quad (\text{wurtzite}). \quad (1.10)$$

In zinc blende (cubic) crystals, there are only three independent stiffness constants:  $C_{11}$ ,  $C_{12}$ , and  $C_{44}$ . The above relations then take the form

$$\begin{pmatrix} \sigma_{xx} \\ \sigma_{yy} \\ \sigma_{zz} \\ \sigma_{yz} \\ \sigma_{zx} \\ \sigma_{xy} \end{pmatrix} = \begin{pmatrix} C_{11} & C_{12} & C_{12} & 0 & 0 & 0 \\ C_{12} & C_{11} & C_{12} & 0 & 0 & 0 \\ C_{12} & C_{12} & C_{11} & 0 & 0 & 0 \\ 0 & 0 & 0 & C_{44} & 0 & 0 \\ 0 & 0 & 0 & 0 & C_{44} & 0 \\ 0 & 0 & 0 & 0 & 0 & C_{44} \end{pmatrix} \begin{pmatrix} \epsilon_{xx} \\ \epsilon_{yy} \\ \epsilon_{zz} \\ \epsilon_{yz} \\ \epsilon_{zx} \\ \epsilon_{xy} \end{pmatrix} \quad (\text{zinc blende}), \quad (1.11)$$

$$\begin{pmatrix} \epsilon_{xx} \\ \epsilon_{yy} \\ \epsilon_{zz} \\ \epsilon_{yz} \\ \epsilon_{zx} \\ \epsilon_{xy} \end{pmatrix} = \begin{pmatrix} S_{11} & S_{12} & S_{12} & 0 & 0 & 0 \\ S_{12} & S_{11} & S_{12} & 0 & 0 & 0 \\ S_{12} & S_{12} & S_{11} & 0 & 0 & 0 \\ 0 & 0 & 0 & S_{44} & 0 & 0 \\ 0 & 0 & 0 & 0 & S_{44} & 0 \\ 0 & 0 & 0 & 0 & 0 & S_{44} \end{pmatrix} \begin{pmatrix} \sigma_{xx} \\ \sigma_{yy} \\ \sigma_{zz} \\ \sigma_{yz} \\ \sigma_{zx} \\ \sigma_{xy} \end{pmatrix} \quad (\text{zinc blende}). \quad (1.12)$$

In the wurtzite phase, elastic constants  $C_{11}$  and  $C_{33}$  correspond to longitudinal modes along the  $[1000]$  and  $[0001]$  directions, respectively. Elastic constants  $C_{44}$  and  $C_{66} = (C_{11} - C_{12})/2$  (owing to symmetry) can be determined from the sound velocity of transverse modes propagating along the  $[0001]$  and  $[1000]$  directions, respectively. The remaining constant  $C_{13}$  is present in combination with four other moduli in the velocity of modes propagating in less symmetrical directions, such as  $[0011]$ . The *bulk modulus* is related to elastic constants by [85]

$$B = \frac{(C_{11} + C_{12})C_{33} - 2C_{13}^2}{C_{11} + C_{12} + 2C_{33} - 4C_{13}}. \quad (1.13)$$

Although the wurtzite ZnO crystal is acoustically anisotropic, there is only a very small difference between the shear sound velocities  $v_{TA1}$  and  $v_{TA2}$  propagating along the  $[001]$  and  $[100]$  directions, respectively ( $v_{TA2}/v_{TA1} \cong 0.98$ ). In the isotropic approximation, the Young's modulus  $E$  (in some texts  $Y$  is also used to denote the Young's modulus) and shear modulus  $G$  can also be evaluated using the relations  $E = 3B(1 - 2\nu)$  and  $G = E/2(1 + \nu)$ , respectively. The term  $\nu$  is the Poisson's ratio and is given by  $\nu = C_{13}/(C_{11} + C_{12})$ .

It has been argued that the most precise technique used to determine the elastic moduli of compound materials is ultrasonic measurement, which requires thick single crystalline samples, about 1 cm thick, to enable precise measurement of the time required for the plane-wave acoustic pulses to propagate through the crystal [86]. The measured quasilongitudinal and quasishear wave velocities can be used in the following equation to determine  $C_{13}$  [86]:

$$C_{13} = \frac{1}{\cos \alpha \sin \alpha} [(\lambda_{22} - \rho v_q^2)(\lambda_{33} - \rho v_q^2)]^{1/2} - C_{44}, \quad (1.14)$$

where for the hexagonal symmetry

$$\begin{aligned} \lambda_{22} &= C_{11} \cos^2 \alpha + C_{44} \sin^2 \alpha, \\ \lambda_{33} &= C_{44} \cos^2 \alpha + C_{33} \sin^2 \alpha. \end{aligned} \quad (1.15)$$

Here,  $\alpha$  is the angle between the propagation direction and the  $c$ -axis,  $\rho$  is the mass per unit volume, and  $v_q$  is either the quasilongitudinal or the quasishear velocity.

As an optical technique, Brillouin scattering allows the determination of the elastic constants and hence of the bulk moduli through the interaction of light with thermal excitation in a material, in particular acoustic phonons in a crystal. In this technique, the elastic constants  $C_{11}$  and  $C_{66}$  can be directly obtained from measurement of the phase velocity of the longitudinal mode and of the shear horizontal mode traveling parallel to the crystal surface. The remaining constants,

$C_{13}$ ,  $C_{33}$ , and  $C_{44}$ , can be evaluated from measurement of the phase velocity of the Rayleigh surface wave and of the longitudinal bulk acoustic wave propagating at different angles from the surface normal. Various forms of X-ray diffraction, such as energy dispersive X-ray diffraction, angular dispersive X-ray diffraction (ADX), and X-ray absorption spectroscopy (XAS) can also be employed to determine the pressure dependence of the lattice parameters. From that, experimental equation of state (EOS), a widely used approach being the Murnaghan's equation of state and hence directly the bulk modulus, which is based on the assumption that the bulk modulus has a linear dependence on pressure  $P$ , can be deduced as [87]

$$V = V_0 \left( 1 + \frac{B'P}{B} \right)^{-1/B'} \quad (1.16)$$

where  $B$  and  $V_0$  represent the bulk modulus and unit volume at ambient pressure, respectively, and  $B'$  is the derivative of  $B$  with respect to pressure. X-ray diffraction leads to the determination of the isothermal bulk modulus, whereas Brillouin scattering leads to the adiabatic one. Nevertheless, in solids other than molecular solids there is no measurable difference between the two thermodynamic quantities. Besides the experimental investigations, many theoretical calculations have also been employed to determine the structural and mechanical properties of ZnO. Most of the calculations are based on density functional theory within the local density approximation using various types of exchange correlation functions and either plane-wave expansion for the pseudopotentials or the LMTO method.

Among the tetrahedrally bonded semiconductors, ZnO has the highest piezoelectric constants with electromechanical coupling larger than that in GaN and AlN [88]. This property makes it a technologically important material for many applications such as piezotransducers that require a large electromechanical coupling, which will be discussed in the context of piezoelectric devices in Section 8.6. In piezoelectric crystals, electrical polarization is produced in the presence of stress, which is described by using the piezoelectric strain coefficients  $e_{ijk}$  and piezoelectric stress coefficients  $d_{ijk}$  as

$$P_i = e_{ijk}\epsilon_{jk} = d_{ijk}\sigma_{jk}. \quad (1.17)$$

$d_{ijk}$  are also referred to as electromechanical constants as it is also possible to produce strain when the crystal is subjected to an electric field with components  $E_k$ :

$$\epsilon_{ij} = d_{ijk}E_k. \quad (1.18)$$

Since the stress is a symmetric second-rank tensor, piezoelectric tensor has 18 independent elements forming a  $3 \times 6$  matrix. Due to crystal symmetry, there remain

only three independent components ( $e_{31}$ ,  $e_{33}$ , and  $e_{15}$ ) in hexagonal wurtzite phase and one ( $e_{14}$ ) in the cubic zinc blende phase, which characterize the full piezoelectric tensors of such crystals [89]. The polarization is then written as

$$\begin{pmatrix} P_{xx} \\ P_{yy} \\ P_{zz} \end{pmatrix} = \begin{pmatrix} 0 & 0 & 0 & 0 & e_{15} & 0 \\ 0 & 0 & 0 & e_{15} & 0 & 0 \\ e_{31} & e_{31} & e_{33} & 0 & 0 & 0 \end{pmatrix} \begin{pmatrix} \varepsilon_{xx} \\ \varepsilon_{yy} \\ \varepsilon_{zz} \\ \varepsilon_{xy} \\ \varepsilon_{yz} \\ \varepsilon_{zx} \end{pmatrix} = \begin{pmatrix} 0 & 0 & 0 & 0 & d_{15} & 0 \\ 0 & 0 & 0 & d_{15} & 0 & 0 \\ d_{31} & d_{31} & d_{33} & 0 & 0 & 0 \end{pmatrix} \begin{pmatrix} \sigma_{xx} \\ \sigma_{yy} \\ \sigma_{zz} \\ \sigma_{xy} \\ \sigma_{yz} \\ \sigma_{zx} \end{pmatrix} \quad (\text{wurtzite}), \quad (1.19)$$

$$\begin{pmatrix} P_{xx} \\ P_{yy} \\ P_{zz} \end{pmatrix} = \begin{pmatrix} 0 & 0 & 0 & e_{14} & 0 & 0 \\ 0 & 0 & 0 & 0 & e_{14} & 0 \\ 0 & 0 & 0 & 0 & 0 & e_{14} \end{pmatrix} \begin{pmatrix} \varepsilon_{xx} \\ \varepsilon_{yy} \\ \varepsilon_{zz} \\ \varepsilon_{xy} \\ \varepsilon_{yz} \\ \varepsilon_{zx} \end{pmatrix} = \begin{pmatrix} 0 & 0 & 0 & d_{14} & 0 & 0 \\ 0 & 0 & 0 & 0 & d_{14} & 0 \\ 0 & 0 & 0 & 0 & 0 & d_{14} \end{pmatrix} \begin{pmatrix} \sigma_{xx} \\ \sigma_{yy} \\ \sigma_{zz} \\ \sigma_{xy} \\ \sigma_{yz} \\ \sigma_{zx} \end{pmatrix} \quad (\text{zincblende}). \quad (1.20)$$

As seen from Equation 1.19, two of the piezoelectric components in wurtzite phase measure the polarization induced along the  $c$ -axis, at zero electric field, by a uniform strain either along the  $c$ -axis or in the basal plane. The relevant relationship is [90]

$$P_z^{\text{piezo}} = e_{33}\varepsilon_z + e_{31}\varepsilon_{\perp}, \quad (1.21)$$

where  $\varepsilon_z$  and  $\varepsilon_{\perp}$  are the strains along the  $c$ -axis and in the basal plane, respectively. The third independent component of piezoelectric tensor,  $e_{15}$ , describes the polarization induced by a shear strain, which is usually neglected for simplicity. The sign of the piezoelectric tensor is generally fixed assuming that the positive direction along  $c$ -axis goes from the cation to the anion.

The natural structure of ZnO is wurtzite, which has low symmetry resulting in the existence of spontaneous polarization along the  $c$ -direction. However, the absolute value of the spontaneous polarization in a nonferroelectric material has never been directly measured, while one invariably measures the polarization derivatives. In semiconductors, the spontaneous polarization may be deduced by investigating the two-dimensional electron gas and the redshift of the transitions in quantum wells albeit indirectly. From the theoretical point of view, there have been some efforts in

determining the value of the spontaneous polarization in ZnO. One conventional approach is to define the spontaneous polarization of a low-symmetry crystal (wurtzite) as the polarization difference with respect to a high-symmetry structure (zinc blende) of the same material.

The micro- and nanoindentation methods have been widely used to determine the hardness of ZnO over a wide range of size scales and temperatures. Hardness measurements are usually carried out on the (0001) surface of the crystal using the conventional pyramidal or spherical diamond tip, or alternatively, with a sharp triangular indenter. The depth-sensing indentation measurements provide the complete information on the hardness and pressure-induced phase transformation of semiconductor materials. Table 1.6 shows the measured and calculated mechanical parameters for ZnO crystallized in the form of wurtzite, zinc blende, and rocksalt phases.

For ZnO, theoretical predictions appear to be in good agreement with experimental findings for certain bulk material properties. The quality of the crystals and theoretical approximations are of primary importance for the precise determination of the physical properties. In regard to the elastic constants, theory and experiments seem capable of producing data that are quite consistent for wurtzite-phase ZnO. Bulk modulus and its rate of change with pressure for all phases are in good agreement within the various experimental findings as well as the theoretical predictions with a few exceptions. Any deviation can be attributed to the sample quality, the accuracy of each experimental method, and phonon dispersion. Each calculation method also has its own limitations related to the basic material parameters, basis sets, and the precisions used in addition to the approximations of the method itself, leading to variations in the calculated parameters. Compared to group III nitrides (e.g., for GaN  $C_{11} = 296$  GPa,  $C_{12} = 130$  GPa,  $C_{13} = 120$  GPa,  $C_{33} = 395$  GPa,  $C_{44} = 241$  GPa,  $B = 190\text{--}245$  GPa, see Chapter 2 in Ref. [91]), the elastic and bulk moduli of ZnO are small. Ultrasonic experiments on single-crystal specimens of the wurtzite (B4) phase of ZnO have shown that, under pressure, this material becomes softer against shear-type acoustic distortions.

Decremps *et al.* [92] have studied the pressure behavior of both longitudinal ( $C_{11}$  and  $C_{33}$ ) and transverse ( $C_{44}$  and  $C_{66}$ ) elastic moduli for the wurtzite phase of single-crystal ZnO using ultrasonic wave velocity measurements up to 10 GPa at three different temperatures. As shown in Figure 1.16, it has been observed that all the moduli exhibit a linear dependence on pressure up to the phase transition pressures, with positive values for the room-temperature longitudinal moduli ( $dC_{11}/dP = 5.32$  and  $dC_{33}/dP = 3.78$ ) but negative values for the shear moduli ( $dC_{44}/dP = -0.35$  and  $dC_{66}/dP = -0.30$ ). At high temperatures, the pressure derivatives of the elastic shear modes become more negative. Thus, the elastic shear softening observed at room temperature is enhanced at elevated temperatures. The effect of phonons and the role of bond-bending forces as a function of pressure in causing the elastic softening have also been investigated [92]. It has been observed that the pressure at which the phase transition (B4  $\rightarrow$  B1) commences decreases to about 6 GPa at 600 °C compared to 7.5 GPa at room temperature.

Table 1.6 Some mechanical properties of ZnO obtained by several experimental techniques and theoretical calculations.

Parameters	Wurtzite	Zinc blende	Rocksalt
$C_{11}$ (GPa)	209.7 <sup>a</sup> , 206 <sup>b</sup> , 157 <sup>c</sup> , 190 <sup>d</sup> , 207 <sup>e</sup> , 209 <sup>f</sup> , 230 <sup>g</sup> , 231 <sup>h</sup> , 246 <sup>i</sup>	193 <sup>j</sup>	
$C_{12}$ (GPa)	121.1 <sup>a</sup> , 117 <sup>b</sup> , 89 <sup>c</sup> , 110 <sup>d</sup> , 117.7 <sup>e</sup> , 85 <sup>f</sup> , 82 <sup>g</sup> , 111 <sup>h</sup> , 127 <sup>i</sup>	139 <sup>j</sup>	
$C_{13}$ (GPa)	105.1 <sup>a</sup> , 118 <sup>b</sup> , 83 <sup>c</sup> , 90 <sup>d</sup> , 106.1 <sup>e</sup> , 95 <sup>f</sup> , 64 <sup>g</sup> , 104 <sup>h</sup> , 105 <sup>i</sup>		
$C_{33}$ (GPa)	210.9 <sup>a</sup> , 211 <sup>b</sup> , 208 <sup>c</sup> , 196 <sup>d</sup> , 209.5 <sup>e</sup> , 270 <sup>f</sup> , 247 <sup>g</sup> , 183 <sup>h</sup> , 246 <sup>i</sup>		
$C_{44}$ (GPa)	42.47 <sup>a</sup> , 44.3 <sup>b</sup> , 38 <sup>c</sup> , 39 <sup>d</sup> , 44.8 <sup>e</sup> , 46 <sup>f</sup> , 75 <sup>g</sup> , 72 <sup>h</sup> , 56 <sup>i</sup>	96 <sup>j</sup>	
$C_{66}$ (GPa)	44.29 <sup>a</sup> , 44.6 <sup>b</sup> , 34 <sup>c</sup> , 40 <sup>d</sup> , 44.6 <sup>e</sup> , 62 <sup>f</sup> , 60 <sup>h</sup> , 115 <sup>i</sup>		
Bulk modulus, $B$ (GPa)	142.4 <sup>f</sup> , 183 <sup>g</sup> , 170 <sup>h</sup> , 160 <sup>m</sup> , 162.3 <sup>n</sup> , 133.7 <sup>o</sup> , 156.8 <sup>k</sup>	161.7 <sup>n</sup> , 135.3 <sup>o</sup> , 154.4 <sup>k</sup>	202.5 <sup>j</sup> , 228 <sup>p</sup> , 205 <sup>m</sup> , 205.7 <sup>n</sup> , 172.7 <sup>o</sup> , 203.3 <sup>k</sup>
$dB/dP$	3.6 <sup>f</sup> , 4.0 <sup>p</sup> , 4.4 <sup>m</sup> , 4.05 <sup>n</sup> , 3.83 <sup>o</sup> , 3.6 <sup>k</sup>	3.95 <sup>n</sup> , 3.72 <sup>o</sup> , 3.6 <sup>k</sup>	3.54 <sup>j</sup> , 4.0 <sup>p</sup> , 4.88 <sup>m</sup> , 3.90 <sup>n</sup> , 3.77 <sup>o</sup> , 3.6 <sup>k</sup>
Young's modulus, $E$ (GPa)	111.2 ± 4.7 <sup>q</sup>		
Hardness (GPa)	5.0 ± 0.1 <sup>r</sup>		
$\epsilon_{31}$ (C m <sup>-2</sup> )	-0.62 <sup>r</sup> , -0.51 <sup>c</sup> , -0.39 <sup>s</sup> , -0.53 <sup>t</sup> , -0.51 <sup>u</sup> , -0.55 <sup>j</sup> , -0.66 <sup>v</sup>		
$\epsilon_{33}$ (C m <sup>-2</sup> )	0.96 <sup>t</sup> , 1.22 <sup>c</sup> , 0.92 <sup>s</sup> , 1.19 <sup>f</sup> , 1.21 <sup>u</sup> , 1.19 <sup>j</sup> , 1.19 <sup>v</sup>		
$\epsilon_{15}$ (C m <sup>-2</sup> )	-0.37 <sup>r</sup> , -0.45 <sup>c</sup> , -0.46 <sup>j</sup>		
$\epsilon_{14}$ (C m <sup>-2</sup> )		0.69 <sup>j</sup> , 0.64 <sup>w</sup>	
Spontaneous polarization (C m <sup>-2</sup> )	-0.057 <sup>t</sup> , -0.047 <sup>x</sup> , -0.057 <sup>u</sup>		
Born effective charge, $Z^*$	2.06 <sup>t</sup> , 2.11 <sup>u</sup> , 2.10 <sup>w</sup> , 2.1 <sup>x</sup>		

<sup>a</sup>Ultrasonic measurement on single-crystal ZnO grown by chemical reaction in vapor state [86].

<sup>b</sup>Surface Brillouin scattering on polycrystalline ZnO film deposited by RF sputtering on (1 0 0) Si substrate [96].

<sup>c</sup>Acoustic investigation technique on ZnO film deposited by RF magnetron sputtering on sapphire substrate [97].

<sup>d</sup>Polarized Brillouin scattering on bulk ZnO single crystal [98].

<sup>e</sup>Ultrasonic resonance method on ZnO single crystal [99].

<sup>f</sup>Calculated by using LDA [14].

<sup>g</sup>Calculated by using GGA [14].

<sup>h</sup>Atomistic calculations based on an interatomic pair potential within the shell model approach [19].

<sup>i</sup>Calculated by using *ab initio* periodic LCAO method, based mainly on the Hartree-Fock Hamiltonian, with an all-electron Gaussian-type basis set [32].

<sup>j</sup>X-ray diffraction by using synchrotron radiation on polycrystalline ZnO (99.99% purity) [12].

- <sup>k</sup>Calculation based on *ab initio* all-electron periodic Hartree–Fock linear combination of atomic orbitals [20].
- <sup>l</sup>Calculation using molecular dynamics simulation based on Tersoff’s potential [100].
- <sup>m</sup>Calculation based on modern theoretical HF cluster and full potential scalar relativistic linearized augmented plane wave [13].
- <sup>n</sup>Calculated by using LDA [18].
- <sup>o</sup>Calculated by using GGA [18].
- <sup>p</sup>X-ray diffraction and <sup>67</sup>Zn Mössbauer spectroscopy on bulk ZnO [13].
- <sup>q</sup>Spherical nanoindentation on bulk ZnO [101].
- <sup>r</sup>Resonance–antiresonance method on ZnO single crystal [99].
- <sup>s</sup>Calculated using modern *ab initio* [88].
- <sup>t</sup>Calculated using modern *ab initio* quantum mechanical level by using through the Berry-phase scheme applied to delocalized crystalline orbitals and through the definition of well-localized Wannier functions [33].
- <sup>u</sup>Calculation based on *ab initio* using the Berry-phase approach to polarization in solids [90].
- <sup>v</sup>Calculation by using a plane-wave pseudopotential implementation of density functional theory and density functional linear response within the local density approximation [82].
- <sup>w</sup>Ref. [102].
- <sup>x</sup>Calculated by using the LDA, HF, and a model GW scheme [46].

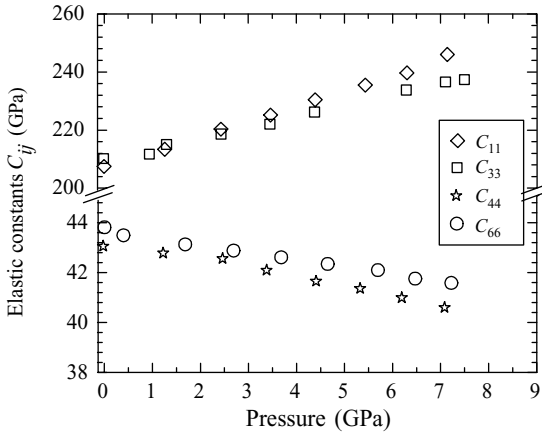


**Figure 1.16** Elastic moduli of ZnO versus pressure at ambient temperature. The slope of the  $C_{11}$  and  $C_{33}$  pressure dependence is positive ( $dC_{11}/dP = 5.32$  and  $dC_{33}/dP = 3.78$ ), whereas that for  $C_{44}$  and  $C_{66}$  is negative ( $dC_{44}/dP = -20.35$  and  $dC_{66}/dP = -20.30$ ). (Courtesy of F. Decremps [92].)

Similar pressure dependence was also reported by Soga and Anderson [93], who measured the pressure dependence of the room-temperature longitudinal (L) and transverse (T) sound velocities of polycrystalline ZnO. They obtained  $(\partial v_L/\partial P)_T = 3.64 \text{ 331 023 km s}^{-1} \text{ kbar}^{-1}$  and  $(\partial v_T/\partial P)_T = 23.193 \text{ 310 23 km s}^{-1} \text{ kbar}^{-1}$ , corresponding to  $(\partial B/\partial P)_T = 4.8$  and  $(\partial G/\partial P)_T = -0.71$  ( $B$  is the bulk modulus and  $G$  is the shear modulus). On the theoretical side, a linear evolution under pressure was calculated for the two longitudinal modes  $C_{11}$  and  $C_{33}$  with pressure derivatives of 3.18 and 1.72, respectively, using atomistic calculations based on an interatomic pair potential within the shell model approach [19]. The shear moduli  $C_{44}$  and  $C_{66}$  exhibited negative pressure dependence with pressure derivatives of  $-0.30$  and  $-0.84$ , respectively. The experimental and calculated values deviated some. The unusual negative values for both shear modes were attributed to two simultaneous effects [92]: (i) a major contribution of the second-nearest-neighbor interactions to the transverse acoustic phonon modes and (ii) an enhancement of the Coulomb forces screening between an atom and its second-nearest neighbor. Another explanation for the observed shear softening of ZnO was attributed to the decrease of bond-bending forces.

The deformation behavior of bulk ZnO single crystals was studied by a combination of spherical nanoindentation and atomic force microscopy [101]. ZnO exhibited plastic deformation for relatively low loads ( $>4\text{--}13 \text{ mN}$  with  $a \sim 4.2 \text{ mm}$  radius spherical indenter). The average contact pressure hardness  $H$  and Young's modulus  $E$  as a function of indenter penetration were determined by analyzing partial load-unload data. The hardness value of ZnO is measured to be  $5.0 \pm 0.1 \text{ GPa}$  at a plastic penetration depth of 300 nm. The Young's modulus remained essentially constant over the indenter penetration depth, with  $E = 111.2 \pm 4.7 \text{ GPa}$ . Previous indentation studies performed mostly on polycrystalline ZnO have reported a wide range of  $H$  ( $\sim 1.5\text{--}12 \text{ GPa}$ ) and  $E$  ( $\sim 40\text{--}120 \text{ GPa}$ ) values. However, it should be noted

from these results that ZnO is significantly softer than GaN, where  $H(\text{GaN}) = 15.5 \pm 0.9 \text{ GPa}$  and  $E(\text{GaN}) = 210 \pm 23 \text{ GPa}$  [94]. The lower value of  $H$  for ZnO is, in fact, expected due to a lower melting point ( $1975 \text{ }^\circ\text{C}$ ) and larger ionicity (0.616) compared to that of GaN ( $2500 \text{ }^\circ\text{C}$  and 0.500, respectively) [95].

The spontaneous and piezoelectric polarization in ZnO have been studied theoretically by a number of groups and compared with a few available indirect experimental results. Dal Corso *et al.* [88] demonstrated applicability of *ab initio* studies of piezoelectricity within an all-electron scheme. A comparative analysis was performed to understand the microscopic origin of the peculiar behavior of ZnO. They have concluded that the piezoelectric effect results from two different contributions of opposite sign, which were referred to as the “clamped ion” and “internal strain.” It has been shown that large piezoelectric tensor of ZnO is due to the low value of its clamped ion contribution (reducing the cancellation effect); besides, the piezoelectric tensor is dominated by the internal relaxation of anion and cation sublattices induced by the macroscopic strain. The piezoelectric tensor in ZnO has been calculated by using various techniques such as plane-wave analysis and ultrasoft pseudopotentials, and a GGA Hamiltonian, an all-electron basis set, and a HF Hamiltonian. The values of  $e_{31}$  and  $e_{33}$  were reported in the range of 0.39–0.66 (mostly,  $\sim 0.52 \text{ C m}^{-2}$ ) and 0.92–1.30  $\text{C m}^{-2}$  (mostly  $\sim 1.20 \text{ C m}^{-2}$ ), respectively, which were in satisfactory agreement with the experimental data as tabulated in Table 1.6.

Furthermore, the spontaneous polarization of ZnO has also been computed and compared with a very indirect experimental estimate of the same quantity. Massidda *et al.* [46] calculated *ab initio* the electronic states, spontaneous polarization, and Born dynamical charge of ZnO by using the LDA, HF, and a model GW scheme. Among these schemes, the GW scheme gives a spontaneous polarization value of  $-0.047 \text{ C m}^{-2}$ , which is about 0.010 smaller than the other two reports ( $-0.057 \text{ C m}^{-2}$  [88, 90]). Although there are no direct experimental data available, these theoretical predictions are in good agreement with an indirect experimental value of  $-0.07 \pm 0.02 \text{ C m}^{-2}$  obtained from a model based on nonlinear optics. For Born dynamical charge, theoretical calculations and experimental data match quite well. From the value of the calculated Born dynamical charge,  $\sim 2.1$ , it has been suggested that rigid-ion-like behavior of ZnO is dominant and its band-by-band decomposition has anomalous contributions from O 2s, Zn 3d, and O 2p bands, indicating a substantial interaction between the corresponding occupied atomic orbitals.

Hill and Waghmare [82] have also performed a first-principles study of the piezoelectric ZnO, named after the application, as a function of stress and temperature using a plane-wave pseudopotential implementation of density functional theory and density functional linear response within the local density approximation. The results are shown in Figure 1.17. The piezoelectric constant is strongly sensitive to both temperature and stress changing by about 20 and 15–30%, respectively, over the range of parameters considered. By analyzing various physical contributions, these dependences were primarily attributed to the changes in structural parameters as manifested through the phonon and strain coupling. The strong bond length dependent hybridization between the O 2p and Zn 3d electrons was believed to be the cause of the large magnitude and sensitivity of this coupling.

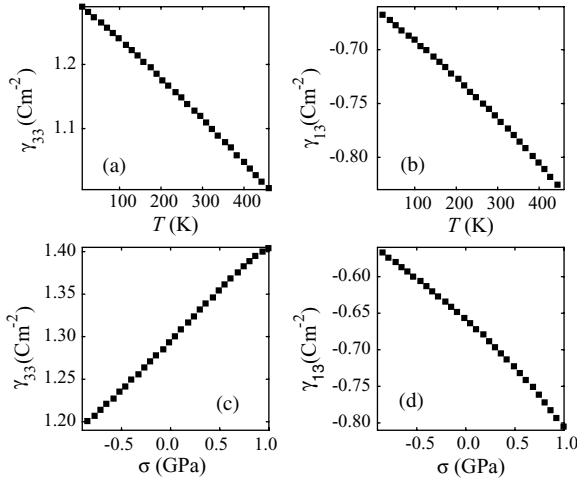


**Figure 1.17** Dependence of piezoelectric constants  $\gamma_{33}$  and  $\gamma_{13}$  of ZnO on temperature (a and b) and stress (c and d), respectively.  $\gamma_{ij}$  used by Hill and Waghmare correspond to  $e_{ij}$  used here. (After Ref. [82].)

As alluded to earlier, ZnO is widely used in electroacoustic devices due to its large piezoelectricity (see Section 8.6 for a discussion of the piezoelectric devices). Therefore, a brief discussion of the acoustic wave propagation in wurtzite ZnO is warranted. The velocity of the acoustic wave propagation in semiconductors depends on the stiffness parameters. The three-dimensional equation of motion governing the macroscopic lattice displacement  $\mathbf{u}$  as a function of time is [103]

$$\rho \frac{\partial^2 \mathbf{u}}{\partial t^2} = \nabla \cdot \boldsymbol{\sigma}, \quad (1.22)$$

where  $\rho$  is the mass density and  $\boldsymbol{\sigma}$  is the stress tensor. If we choose the  $c$ -direction as the  $z$ -direction, using the stress-strain relation in Equation 1.9 and the definition of the strain tensor  $\boldsymbol{\epsilon} = \nabla \mathbf{u}$ , the acoustic phonon wave equations in wurtzite crystals are obtained as [103]

$$\begin{aligned} \rho \frac{\partial^2 u_x}{\partial t^2} &= C_{11} \frac{\partial^2 u_x}{\partial x^2} + \frac{(C_{11} - C_{12})}{2} \frac{\partial^2 u_x}{\partial y^2} + C_{44} \frac{\partial^2 u_x}{\partial z^2} + \frac{(C_{11} + C_{12})}{2} \frac{\partial^2 u_y}{\partial x \partial y} \\ &+ (C_{13} + C_{44}) \frac{\partial^2 u_z}{\partial x \partial z}, \quad \rho \frac{\partial^2 u_y}{\partial t^2} = C_{11} \frac{\partial^2 u_y}{\partial y^2} + \frac{(C_{11} - C_{12})}{2} \frac{\partial^2 u_y}{\partial x^2} + C_{44} \frac{\partial^2 u_y}{\partial z^2} \\ &+ \frac{(C_{11} + C_{12})}{2} \frac{\partial^2 u_x}{\partial x \partial y} + (C_{13} + C_{44}) \frac{\partial^2 u_z}{\partial y \partial z}, \quad \rho \frac{\partial^2 u_z}{\partial t^2} = C_{33} \frac{\partial^2 u_z}{\partial z^2} + C_{44} \left( \frac{\partial^2 u_z}{\partial x^2} + \frac{\partial^2 u_z}{\partial y^2} \right) \\ &+ (C_{13} + C_{44}) \left( \frac{\partial^2 u_x}{\partial x \partial z} + \frac{\partial^2 u_y}{\partial z \partial y} \right). \end{aligned} \quad (1.23)$$

Assuming a solution in the form  $\mathbf{u}(t) = (u_x \hat{x} + u_y \hat{y} + u_z \hat{z})e^{i(\mathbf{q} \cdot \mathbf{r} - \omega t)}$ , with  $\omega$  being the angular frequency and  $\mathbf{r}$  the position vector, and choosing the  $y$ -axis such that the wave vector  $\mathbf{q}$  lies in the  $yz$  plane, we may write the wave equations as

$$\begin{aligned}\rho\omega^2 u_x &= \frac{1}{2}(C_{11} - C_{12})(q \sin \theta)^2 u_x + C_{44}(q \cos \theta)^2 u_x, \\ \rho\omega^2 u_y &= C_{11}(q \sin \theta)^2 u_y + C_{44}(q \cos \theta)^2 u_y + (C_{13} + C_{44})q^2 \sin \theta \cos \theta u_z, \\ \rho\omega^2 u_z &= C_{33}(q \cos \theta)^2 u_z + C_{44}(q \sin \theta)^2 u_z + (C_{13} + C_{44})q^2 \sin \theta \cos \theta u_y,\end{aligned}\tag{1.24}$$

where  $\theta$  is the angle between  $\mathbf{q}$  and the  $z$ -axis ( $c$ -axis). For  $\theta = 0$ , these equations reduce to

$$\begin{aligned}\rho\omega^2 u_x &= C_{44}q^2 u_x, \\ \rho\omega^2 u_y &= C_{44}q^2 u_y, \\ \rho\omega^2 u_z &= C_{33}q^2 u_z.\end{aligned}\tag{1.25}$$

It is clear that there are two acoustic waves: transverse ( $x$ - $y$ ) and longitudinal ( $z$ ), with velocities  $v_z = \sqrt{C_{33}/\rho}$  and  $v_{xy} = \sqrt{C_{44}/\rho}$ , respectively. As will be discussed in Section 8.6, the electromechanical coupling results in an increase in the stiffness and therefore the sound velocity. For longitudinal acoustic wave propagation (i.e., along the  $c$ -axis), the effective stiffness constant including the electromechanical coupling becomes  $C_{33,s} = C_{33}(1 + K^2)$ , where  $K^2$  is called the electromechanical constant. The resulting acoustic velocity is then

$$v_{z,s} = \sqrt{\frac{C_{33}(1 + K^2)}{\rho}}.\tag{1.26}$$

An electromechanical coupling constant of 6% has been measured for ZnO [104], which would increase the sound velocity significantly, by  $\sim 3\%$ .

## 1.5 Vibrational Properties

A fundamental understanding of the thermal and electrical properties in terms of low- and high-field carrier transport requires precise knowledge of the vibrational modes of the single crystal, which are related to mechanical properties and can be construed as such. Vibrational properties of ZnO probed by techniques such as Raman scattering were determined early on [105–111]. Here, phonons have been arbitrarily chosen to be discussed under the mechanical properties of the crystal rather than under its optical properties. A succinct discussion of vibrational modes,

**Table 1.7** Acoustic and optical phonon modes in a crystal with wurtzite symmetry where  $s$  represents the number of atoms in the basis.

Mode type	Number of modes
Longitudinal acoustic	1
Transverse acoustic	2
Total acoustic modes	3
Longitudinal optical	$s - 1$
Transverse optical	$2s - 2$
All optical modes	$3s - 3$
All modes	$3s$

The  $s$  parameter for wurtzite symmetry is 4. This table is also applicable to the zinc blende case but with  $s = 2$ .

some of which are active Raman modes, some are active in IR measurements, and some are optically inactive (silent) modes, is provided [112]. Vibrational modes, which go to the heart of the mechanical properties, are very sensitive to crystalline defects, strain, and dopant in that the phonon mode frequencies and their frequency broadening can be used to glean very crucial information about the semiconductor. The method can also be applied to heterostructures and strained systems. Electronic Raman measurements can be performed to study processes such as electron–phonon interaction in the CW or time-resolved schemes. Time-resolved Raman measurements as applied to hot electron and phonon processes under high electric fields have important implications for carrier velocities.

In the case of wurtzite ZnO (similar to the case of wurtzitic nitrides) [113], the number of atoms per unit cell  $s = 4$ , and there is a total of 12 phonon modes, namely, 1 longitudinal acoustic (LA), 2 transverse acoustic (TA), 3 longitudinal optical (LO), and 6 transverse optical (TO) branches, the details of which are listed in Table 1.7. In the zinc blende polytypes with  $s = 2$ , only six modes are present, three of which are acoustical (one LA and two TA) and the other three are optical (one LO and two TO) branches. Infrared (IR) reflection and Raman spectroscopies have been commonly employed to derive zone center and some zone boundary phonon modes in ZnO. In the hexagonal structures with  $C_{6v}^4$  symmetry, group theory predicts eight sets of phonon normal modes at the  $\Gamma$  point, namely,  $2A_1 + 2E_1 + 2B_1 + 2E_2$ . Among them, one set of  $A_1$  and  $E_1$  modes are acoustic, while the remaining six modes, namely,  $A_1 + E_1 + 2B_1 + 2E_2$ , are optical modes. In a more simplified manner, one can consider that the stacking order of the Wz polytype is AaBb while that for the zinc blende variety is AaBbCc. In addition, the unit cell length of the cubic structure along  $[1\ 1\ 1]$  is equal to the width of one unit bilayer, while that of the hexagonal structure along  $[000\ 1]$  is twice that amount. Consequently, the phonon dispersion of the hexagonal structure along  $[000\ 1]$  ( $\Gamma \rightarrow A$  in the Brillouin zone) is approximated by folding the phonon dispersion for the zinc blende structure along the  $[1\ 1\ 1]$  ( $\Gamma \rightarrow L$ ) direction [114], as shown in Figure 1.18. Doing so reduces the TO phonon mode at the L point of the Brillouin zone in the zinc blende structure to the  $E_2$  mode at the  $\Gamma$  point

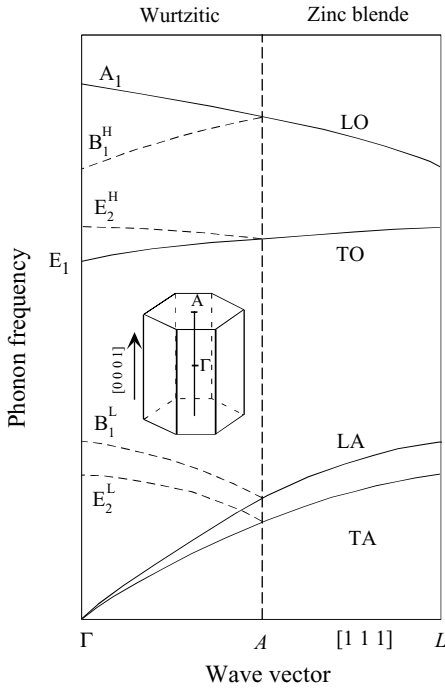


**Figure 1.18** Schematic depiction of the phonon dispersion curves for zinc blende and Wz structures. Also shown are the  $\Gamma$  and A points of the zone in relation to the real-space hexagonal structure. Phonon branches along the  $[1\ 1\ 1]$  direction in the zinc blende structure are folded to approximate those of the wurtzite structure along the  $[000\ 1]$  direction because the unit cell length of the cubic structure along the  $[1\ 1\ 1]$  direction is equal to the width of one unit bilayer, while that for the hexagonal structure along the  $[000\ 1]$  direction is twice that amount. (Patterned after Ref. [114].)

of the Brillouin zone in the hexagonal structure. This vibrational mode is denoted as  $E_2^H$  with superscript H depicting the higher frequency branch of the  $E_2$  phonon mode. In addition, one  $A_1$  and one  $B_1$  mode ( $B_1^H$ ) derive from a singly degenerate LO phonon branch of the zinc blende system by zone folding, while one  $E_1$  mode together with  $E_2^H$  derive from a doubly degenerate TO mode in the cubic system. As indicated in the figure, there is another  $E_2$  mode at lower frequency labeled as  $E_2^L$ . This has its genesis in zone folding of the TA mode in the zinc blende structure. It should be noted that in the hexagonal structure, there is anisotropy in the macroscopic electric field induced by polar phonons. As a result, both TO and LO modes split into the axial (or  $A_1$ ) and planar (or  $E_1$ ) type modes where atomic displacement occurs along the  $c$ -axis or perpendicular to the  $c$ -axis, respectively. This splitting is not shown in Figure 1.18 as it is very small, just a few meV. Because the space group  $C_{6v}$  describes the crystalline structure of the wurtzite ZnO compound with two formula units in the primitive cell, the optical phonons at the  $\Gamma$  point of the Brillouin zone belong to the following irreducible representation. The  $A_1$  and  $E_1$  branches are both Raman and infrared active, the two nonpolar  $E_2$  branches are Raman active only, and the  $B_1$  branches are

inactive (silent modes). The  $A_1$  and  $E_1$  modes are each split into LO and TO components with different frequencies due to the macroscopic electric fields associated with the LO phonons. Because the electrostatic forces dominate the anisotropy in the short-range forces, the TO–LO splitting is larger than the  $A_1$ – $E_1$  splitting. For the lattice vibrations with  $A_1$  and  $E_1$  symmetry, the atoms move parallel and perpendicular to the  $c$ -axis, respectively. The low-frequency  $E_2$  mode is associated with the vibration of the heavy Zn sublattice, while the high-frequency  $E_2$  mode involves only the oxygen atoms. In the case of highly oriented ZnO films, if the incident light is exactly normal to the surface, only  $A_1(\text{LO})$  and  $E_2$  modes are observed and the other modes are forbidden according to the Raman selection rules.

The first-order phonon Raman scattering is due to phonons near the  $\Gamma$  point zone center, that is, with wave vector  $k \approx 0$ , because of the momentum conservation rule in the light scattering process. Raman measurements are typically employed to probe the vibrational properties of semiconductors. When done along the direction perpendicular to the (0001) plane, the nomenclature used to describe this configuration is depicted as  $Z(XY, XY)\bar{Z}$ . Here, following Porto's notation [105], A(B,C)D is used to describe the Raman geometry and polarization where A and D represent the wave vector direction of the incoming and scattered light, respectively, whereas B and C represent the polarization of the incoming and scattered light. In Raman scattering, all the above-mentioned modes, with the exception of  $B_1$  modes, are optically active. Because of their polar nature, the  $A_1$  and  $E_1$  modes split into longitudinal optical ( $A_1$ -LO and  $E_1$ -LO), meaning beating along the  $c$ -axis, and transverse optical ( $A_1$ -TO and  $E_1$ -TO), meaning beating in the basal plane. To reiterate, the  $A_1$  and  $B_1$  modes give atomic displacements along the  $c$ -axis, while the others,  $E_1$  and  $E_2$ , give atomic displacements perpendicular to the  $c$ -axis. Here, the  $A_1$  and  $E_1$  modes are both Raman and IR active, while the two  $E_2$  modes are only Raman active, and the two  $B_1$  modes are neither Raman nor IR active, meaning silent modes. In the  $Z(XY, XY)\bar{Z}$  configuration, only the  $E_2^L$  (or  $E_2^L$  or  $E_2$ -low),  $E_2^H$  (or  $E_2^H$  or  $E_2$ -high), and  $A_1(\text{LO})$  modes should be observable. In particular, in the  $Z(X, X)\bar{Z}$  and  $Z(Y, Y)\bar{Z}$  geometries all three modes are observable, while in the  $Z(X, Y)\bar{Z}$  or  $Z(Y, X)\bar{Z}$  geometries only the  $E_2$  modes are detected [106]. The details of the mode–Raman configuration relationship are provided in Table 1.8. Shown in Figure 1.19 are the modes and the Raman backscattered geometries in relation to hexagonal crystalline orientation that can be used to sense the various phonon modes indicated.

The acoustic modes are simple translational modes, and optical modes for wurtzite symmetry are shown in Figure 1.20. Table 1.9 gives a list of observed zone center optical phonon wave numbers along with those calculated for wurtzite ZnO.

The optical phonon energies are linked to the low- and high-frequency dielectric constants and therefore can be calculated from one another. Electromagnetic theory indicates that for any longitudinal electromagnetic wave to propagate, the dielectric function  $\epsilon(\omega)$  must vanish. Doing so leads to [113]

$$\frac{\epsilon(\omega)}{\epsilon(\infty)} = \frac{\omega_{\text{LO}}^2 - \omega^2}{\omega_{\text{TO}}^2 - \omega^2}, \quad (1.27)$$

**Table 1.8** Raman measurement configuration needed to observe the phonon modes in hexagonal ZnO.

Mode	Configuration
A <sub>1</sub> (TO), E <sub>2</sub>	X(Y, Y) $\bar{X}$
A <sub>1</sub> (TO)	X(Z, Z) $\bar{X}$
E <sub>1</sub> (TO)	X(Z, Y) $\bar{X}$
E <sub>1</sub> (TO), E <sub>1</sub> (LO)	X(Y, Z) Y
E <sub>2</sub>	X(Y, Y) Z
E <sub>2</sub>	Z(Y, X) $\bar{Z}$
A <sub>1</sub> (LO), E <sub>2</sub>	Z(Y, Y) $\bar{Z}$

where  $\omega_{LO}$  and  $\omega_{TO}$  represent the LO and TO phonon frequencies, and  $\epsilon(\omega)$  and  $\epsilon(\infty)$  represent the low and high (optical) frequency dielectric constants, respectively. When  $\omega = \omega_{LO}$ , the dielectric function vanishes,  $\epsilon(\omega_{LO}) = 0$ . Equation 1.27 can be expanded to the directional dependence of the dielectric function in wurtzite ZnO. In the direction parallel to the *c*-axis or the *z*-direction, from the  $\Gamma$  point to the A point, in the *k*-space (with *x*, *y* representing the in-plane coordinates), the low- and high-frequency dielectric functions are related to each other with the help of A<sub>1</sub>(LO) and E<sub>1</sub>(TO) phonon frequencies through [119]

$$\epsilon_{//}(\omega) = \epsilon_{//}^{\infty} \frac{\omega^2 - \omega_{//}^2(LO)}{\omega^2 - \omega_{//}^2(TO)} \tag{1.28}$$

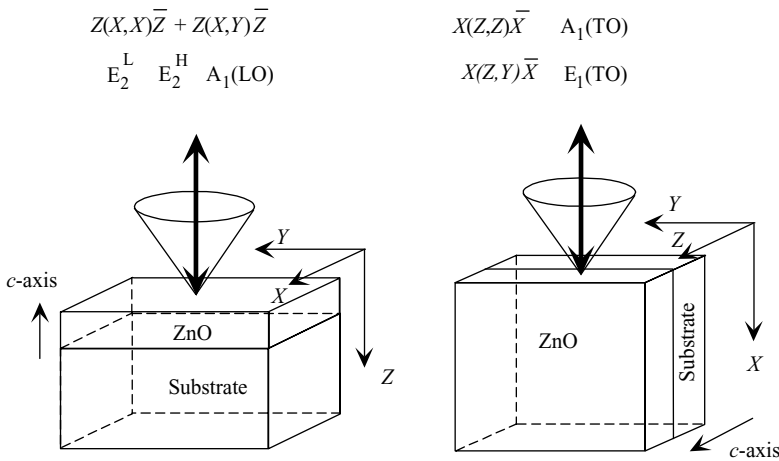
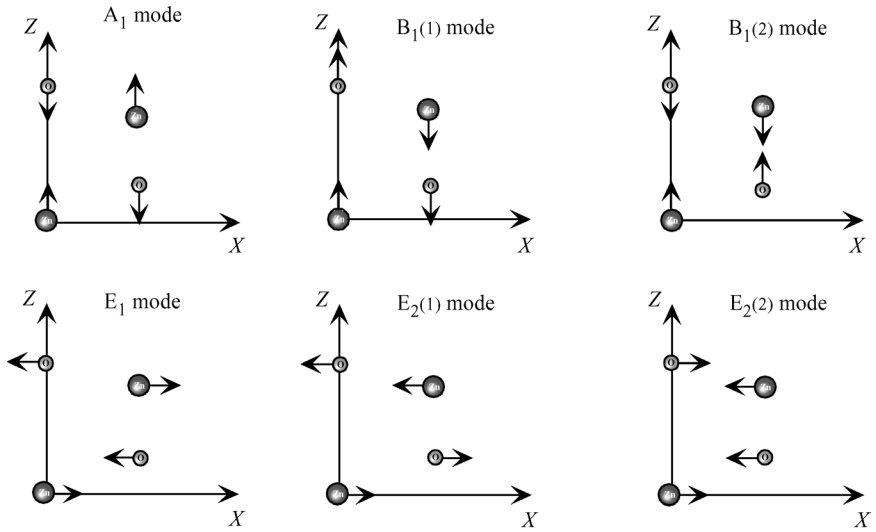
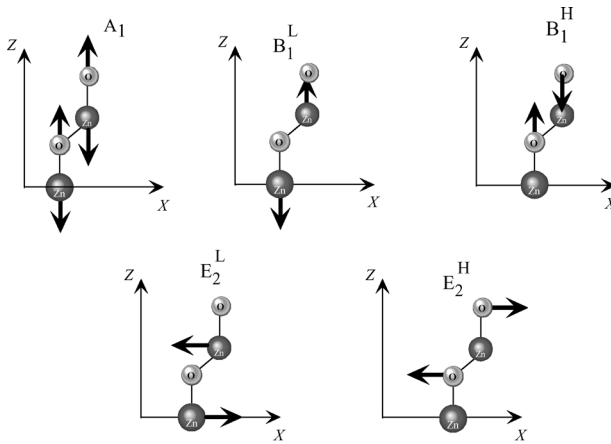


**Figure 1.19** Schematic representation of two Raman configurations with incident and scattered light directions in the backscattering geometry for  $Z(X, X) \bar{Z} + Z(X, Y) \bar{Z}$  configuration to sense  $E_2^L$ ,  $E_2^H$ , and  $A_1(LO)$  modes,  $X(Z, Z) \bar{X}$  configuration to sense  $A_1(TO)$  mode, and  $X(Z, Y) \bar{X}$  configuration to sense  $E_1(TO)$  mode.



(a)



(b)

**Figure 1.20** Atomic vibrations in Wz ZnO. The larger atom represents Zn while the smaller one represents O.  $X = (100)$ ,  $Y = (010)$ ,  $Z = (001)$  represent the optical polarization directions: (a) for general wave vector and (b) for zone center phonons.

**Table 1.9** Phonon mode frequencies (in units of  $\text{cm}^{-1}$ ) of wurtzite ZnO at the center of the Brillouin zone obtained from infrared spectroscopic ellipsometry (IRSE) and Raman scattering measurements in comparison with theoretical predictions.

Symmetry	Raman spectroscopy	Infrared spectroscopy	Theoretical calculations
A <sub>1</sub> -TO	380 (2) <sup>a</sup> , 379 (2) <sup>b</sup> , 380 <sup>c</sup> , 380 <sup>d</sup> , 378 <sup>e</sup> , 380 <sup>f</sup>	380 <sup>g</sup> , 376.5 <sup>j</sup>	382 <sup>h</sup> , 386 <sup>i</sup>
E <sub>1</sub> -TO	409 (2) <sup>a</sup> , 410 (2) <sup>b</sup> , 407 <sup>c</sup> , 413 <sup>d</sup> , 409.5 <sup>e</sup>	409.1 (0.9) <sup>a</sup> , 408.2 (0.3) <sup>b</sup> , 412 <sup>g</sup> , 410.7 <sup>j</sup>	316 <sup>h</sup> , 407 <sup>i</sup>
A <sub>1</sub> -LO	574 <sup>c</sup> , 576 <sup>e</sup> , 579 <sup>d</sup> , 579 <sup>f</sup>	574.5 (0.3) <sup>a</sup> , 577.1 (0.4) <sup>b</sup> , 570 <sup>g</sup> , 574.1 <sup>j</sup>	548 <sup>h</sup>
E <sub>1</sub> -LO	587 (2) <sup>a</sup> , 591 (2) <sup>b</sup> , 583 <sup>c</sup> , 588 <sup>e</sup> , 591 <sup>d</sup>	588.3 (0.7) <sup>a</sup> , 592.1 (0.2) <sup>b</sup> , 591 <sup>g</sup> , 590.4 <sup>j</sup>	628 <sup>h</sup>
E <sub>2</sub> -low	102 (1) <sup>a</sup> , 102 (1) <sup>b</sup> , 101 <sup>c</sup> , 101 <sup>d</sup> , 98 <sup>e</sup> , 99 <sup>f</sup>		126 <sup>h</sup> , 98 <sup>i</sup>
E <sub>2</sub> -high	438 (1) <sup>a</sup> , 437 (1) <sup>b</sup> , 437 <sup>c</sup> , 444 <sup>d</sup> , 437.5 <sup>e</sup> , 438 <sup>f</sup>		335 <sup>h</sup> , 433 <sup>i</sup>
B <sub>1</sub> -low			261 <sup>k</sup>
B <sub>1</sub> -high			552 <sup>k</sup>

<sup>a</sup>ZnO epilayer grown on sapphire. Error bars in parentheses of the infrared spectroscopy data represent the 90% confidence limits. Error bars of the Raman data are determined by the experimental setup [123].

<sup>b</sup>Bulk ZnO. Error bars in parentheses represent the 90% confidence limits [123].

<sup>c</sup>Raman scattering on ZnO single crystal [105].

<sup>d</sup>Raman spectra on ZnO [106].

<sup>e</sup>Raman spectra [121].

<sup>f</sup>Raman spectra on ZnO film [115].

<sup>g</sup>IR reflection [116].

<sup>h</sup>Atomistic calculations based on an interatomic pair potential within the shell model approach [19].

<sup>i</sup>Calculation [109].

<sup>j</sup>Generalized IRSE on *a*-plane ZnO on *r*-plane sapphire [117].

<sup>k</sup>*Ab initio* calculations [118].

Likewise, Equation 1.27 can be expanded in the direction perpendicular to the *c*-axis or the *z*-direction, or in the basal plane or the (*x*, *y*) plane (in *k*-space between the  $\Gamma$  point and *M* (1/2, 0, 0) or *K* (1/3, 1/3, 0) points). In this case, the low- and high-frequency dielectric functions are related to each other with the help of A<sub>1</sub>(TO) and E<sub>1</sub>(LO) phonons through [119]

$$\epsilon_{\perp}(\omega) = \epsilon_{\perp}^{\infty} \frac{\omega^2 - \omega_{\perp}^2(\text{LO})}{\omega^2 - \omega_{\perp}^2(\text{TO})}, \quad (1.29)$$

where  $\perp$  and  $\parallel$  indicate in the basal plane and along the *c*-direction, respectively.

For wurtzite materials, the various directional components of phonon modes correspond to  $\omega_{\perp}(\text{LO}) \rightarrow E_1(\text{LO})$ ,  $\omega_z(\text{LO}) = \omega_{\parallel}(\text{LO}) \rightarrow A_1(\text{LO})$ ,  $\omega_{\perp}(\text{TO}) \rightarrow E_1(\text{TO})$ , and  $\omega_z(\text{TO}) = \omega_{\parallel}(\text{TO}) \rightarrow A_1(\text{TO})$ . In the *z*-direction (along the *c*-direction) and the directions perpendicular to the *z*-direction (in basal plane), LO and TO phonons are not mixed. For any direction other than these in-plane and out-of-plane

configurations, the LO and TO phonons mix and hybridize. For a given propagation direction with an angle  $\theta$  relative to the  $c$ -axis ( $z$ -axis), one finds three phonon branches. One is an ordinary TO phonon mode with atomic displacement in the  $xy$  plane. The other two branches have a mixed TO and LO character and their dielectric functions are given by the solutions of [120]

$$\varepsilon_{//} \cos^2 \theta + \varepsilon_{\perp} \sin^2 \theta = 0. \quad (1.30)$$

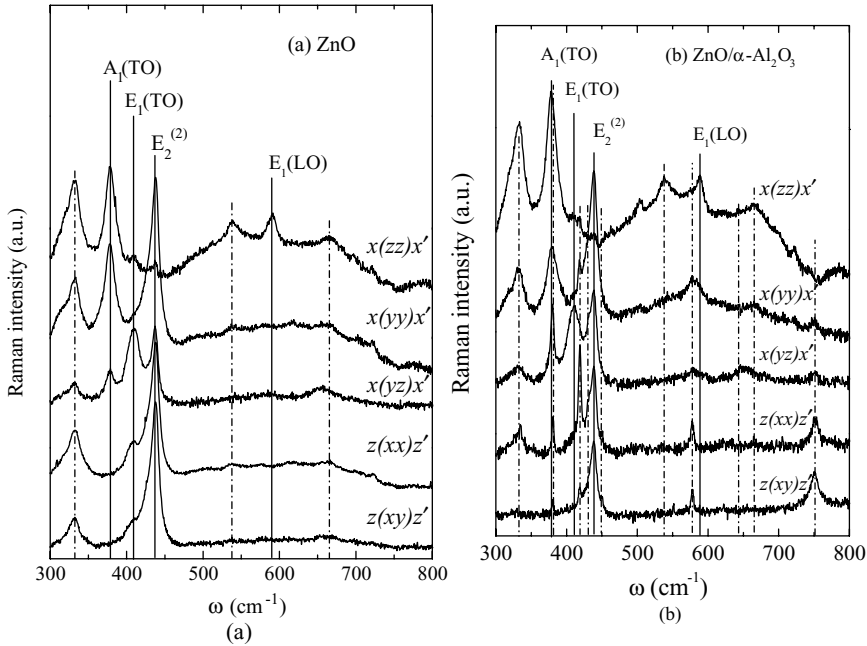
Using the above relationship, the phonon energy as a function of the angle can easily be calculated. Doing so leads to the conclusion that the upper branch (LO-like) remains between the  $A_1(\text{LO})$  and  $E_1(\text{LO})$  energies while the lower branch (TO-like) remains between the  $A_1(\text{TO})$  and  $E_1(\text{TO})$  energies. Therefore, the dispersion remains small compared to the LO–TO separation, owing to the relatively small cell asymmetry and the large ionicity of atomic bonds. A more important consequence of LO–TO mixing is that the TO-like mode couples to carriers whereas in the  $c$ -direction  $A_1(\text{LO})$  mode and in the basal plane  $E_1(\text{LO})$  phonons couple to the carriers.

For the special case  $\omega = 0$  (or very small frequencies compared to the LO and TO phonon frequencies), the relationship between the optical and static dielectric constants reduces to the well-known Lyddane–Sach–Teller relationship

$$\frac{\varepsilon(\omega)}{\varepsilon(\infty)} = \frac{\omega_{\text{LO}}^2}{\omega_{\text{TO}}^2}, \quad (1.31)$$

which is often used to determine the optical frequency dielectric constant from knowledge of the  $A_1(\text{LO})$  and  $A_1(\text{TO})$  phonon frequencies along the  $c$ -direction and  $E_1(\text{LO})$  and  $E_1(\text{TO})$  in the basal plane. The static and high-frequency dielectric constants of ZnO are listed in Table 3.8.

A reasonably complete set of phonon mode frequencies has been measured by using either IR or Raman spectroscopy (RS) for both bulk and thin-film ZnO. In early measurements, phonon modes of bulk ZnO were explored and discussed extensively by several groups using RS measurements [105–108, 121]. Observation of the phonon modes in PLD-grown ZnO thin films was reported by Lu *et al.* [122] and Ashkenov *et al.* [117, 123]. No significant differences for the  $E_1(\text{TO})$ ,  $A_1(\text{TO})$ , and  $E_2$  mode frequencies were observed between the thin film and the bulk sample. The thin-film ZnO phonon mode frequencies are highly consistent with those of the bulk material. A small redshift of the longitudinal optical phonon mode frequencies of the ZnO films with respect to the bulk material was tentatively assigned to the existence of vacancy point defects within the films. The data obtained from IR and RS measurements are consistent with each other within the experimental accuracy. The predicted phonon frequencies reported by Tsuboi and Wada [109] are also in very good agreement with the experimental observations. The modes  $E_1(\text{TO})$  and  $A_1(\text{TO})$  reflect the strength of the polar lattice bonds. Accordingly, as discussed above no significant differences between the lattice constants of the film and bulk samples were observed.



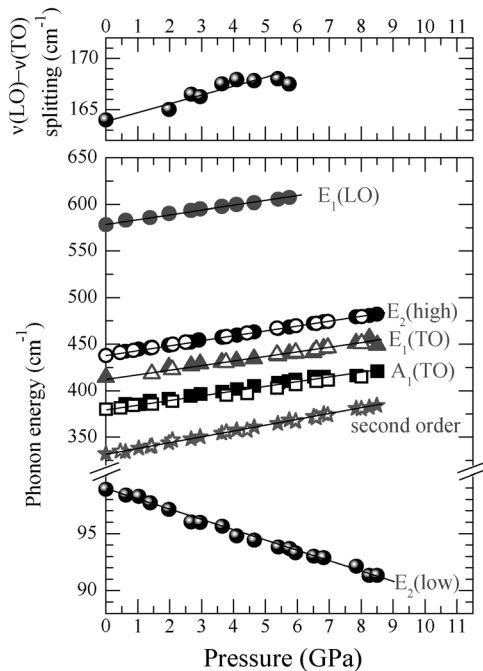
**Figure 1.21** (a) Raman spectra of the bulk ZnO sample. First-order phonon modes of ZnO are indicated by the vertical solid lines. The vertical dashed–dotted lines mark the features due to multiple-phonon scattering processes. (b) Raman spectra for the thin-film ZnO sample. The vertical dotted lines indicate the Raman-active sapphire substrate phonon mode frequencies. (Courtesy of M. Schubert [123].)

Figure 1.21 shows typical Raman spectra of the bulk and thin-film ZnO samples [123]. In this particular study, solid lines in both figures indicate  $E_1$ ,  $A_1$ , and  $E_2$  phonon modes of ZnO. Dashed–dotted lines mark features observed at 332, 541, and 665  $\text{cm}^{-1}$ , which were assigned to possible multiple-phonon scattering processes [105, 108]. Dotted lines are related to the sapphire phonon mode frequencies ( $A_{1g}$  mode: 417 and 645  $\text{cm}^{-1}$ ;  $E_g$  mode: 379, 430, 450, 578, and 751  $\text{cm}^{-1}$ ) [110]. For both samples  $A_1(\text{LO})$  has not been observed and it was claimed that the scattering cross section for this mode is markedly smaller than that of the  $A_1(\text{TO})$  mode due to the destructive interference between the Fröhlich interaction and the deformation potential contributions to the LO phonon scattering in ZnO [107]. Additionally, the occurrence of the  $E_1(\text{LO})$  mode in both samples was attributed to the breakdown of the selection rule due to the use of the Raman microscope.

Rajalakshmi *et al.* [124] have reported additional Raman peaks at 205, 331, and 539  $\text{cm}^{-1}$  in their ZnO nanoparticle samples synthesized at ambient temperature using an electrochemical cell. Similar peaks (208, 332, and 541  $\text{cm}^{-1}$ ) that occur under resonance conditions were also reported for bulk ZnO [108]. In both studies, these peaks have been assigned to the second-order Raman spectrum arising from

zone boundary ( $M$  point) phonons  $2\text{-TA}(M)$ ,  $2\text{-E}_2(M)$ , and  $2\text{-LA}(M)$ , respectively. However, the coupling to plasmons in highly doped material and stress-induced effects due to lattice mismatch with the substrate might play a role in the interpretation of the observed phonon frequencies.

The hydrostatic pressure dependence of the zone center phonon modes has also been studied. In conjunction with the previously reported results [111, 125], Decremps *et al.* [92] investigated in detail the pressure-induced Raman shifts in a single-crystal ZnO sample at room temperature using Raman spectroscopy and *ab initio* calculations based on a plane-wave pseudopotential method within the density functional theory. The pressure dependence of the zone center phonons ( $E_2$ ,  $A_1$ , and  $E_1$ ) was measured for the wurtzite structure up to the hexagonal/cubic phase transition pressure ( $\sim 8.7$  GPa), above which all Raman peaks disappeared. The pressure dependences of the phonon frequencies for the two high-pressure experiments are shown in Figure 1.22. Only the  $E_2$ -low mode exhibited a negative pressure dependence. The frequency shifts in the  $E_2$ -high,  $A_1(\text{TO})$ ,  $E_1(\text{TO})$ , and  $E_1(\text{LO})$  modes were observed to increase with pressure. The pressure dependence of the optical mode energies was also compared with the prediction of a model. No evidence of an anomaly in the  $E_2$  and  $A_1$  mode behaviors before the phase transition



**Figure 1.22** *Top:*  $(\nu_{\text{LO}} - \nu_{\text{TO}})$   $E_1$  phonon mode splitting versus pressure. Solid lines are linear least-square fits to the experimental points. *Bottom:* Pressure dependence of the observed optical phonons. Open (full) symbols: propagation of light perpendicular (parallel) to  $c$ -axis. (Courtesy of F. Decremps [92].)

was detected. The corresponding perpendicular tensor component of the Born's transverse dynamic charge  $e_T^*$  ( $Z^*$  in table 1.6) is experimentally found to increase under compression as  $e_T^*(P) = 2.02 - 6.4 \times 10^{-3} P$ , whereas calculations give  $e_T^*(P) = 2.09 - 2.5 \times 10^{-3} P$  (in units of the elementary charge  $e$ ,  $P$  in GPa). It has also been noted that the observation of optical phonons under pressure does not show any softening of the optic  $A_1$  and  $E_2$ -high modes as theoretically expected [126, 127]. Moreover, from both the experimental observation and the theoretical calculations, the LO–TO splitting of the  $E_1$  phonon mode, which depends on the long-range electrostatic forces, has unusually shown weak pressure dependence. This behavior has been attributed to a small variation of the chemical bond ionicity of wurtzite ZnO with pressure. Experimentally, the second-order process observation (e.g., via optical phonon instabilities) could not be performed because the wurtzite-to-rocksalt first-order transition limits the pressure range within which the *wurtzite* structure exists.

The strong bond in ZnO and light O atoms result in high phonon frequencies and limit the range of possibly observable impurity-related local vibrational modes (LVMS) to even lighter elements at higher frequencies. So far, a number of reports have appeared for the infrared and Raman modes, which have been associated with local vibrational modes of impurities, dopants, and defect complexes. Kaschner *et al.* [128] have studied the influence of nitrogen, which is considered as a potential acceptor in ZnO, on the lattice dynamics of ZnO. They investigated a series of samples grown by chemical vapor deposition (CVD) containing different nitrogen concentrations. The Raman spectra revealed vibrational modes at 275, 510, 582, 643, and  $856 \text{ cm}^{-1}$  in addition to the host phonons of ZnO as discussed above. It has been observed that the intensity of these additional modes correlates linearly with the nitrogen concentration. Therefore, these modes were interpreted as local vibrational modes due to the vibrating nitrogen-related complexes. Bundesmann *et al.* [129] later measured the phonon modes of Fe-, Sb-, Al-, Ga-, and Li-doped ZnO thin films, grown by pulsed laser deposition (PLD) on *c*-plane sapphire substrates using polarized micro-Raman spectroscopy. Additional modes at about 277, 511, 583, and  $644 \text{ cm}^{-1}$ , which had been assigned to N incorporation, were observed for intentionally doped Fe, Sb, and Al films [129]. The mode at  $277 \text{ cm}^{-1}$  was also observed for Ga-doped films. Based on these observations, it has been stated that these modes cannot be related directly to N incorporation. Instead, the host lattice defects were suggested to be the origin of the additional modes [129]. This suggestion was supported by theoretical considerations, which stated that defects related to the incorporation of dopants might result in breakdown of the selection rules, and silent modes become Raman active [130]. Therefore, the above-addressed additional modes can be related to silent modes of ZnO.

First-principles calculations based on density functional theory within the local density approximation and the pseudopotential plane-wave method by Van de Walle [131] suggest that hydrogen atoms might act as shallow donors in ZnO. It has been argued that the incorporation of hydrogen accompanied by remarkably large relaxations of the surrounding atoms leads to an O–H bond, which in fact can be regarded as a new type of dopant atom in ZnO. To determine the microscopic

structure of hydrogen donors, the LVMS arising from these complexes have been investigated using IR and Raman spectroscopy [132–134]. The hydrogen-related defects in ZnO samples, hydrogenated using an H or a D plasma, have been investigated by a combination of local vibrational mode spectroscopy and compared with the first-principles calculations. Three new IR absorption lines at 3611.3, 3349.6, and 3312.2  $\text{cm}^{-1}$  have been observed at 10 K. Based on polarization studies and first-principles calculations, the line at 3611.3  $\text{cm}^{-1}$  was assigned to a single interstitial hydrogen atom at the bond center site oriented along the  $c$ -axis of the crystal although the possibility that this H atom is associated with an impurity cannot be ruled out. The lines at 3349.6 and 3312.2  $\text{cm}^{-1}$  were attributed to a zinc vacancy that contains two inequivalent hydrogen atoms, one in an O–H bond roughly aligned with the  $c$ -axis and the other in an O–H bond that forms an angle of  $100^\circ$  with the  $c$ -axis [133].

McCluskey *et al.* [132] have also used IR spectroscopy to measure local vibrational modes in ZnO annealed in hydrogen gas. An IR absorption peak at 3326.3  $\text{cm}^{-1}$  was observed at a temperature of 8 K and attributed to the O–H stretch mode based on comparison with the first-principles calculations of Van de Walle [131], in which the calculated mode frequencies were 3726 and 3384  $\text{cm}^{-1}$  for the bond-centered and antibonding configurations, respectively, after subtracting 166  $\text{cm}^{-1}$  due to the anharmonic terms in the potential causing the stretch-mode frequency to shift downward. However, because of the uncertainty in actual anharmonicity the bond-centered configuration was not ruled out. The IR spectrum of ZnO annealed in deuterium has revealed an additional stretch mode at 2470.3  $\text{cm}^{-1}$  for the same temperature, which was tentatively assigned to the oxygen–deuterium (O–D) complexes. Using polarization measurements at room temperature, they also showed that the dipole of the O–H complex does not lie parallel to the  $c$ -axis of wurtzite ZnO [132, 135].

Using Raman backscattering spectroscopy, Nickel and Fleischer [136] have detected six local vibrational modes at 2854, 2890, 2918, 2948, 2988, and 3096  $\text{cm}^{-1}$ . A Raman backscattering spectrum measured on an *as-grown* ZnO single crystal is shown in Figure 1.23. The peak positions were obtained by deconvolving the spectrum into six Gaussian lines. To elucidate the origin of the local vibrational modes, Nickel and Fleischer performed hydrogen effusion experiments on ZnO single crystals. Upon annealing some samples up to 950  $^\circ\text{C}$  to remove hydrogen, the subsequent measurement revealed that the local vibrational modes disappeared, from which the observed vibrational modes were attributed to the presence of hydrogen in the ZnO crystals. It was found that the stretching vibration of the corresponding hydrogen complex is *not* parallel to the  $c$ -axis. The vibrational modes located at 2854, 2890, 2918, 2948, and 2988  $\text{cm}^{-1}$  were assumed to be due to the stretching modes of C–H, symmetric stretching modes of C–H<sub>3</sub>, symmetric stretching modes of C–H<sub>2</sub>, antisymmetric stretching modes of C–H<sub>3</sub>, and antisymmetric stretching modes of C–H<sub>2</sub>, respectively, based on the effusion data, where a significant concentration of hydrocarbons was detected. The local vibrational mode located at 3096  $\text{cm}^{-1}$  was attributed to the N–H, assuming a considerable amount of hydrogen is bonded to nitrogen atoms based on the effusion experimental data. This

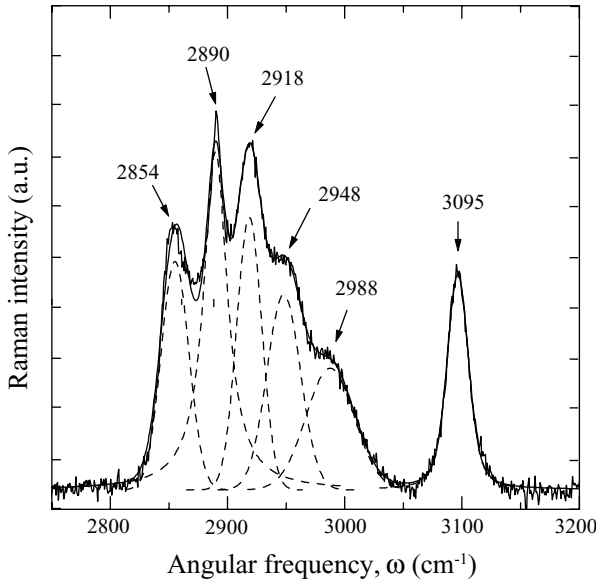


**Figure 1.23** Raman backscattering spectrum of *as-grown* single-crystal ZnO after background subtraction. The sample was irradiated with the 488 nm line of an Ar laser and a power of 190 mW. The solid line represents a least-square fit of six Gaussian lines to the data. The dashed lines indicate the individual local vibrational modes. The peak positions are indicated in the plot. (Courtesy of N.H. Nickel [136].)

observed mode frequency was also found to be consistent with that reported for ZnSe compound semiconductors [137].

## 1.6 Thermal Properties

As in all solids, the atoms in a semiconductor at nonzero temperature are in ceaseless motion, oscillating about their equilibrium states. These oscillation modes are defined by phonons as discussed in Section 1.5. The amplitude of the vibrations increases with temperature, and the thermal properties of the semiconductor determine the response of the material to temperature changes. Thermal expansion, specific heat, and pyroelectricity are among the standard material properties that define the linear relationships between mechanical, electrical, and thermal variables. These thermal properties and thermal conductivity depend on the ambient temperature, and the ultimate temperature limit to study these effects is the melting temperature, which is  $\sim 1975$  K for ZnO. It should also be noted that because ZnO is widely used in thin-film form deposited on foreign substrates, meaning templates other than ZnO, the properties of the ZnO films also intricately depend on the inherent properties of the substrates, such as lattice constants and thermal expansion coefficients.

## 1.6.1

**Thermal Expansion Coefficients**

The lattice parameters of semiconductors depend on temperature and are quantified by thermal expansion coefficients, which are denoted as  $\Delta a/a$  or  $\alpha_a$  and  $\Delta c/c$  or  $\alpha_c$ , for in-plane and out-of-plane cases, respectively. They depend on the stoichiometry, presence of extended defects, and free carrier concentration. The typical room-temperature values for ZnO are  $\Delta a/a = 4.75 \times 10^{-6} \text{ K}^{-1}$  and  $\Delta c/c = 2.9 \times 10^{-6} \text{ K}^{-1}$  [138]. Figure 1.24 depicts the percent thermal expansion of ZnO in the  $c$ -plane and along the  $c$ -axis as a function of temperature [139]. Also shown is the thermal expansion of polycrystalline ZnO.

The temperature dependence of the lattice constants  $a$  and  $c$  and the thermal expansion coefficients of hexagonal ZnO have been determined by the capacitive method [138]. The thermal expansion coefficients measured between 4 and 800 K are shown in Figure 1.25. Reeber [30] has employed X-ray powder diffraction methods instead to measure the temperature dependence of the lattice parameters of ZnO in the range of 4.2–296 K. The results are shown in Figure 1.26. When analyzing the dependence of the lattice parameters on temperature, fourth-order polynomials

$$a(T) = 3.24853 - 1.0811 \times 10^{-5}T + 6.820 \times 10^{-8}T^2 - 6.109 \times 10^{-11}T^3 + 2.143 \times 10^{-14}T^4 \quad (1.32)$$

were fitted by using the least-square method, which gives a minimum for the  $a_0$  parameter at 93 K. The  $c_0$  parameter did not give any minimum, most probably due to its low precision and uncertainty in the measurement. Using the same X-ray diffraction technique from 300 to 1373 K for powdered ZnO crystals, Iwanaga *et al.* [140] obtained second-order polynomials for the temperature dependence of

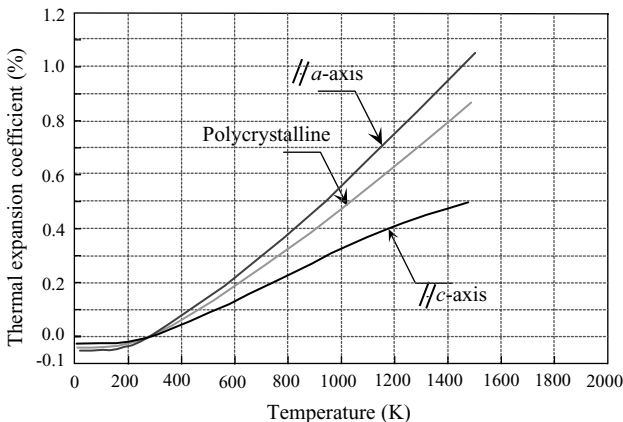


**Figure 1.24** Thermal expansion of ZnO in the  $c$ -plane (along the  $a$ -axis) and along the  $c$ -axis as a function of temperature. Also shown is the thermal expansion coefficient of polycrystalline ZnO. (After Ref. [139].)

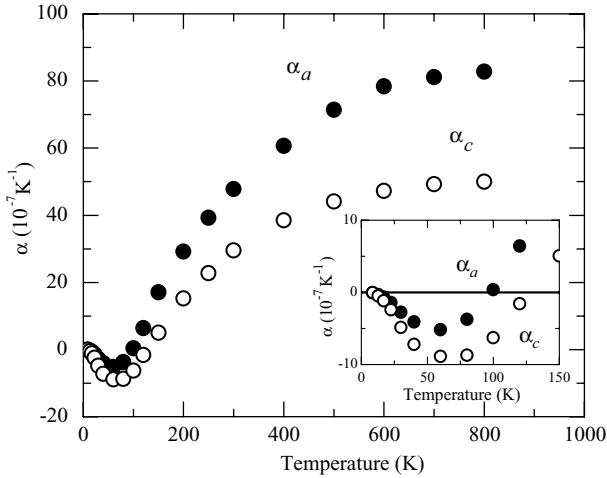


**Figure 1.25** Thermal expansion coefficients  $\alpha_a$  ( $\perp c$ ) and  $\alpha_c$  ( $\parallel c$ ) of ZnO as a function of temperature. (After Ref. [138].)

the lattice parameters measured within an error of  $5 \times 10^{-4} \text{ \AA}$ :

$$\begin{aligned} a(T) &= 3.2468 + 0.623 \times 10^{-5}T + 12.94 \times 10^{-9}T^2, \\ c(T) &= 5.2042 + 0.522 \times 10^{-5}T + 12.13 \times 10^{-9}T^2, \end{aligned} \quad (1.33)$$

with corresponding thermal expansion coefficients of  $\alpha_a = 4.31 \times 10^{-6} \text{ K}^{-1}$  and  $\alpha_c = 2.49 \times 10^{-6} \text{ K}^{-1}$  at 300 K.

Hang and Jou [141] studied thermal properties of ZnO films prepared by RF magnetron sputtering on Si and GaAs substrates. Thermal stresses were determined by using bending beam technique where the specimens were thermally cycled from 25 to 400 °C. They investigated the thermal expansion coefficient as a function of growth parameters, such as substrate temperature and sputtering power. With a

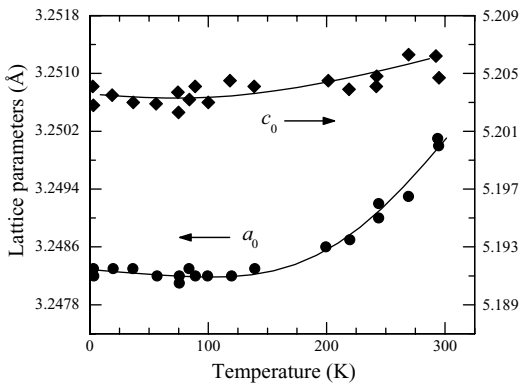


**Figure 1.26** Wurtzite ZnO lattice parameters as a function of temperature. (After Ref. [30].)

few exceptions, they found no significant changes with the variation of total gas pressure from 0.53 to 2.1 Pa, substrate temperature from 250 to 450 °C, Ar-to-O pressure ratio from 0.3 to 3, and power from 100 to 300 W. It has been observed that the thermal expansion coefficient increases about 37% from  $5 \times 10^{-6}$  to  $8 \times 10^{-6} \text{ } ^\circ\text{C}^{-1}$  within the temperature range of 25–400 °C. Aoumeur *et al.* [100] calculated the thermal expansion coefficient for both zinc blende and rocksalt phases of ZnO using a molecular dynamics simulation based on Tersoff's potential. They found that  $\alpha = 1.24 \times 10^{-5} \text{ K}^{-1}$  for the zinc blende and  $\alpha = 0.16 \times 10^{-5} \text{ K}^{-1}$  for rocksalt structures.

As alluded to earlier, ZnO is widely used in thin-film form deposited on nonnative substrates. Therefore, the material quality, actually properties in general, of the ZnO films depends on the properties of the substrates used. Especially, the lattice parameters and thermal expansion coefficients of these substrates are extremely important since reduction of strain and dislocation density in ZnO thin films is the main objective, and substrates with parameters similar to those of ZnO are favorable in this context. Thermal expansion coefficients of various substrates used for thin-film ZnO growth are given in Table 2.3.

### 1.6.2

#### Thermal Conductivity

Thermal conductivity ( $\kappa$ ), a kinetic property determined by the contributions from the vibrational, rotational, and electronic degrees of freedom, is an extremely important material property when high-power/high-temperature electronic and optoelectronic devices are considered. For pure crystals, phonon–phonon scattering, which is ideally proportional to  $T^{-1}$  above the Debye temperature, is the limiting process for thermal conductivity. Specifically, the heat transport is predominantly determined by the phonon–phonon Umklapp scattering and phonon scattering by point and extended defects, such as vacancies (inclusive of lattice distortions caused by them), impurities, and isotope fluctuations (mass fluctuation). As for other semiconductors point defects play a significant role in thermal conductivity of ZnO. The lattice contribution (phonon scattering) to the thermal conductivity  $\kappa$  is obtained from the kinetic theory as [142]

$$\kappa_{\text{lattice}}(T) = \frac{1}{3} v_s C_{\text{lattice}}(T) L(T), \quad (1.34)$$

where  $T$  is the temperature,  $v_s$  is the velocity of sound (almost independent of temperature),  $C_{\text{lattice}}(T)$  is the lattice specific heat, and  $L(T)$  is the phonon mean free path. In almost all materials,  $\kappa(T)$  first increases with temperature, reaches a maximum ( $\kappa_{\text{max}}$ ) at some characteristic temperature  $T_{\text{ch}}$ , and then decreases. At low temperatures,  $L$  is relatively long and is dominated by extrinsic effects such as “defects” and/or finite crystal size and  $C_{\text{lattice}}(T) \sim (T/\theta_D)^3$ , where  $\theta_D$  is the Debye temperature. As the temperature increases,  $C_{\text{lattice}}(T)$  begins to saturate and intrinsic temperature-dependent Umklapp processes become dominant, thus causing a decrease in  $L$ .

The electronic contribution to the thermal conductivity, which is negligible for carrier concentrations  $\leq 10^{19} \text{ cm}^{-3}$ , is [143]

$$\kappa_{\text{electr}}(T) = \frac{\pi^2 n k_B^2 T \tau_{\text{electr}}}{3 m_c^*}, \quad (1.35)$$

where  $n$  is the carrier density,  $k_B$  is the Boltzmann constant,  $\tau_{\text{electr}}$  is the scattering time of the electrons, and  $m_c^*$  is the conduction band effective mass. The overall thermal conductivity generally decreases with increasing carrier concentration, because the decrease in the lattice component of  $\kappa$  due to increased phonon scattering from both impurities and free electrons outweighs the increase in the electronic contribution to  $\kappa$  [144].

Scanning thermal microscopy (SThM) [145] is a powerful technique used to measure thermal conductivity and is purported to provide nondestructive, absolute measurements with a high spatial/depth resolution of about 2–3  $\mu\text{m}$ . Thermal imaging is achieved by using a resistive thermal element incorporated at the end of a cantilever/AFM tip, which forms one element of a Wheatstone bridge (for more information and a schematic see Ref. [91]). Upon contact with the sample, the tip tends to cool down due to heat conduction into the sample, which is related to its thermal conductivity,  $\kappa$ . The bridge circuit applies a compensating voltage ( $V_{\text{out}}$ ) to maintain its target operating temperature. The feedback signal for constant resistance is a measure of the thermal conductivity of the material with which the tip is in contact, specifically  $V_{\text{out}}^2$  is proportional to  $\kappa$ , because power dissipation is the mechanism here. Measurements of the absolute values of  $\kappa$  are based on a calibration procedure. This simply comprises calibrating the feedback signal,  $V_{\text{out}}^2$ , for a constant thermal element resistance against that for samples with known conductivities such as GaSb, GaAs, InP, Si, and Al metal. The influence of the surface roughness on the effective thermal conductivity is of concern. For a perfectly flat surface, the contact between the probe tip (radius of curvature  $\sim 1 \mu\text{m}$ ) and the sample surface is very small. However, for rough surfaces the tip could impinge on a valley- or hillock-like feature with the result that a valley/hillock will lead to increased/decreased thermal signal with a corresponding change in the measured effective thermal conductivity.

SThM was applied to measure the room-temperature thermal conductivity on Zn and O faces of high-quality ZnO (0001) single crystals, grown by a vapor-phase transport method [146]. The thermal investigation was performed in two ways: point-by-point ( $\sim 2 \mu\text{m}$  resolution) and area scans. The point-by-point measurements on Zn-face samples produced  $\kappa = 1.16 \pm 0.08$  and  $1.02 \pm 0.07 \text{ W cm}^{-1} \text{ K}^{-1}$ , while O-face samples showed  $\kappa = 1.10 \pm 0.09$  and  $0.98 \pm 0.08 \text{ W cm}^{-1} \text{ K}^{-1}$ . The variations represent the standard deviation in the data, which was obtained by investigating approximately 15–20 points randomly distributed over a  $6 \times 6 \text{ mm}^2$  surface area. In this study, a correlation between the surface topography and thermal conductivity variations was also studied by acquiring the AFM and SThM scans simultaneously during the area scan. The effects of surface roughness on effective  $\kappa$  values were treated in terms of tip–surface geometry. It has been argued that when the

experimental voltage variations (proportional to  $\kappa$ ) correspond to only 6–7% changes in the thermal conductivity, variations probably originate from the topography. Larger variations (>12%) in the SThM voltage reading for AFM topographical features with heights <100 nm would be an indication of intrinsic thermal conductivity variations across the area under investigation.

Pollak and coworkers [147] measured the thermal conductivity  $\kappa$  of several bulk ZnO (0001) samples grown by CERMET, Inc. and prepared by the authors' group under different surface treatments. The measurements were made using SThM with a spatial/depth resolution of about 2–3  $\mu\text{m}$ . The surface treatments of various samples are summarized in Table 1.10. The measurements were made at different points on each sample and the results are also shown in Table 1.10. For sample (a) in both positions,  $\kappa$  is considerably less than the previously reported values of about  $1.0 \text{ W cm}^{-1} \text{ K}^{-1}$  [146]. To be consistent with the earlier models, one would argue that forming gas annealing has resulted in surface roughness, which has considerably reduced  $\kappa$ . The same is mostly true for sample (e), which exhibits considerable inhomogeneity in the measured  $\kappa$ . At present, there is no explanation for this result, although Florescu *et al.* [144] did find that in GaN  $\kappa$  was a function of carrier concentration; that is, it decreased with increasing carrier concentration due to scattering of phonons from the ionized impurities. No information is available neither about the carrier concentrations/doping levels nor about their distribution for this or any other of the samples. For sample (b) the measured results for  $\kappa$  are similar to those reported in Ref. [146], while for samples (c) and (d) they are actually somewhat higher and are the highest  $\kappa$  values reported for ZnO. Thus, both air annealing and nitrogen plasma treatment result in a good surface.

**Table 1.10** Thermal conductivity,  $\kappa$  ( $\text{W cm}^{-1} \text{ K}^{-1}$ ), at multiple positions of bulk ZnO samples with various surface treatments [147].

Sample	Surface treatment	Thermal conductivity ( $\text{W cm}^{-1} \text{ K}^{-1}$ )
(a)	Forming gas annealed	(1) $\kappa = 0.67 \pm 0.08$
		(2) $\kappa = 0.46 \pm 0.05$
(b)	As received (O face)	(1) $\kappa = 1.00 \pm 0.08$
		(2) $\kappa = 0.95 \pm 0.06$
(c)	Air annealed	(1) $\kappa = 1.35 \pm 0.08$
		(2) $\kappa = 1.25 \pm 0.05$
(d)	Nitrogen plasma treated at 750 °C	(1) $\kappa = 1.44 \pm 0.08$
		(2) $\kappa = 1.47 \pm 0.08$
(e)	Oxygen plasma treated at 700 °C	(1) $\kappa = 0.87 \pm 0.06$
		(2) $\kappa = 0.75 \pm 0.06$
		(3) $\kappa = 0.80 \pm 0.06$
		(4) $\kappa = 1.24 \pm 0.05$
		(5) $\kappa = 0.54 \pm 0.07$

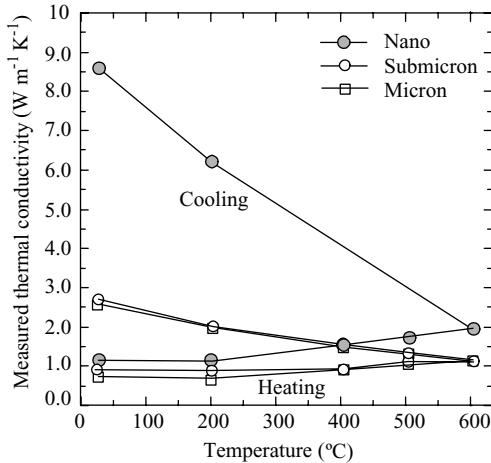


**Figure 1.27** Thermal conductivity of nanometer-, submicrometer-, and micrometer-sized ZnO heated from room temperature to 600 °C at 3 °C min<sup>-1</sup>. (After Ref. [148].)

Olorunyolemi *et al.* [148] measured the thermal conductivity of ZnO powders with different particle sizes (micrometer, submicrometer, and nanometer) from the as-received powder state to fully sintered state by using a laser flash technique. Curves of thermal conductivity versus temperature for the three sets of ZnO samples (micrometer, submicrometer, and nanometer) measured as they were heated to 600 °C and cooled back to 25 °C are shown in Figure 1.27. The first surprising observation is that the thermal conductivity at room temperature and up to 200 °C is the reverse of what is expected for the different particle sizes, with the nanopowder having the highest thermal conductivity. The room-temperature thermal conductivities were measured to be 0.745, 0.914, and 1.160 W m<sup>-1</sup> K<sup>-1</sup> for micro-, submicron-, and nanosized samples with an average particle diameter of 1.0 μm, 0.2 μm, and 20 nm, respectively. The initial higher thermal conductivity of the nanopowder ZnO samples was attributed to the adsorbed water including chemisorbed water (more than that adsorbed by the submicrometer, which in turn is more than that adsorbed by the micrometer powder). Above 400 °C, the thermal conductivity of the nanosized particle increases faster with increasing temperature than that of the submicrometer- and the micrometer-sized samples. In this work, a model for interparticle neck growth was also developed based on the mass transfer of a powder to the neck region as a result of known temperature. The observed data were compared with the theoretical results obtained by the three-dimensional numerical code combined with this model.

Figure 1.28 shows the measured thermal conductivity of a fully sintered sample heated from room temperature to 1000 °C. The thermal conductivity decreases from 37 to 4 W m<sup>-1</sup> K<sup>-1</sup> as the temperature is increased from room temperature to 1000 °C. This is the thermal conductivity curve for a fully dense ZnO crystal, where

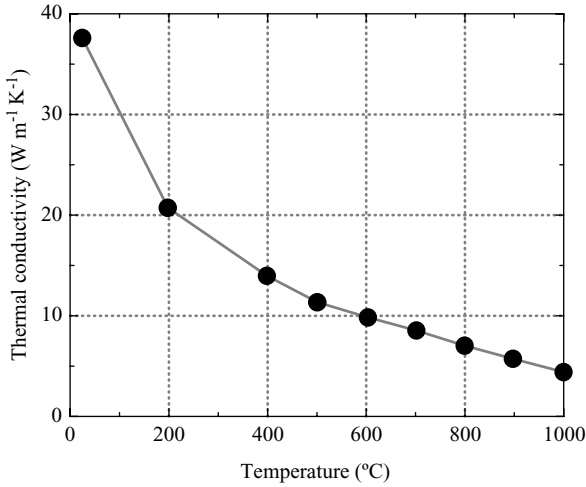


**Figure 1.28** Thermal conductivity of fully sintered ZnO heated from room temperature to 1000 °C. (After Ref. [148].)

the resistive phonon–phonon interactions (Umklapp processes) are the dominant scattering mechanisms.

The thermal properties of ZnO doped with Al and Mg were also studied by a number of groups [149–153] for the evaluation of the thermoelectric performance. Tsubota *et al.* [152] investigated the thermal conductivity of sintered  $(\text{Zn}_{1-\gamma}\text{Mg}_\gamma)_{1-x}\text{Al}_x\text{O}$  ( $x=0-0.1$ ,  $\gamma=0-0.1$ ) samples determined from thermal diffusivity and specific heat capacity measured by the laser flash technique and differential scanning calorimetry (DSC), respectively. The temperature dependences of the thermal conductivities of  $(\text{Zn}_{1-\gamma}\text{Mg}_\gamma)_{0.98}\text{Al}_{0.02}\text{O}$  ( $\gamma=0, 0.02, 0.1$ ) are shown in Figure 1.29 in comparison with that of ZnO. The reduction of  $\kappa$  from

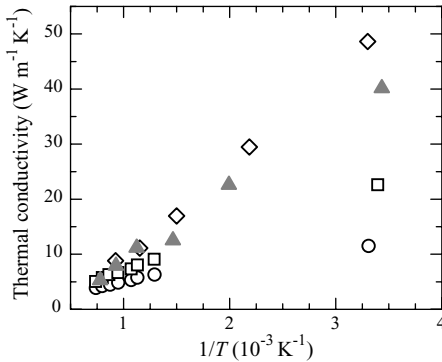


**Figure 1.29** Thermal conductivities of ZnO (diamonds),  $\text{Zn}_{0.98}\text{Al}_{0.02}\text{O}$  (triangles), and  $(\text{Zn}_{1-\gamma}\text{Mg}_\gamma)_{0.98}\text{Al}_{0.02}\text{O}$  for  $\gamma=0.02$  (squares) and 0.1 (circles) as a function of inverse temperature. (After Ref. [152].)

ZnO to  $\text{Zn}_{0.98}\text{Al}_{0.02}\text{O}$  was almost negligible. Although addition of Al (using  $\text{Al}_2\text{O}_3$ ) is considered to be ineffective in suppressing  $\kappa$  of ZnO-based materials, the difference in  $\kappa$  values between the MgO added samples and the  $\text{Zn}_{0.98}\text{Al}_{0.02}\text{O}$  sample is significantly larger at low temperatures, indicating that the addition of MgO is very effective in reducing the thermal conductivity at low temperatures. From the temperature dependence behavior ( $1/T$  dependence above the Debye temperature), the authors have concluded that the decrease in phonon-phonon scattering contribution is mainly responsible for the reduction of thermal conductivity upon the addition of MgO as well as  $\text{Al}_2\text{O}_3$ . The formation of a solid solution of MgO and ZnO is thereby considered to be effective in introducing phonon scattering centers to reduce vibrational component and thus the overall value of  $\kappa$ .

Similarly, thermal properties of  $(\text{Zn}_{1-y}\text{Mg}_y)_{1-x}\text{Al}_x\text{O}$  ( $0 < x < 0.05$  and  $0 < y < 0.16$ ) ceramics synthesized from a powder precursor prepared by a polymerized complex method have also been investigated by Katsuyama *et al.* [151]. They observed similar dependence of thermal conductivity on temperature and doping constituents as Tsubota *et al.* [152]. The thermal conductivity decreased with increasing  $x$ , but it was further suppressed by the additional substitution of the Zn sites by Mg atoms with the resultant lattice contribution, that is, the point defects introduced by the addition of Mg enhanced the phonon scattering. However, in both studies, although the temperature dependence reveals  $1/T$  behavior indicative of Umklapp scattering, room-temperature thermal conductivity of sintered ZnO, which is about  $40 \text{ W m}^{-1} \text{ K}^{-1}$  and reduces to  $\sim 7 \text{ W m}^{-1} \text{ K}^{-1}$  with increasing MgO concentration, is much smaller than the values reported for the high-quality single crystal discussed above. This indicates the large contribution due to enhanced phonon-point defect or -extended defect and -grain boundary scattering.

Because ZnO thin films deposited on foreign substrates are used in different applications, thermal conductivities of the substrates would be of concern when designing device structures. A comparison of thermal conductivities for various templates used for ZnO growth is provided in Table 2.3.

### 1.6.3

#### Specific Heat

The specific heat of a semiconductor has contributions from lattice vibrations, free carriers (very effective at low temperatures), and point and extended defects. For good quality semi-insulating crystal, the specific heat is determined mostly by the lattice vibrations. The available specific heat data for ZnO is very limited. Lawless and Gupta [154] investigated the specific heat for both pure and varistor type of ZnO samples between the temperature ranges of 1.7–25 K, where the latter has an average grain size of  $10 \mu\text{m}$ . Specific heat measurements were performed using the pulse method. As seen in Figure 1.30, the specific heat of varistor ZnO diverges from that of pure ZnO below 20 K. This difference was attributed to the

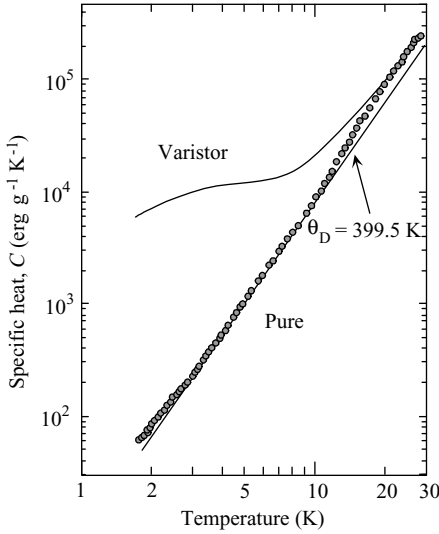


**Figure 1.30** Specific heat data measured for pure ZnO compared to data for varistor ZnO. (After Ref. [154].)

contribution by the large amount of impurities, present in the region of the grain boundaries of varistor-type ZnO, giving rise to a very large excess specific heat below 20 K.

The specific heat data for pure ZnO were further analyzed by considering two non-Debye features at different temperature regions according to

$$C = C_{\text{Debye}} + C_{\text{Schottky}} + C_{\text{Einstein}}, \quad (1.36)$$

where  $C_{\text{Debye}}$ ,  $C_{\text{Schottky}}$ , and  $C_{\text{Einstein}}$  represent the Debye, Schottky, and Einstein terms of the total specific heat of ZnO, respectively. In general, the Debye expression for the temperature dependence of specific heat in a solid at a constant pressure can be expressed as

$$C_{\text{Debye}} = 18R \left( \frac{T}{\theta_D} \right)^3 \cdot \int_0^{x_D} \frac{x^4 e^x}{(e^x - 1)^2} dx, \quad (1.37)$$

where  $x_D \equiv \theta_D/T$  and  $R = 8.3144 \text{ J mol}^{-1} \text{ K}^{-1}$  is the molar gas constant. The coefficient in front of the term  $R$  has been multiplied by 2 to take into account the two constituents making up the binary compound. By fitting the measured temperature-dependent heat capacity to the Debye expression, one can obtain the Debye temperature  $\theta_D$  specific to the heat capacity. It is often easier to extract a Debye temperature by using data either near very low temperatures or well below

the Debye temperature where the specific heat has a simple cubic dependence on temperature:

$$C_{\text{Debye}} = 234R \left( \frac{T}{\theta_D} \right)^3. \quad (1.38)$$

Unfortunately for ZnO, the samples contain large densities of free carriers and defects, which make the Debye specific heat expression unreliable. The Debye contribution to the specific heat of pure ZnO is also shown in Figure 1.30 as the curve labeled with a calorimetric Debye temperature of  $\theta_D = 399.5$  K, and the deviation of the data below  $\sim 5$  K is due to the Schottky term and that above  $\sim 10$  K is due to the Einstein term. The latter has an exponential dependence and is given by

$$C_{\text{Einstein}} = 3Rr_E \left( \frac{\theta_E}{T} \right)^2 \exp\left(-\frac{\theta_E}{T}\right) \quad \text{for } T \ll \theta_E, \quad (1.39)$$

where  $r_E$  is the number of Einstein oscillators per formula weight and  $\theta_E$  is the Einstein temperature. Schottky term has a  $T^{-2}$  dependence and is expressed by

$$C_{\text{Schottky}} = bT^{-2}, \quad (1.40)$$

where  $b = nR(\delta/2)^2$  ( $n = r_E$  is assumed) is the Schottky coefficient.

The least-square fits of these two expressions to the experimental data for the corresponding temperature ranges are shown in Figure 1.31. Very good agreement with 2–3% uncertainty was achieved for the values of  $\theta_E = 120.5$  K and  $r_E = 8.72 \times 10^{-2}$  for the case of Einstein model and  $b = 350.7 \text{ erg g}^{-1} \text{ K}^{-1}$  for the Schottky term. The Zn interstitials ( $3.6 \times 10^{21} \text{ cm}^{-3}$ ) might be responsible for the dispersionless Einstein-type contribution to the specific heat above 10 K, whereas the Schottky contribution appearing below 4 K is due to ordering of, possibly, Zn interstitials with a characteristic energy of  $\delta = 1.1 \times 10^5 \text{ eV}$  for such an ordering mechanism.

#### 1.6.4

##### Pyroelectricity

Pyroelectricity is a first-rank tensor property that relates the change in temperature to a change in electrical displacement  $\mathbf{D}$  (or polarization  $\mathbf{P}$  since no field is applied):

$$\delta D_i = \delta P_i = p_i \delta T \quad \text{or} \quad p_i = (\delta P_i / \delta T)_E. \quad (1.41)$$

The constraint for obtaining the pyroelectric coefficient  $p_i$  (units  $\text{C m}^{-2} \text{ K}^{-1}$ ) is constant electric field  $E$ . Under constant strain, that is, when the sample is rigidly

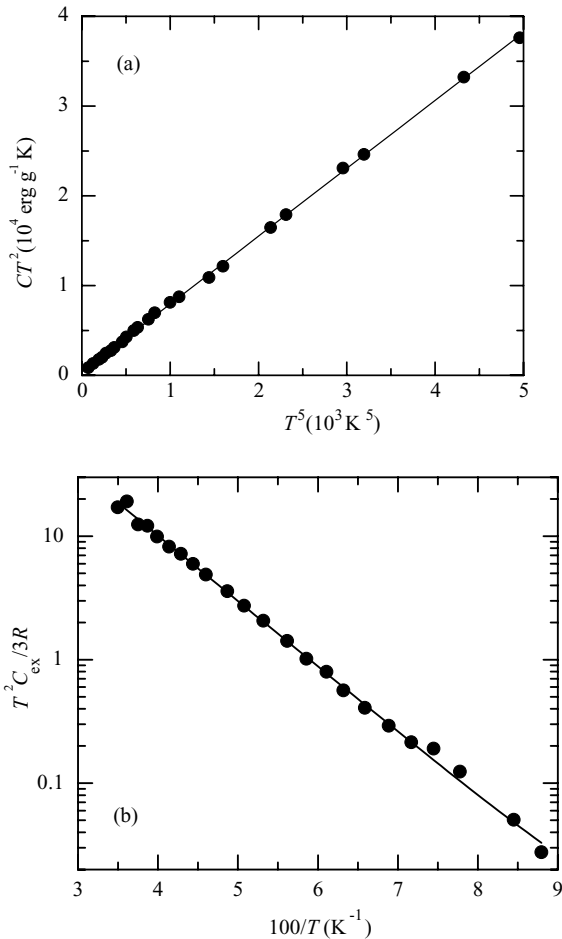


**Figure 1.31** Fit to the pure ZnO data (a) using the Schottky model (with just Schottky and Debye contributions yielding a Debye temperature of 395.5 K) and (b) using the Einstein model.  $C_{\text{ex}}$  is the excess specific heat (ideally the Einstein contribution) obtained by removing the Debye and Schottky contributions from the total specific heat. The Einstein oscillators are identified as the Zn interstitials. (After Ref. [154].)

clamped to prevent thermal expansion or contraction, measurements reveal the “primary” pyroelectric coefficient, which originates from the change in the electric displacement due to internal rearrangements in the structure. However, most of the measurements are carried out under constant stress, meaning that the crystal deformation through thermal expansion is allowed. In this so-called “secondary” effect, the strain induced by thermal expansion alters the electric displacement through the piezoelectric process because all pyroelectric materials are also piezoelectric, such as ZnO. To exhibit pyroelectricity, the material should have no central

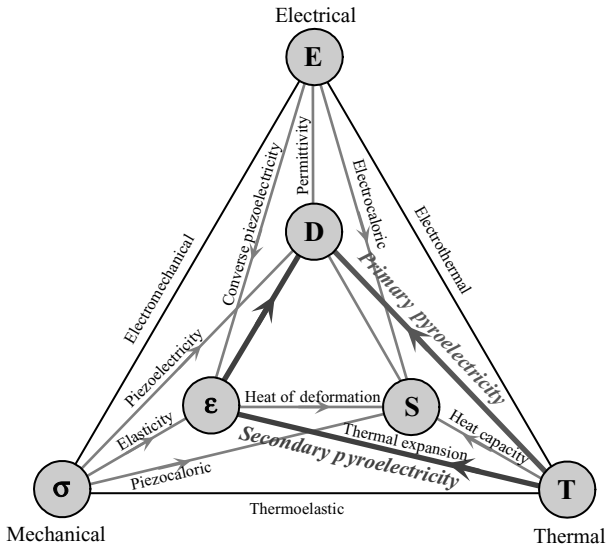


**Figure 1.32** The well-known triangle used to describe the pathways between mechanical, electrical, and thermal energies in a class of noncentrosymmetric materials exhibiting piezoelectric effect, pyroelectric effect (converse of electrocaloric effect), piezocaloric effect (converse of thermal expansion), and so on. For

simplicity, the magnetic property node is not shown. The variables denoted as the nodes are stress ( $\sigma$ ), strain ( $\epsilon$ ), electric field ( $E$ ), displacement ( $D$ ), temperature ( $T$ ), and entropy ( $S$ ). The primary ( $T$  to  $D$ ) and secondary ( $T$  to  $\epsilon$  to  $D$ ) pyroelectric effects are indicated.

symmetry, should have either no axis of rotational symmetry or a single axis of rotational symmetry that is not in an inversion axis, and its molecular structure should have a nonzero dipole moment.

The primary and the secondary pyroelectric effects are indicated in the well-known triangular diagram of Figure 1.32, which describes the pathways between the mechanical, electrical, and thermal energies. Measurement of the primary effect is extremely difficult as it is difficult to prevent the thermal expansion completely. The secondary effect, however, can easily be calculated by using the elastic stiffness and piezoelectric constants and the thermal expansion coefficient. The total (unclamped) pyroelectric coefficient (defined for constant stress as well as constant electric field) is given by the sum of the primary and secondary components and is what is usually measured in experiments. Pyroelectric coefficients measured for various materials are listed in Table 1.11 [155–157]. The pyroelectric effect is stronger in ferroelectric materials, which below a critical temperature, called the Curie temperature, exhibit strong hysteretic electrical polarization, the direction of which can be reversed by an applied electric field. Especially in ferroelectrics, the primary contribution to the pyroelectricity is generally larger than the secondary effect. In nonferroelectric or weakly ferroelectric materials such as ZnO, the pyroelectric coefficients are usually small and correlate well with the specific heat, which is also caused by thermal motions, as illustrated in Figure 1.33. In single-crystal hexagonal ZnO, the electric

**Table 1.11** Primary, secondary, and total (experimentally measured) pyroelectric coefficients (in units of  $\mu\text{C m}^{-2} \text{K}^{-1}$ ) for various materials.

	Primary coefficient	Secondary coefficient	Total (experimental value)
<b>Ferroelectrics</b>			
Poled ceramics			
BaTiO <sub>3</sub>	-260	+60	-200
PbZr <sub>0.95</sub> Ti <sub>0.05</sub> O <sub>3</sub>	-305.7	+37.7	-268
Crystals			
LiNbO <sub>3</sub>	-95.8	+12.8	-83
LiTaO <sub>3</sub>	-175	-1	-176
Pb <sub>5</sub> Ge <sub>3</sub> O <sub>11</sub>	-110.5	+15.5	-95
Ba <sub>2</sub> NaNb <sub>5</sub> O <sub>15</sub>	-141.7	+41.7	-100
Sr <sub>0.5</sub> Ba <sub>0.5</sub> Nb <sub>2</sub> O <sub>6</sub>	-502	-48	-550
(CH <sub>2</sub> CF <sub>2</sub> ) <sub>n</sub>	-14	-13	-27
Triglycine sulfate (TGS)	+60	-330	-270
Pb(Zr <sub>0.54</sub> Ti <sub>0.46</sub> )O <sub>3</sub>			-700
PbTiO <sub>3</sub>			-1250
<b>Nonferroelectrics and weak ferroelectrics</b>			
ZnO	-6.9	-2.5	-9.4
ZnO [157]			-10.5
CdSe	-2.94	-0.56	-3.5
CdS	-3.0	-1.0	-4.0
Tourmaline	-0.48	-3.52	-4.0
Li <sub>2</sub> SO <sub>4</sub> ·2H <sub>2</sub> O	+60.2	+26.1	+86.3

From Refs [155–157].

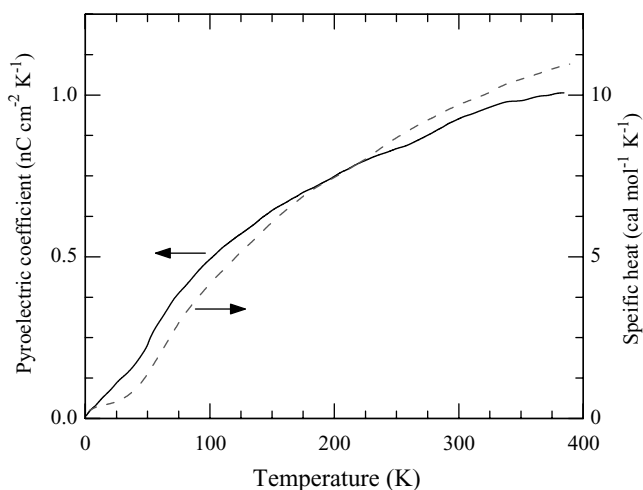


**Figure 1.33** Pyroelectric coefficient and specific heat of ZnO as a function of temperature. (After Ref. [156].)

dipoles formed by the cations and anions add up as all the tetrahedral units point along the *c*-axis.

## 1.7

### Electrical Properties of Undoped ZnO

As a direct and large bandgap material, ZnO is attracting much attention for a variety of electronic and optoelectronic applications. Advantages associated with a large bandgap include high-temperature and high-power operation, lower noise generation, higher breakdown voltages, and ability to sustain large electric fields. The electron transport in semiconductors can be considered for low and high electric fields. (i) At sufficiently low electric fields, the energy gained by the electrons from the applied electric field is small compared to the thermal energy of electrons and therefore the energy distribution of electrons is unaffected by such a low electric field. Because the scattering rates determining the electron mobility depend on the electron distribution function, electron mobility remains independent of the applied electric field, and Ohm's law is obeyed. (ii) When the electric field is increased to a point where the energy gained by electrons from the external field is no longer negligible compared to the thermal energy of the electron, the electron distribution function changes significantly from its equilibrium value. These electrons become hot electrons characterized by an electron temperature larger than the lattice temperature. Furthermore, as the dimensions of the device are decreased to submicron range, transient transport occurs when there is minimal or no energy loss to the lattice during a short and critical period of time, such as during transport under the gate of a field effect transistor or through the base of bipolar transistor. The transient transport is characterized by the onset of ballistic or velocity overshoot phenomenon. Because the electron drift velocity is higher than its steady-state value, one can design a device operating at frequencies exceeding those expected from linear scaling of dimensions.

#### 1.7.1

##### Low-Field Transport

Hall effect is the most widely used technique to measure the transport properties and assess the quality of epitaxial layers. For semiconductor materials, it yields the carrier concentration, its type, and carrier mobility. More specifically, experimental data on Hall measurements over a wide temperature range (4.2–300 K) provide quantitative information on impurities, imperfections, uniformity, scattering mechanisms, and so on. The Hall coefficient and resistivity ( $\rho$ ) are experimentally determined and then related to the electrical parameters through (for n-type conduction)  $R_H = r_H/ne$  and  $\mu_H = R_H/\rho$ , where  $n$  is the free electron concentration,  $e$  is the unit electronic charge,  $\mu_H$  is the Hall mobility, and  $r_H$  is the Hall scattering factor that depends on the particular scattering mechanism. The drift mobility is the average velocity per unit electric field in the limit of zero electric field and is related to the Hall mobility

through the Hall scattering factor by  $\mu_H = r_H \mu$ . As noted above, the Hall scattering factor depends on the details of the scattering mechanism, which limits the drift velocity. In degenerate semiconductors, the Hall factor is unity making the Hall mobility and drift mobility identical such as the case in FETs relying on 2D electron gas. As the carriers travel through a semiconductor, they encounter various scattering mechanisms that govern the carrier mobility in the electronic system. The parameter for characterizing the various scattering mechanisms is the relaxation time  $\tau$ , which determines the rate of change in electron momentum as it moves in the semiconductor crystal. Mobility is related to the scattering time by

$$\mu = \frac{q \langle \tau \rangle}{m^*}, \quad (1.42)$$

where  $m^*$  is the electron effective mass,  $q$  is the electronic charge, and  $\langle \tau \rangle$  is the relaxation time averaged over the energy distribution of electrons. The total relaxation time,  $\tau_T$ , when various scattering mechanisms are operative, is given by Matthiessen's rule:

$$\frac{1}{\tau_T} = \sum_i \frac{1}{\tau_i}, \quad (1.43)$$

where  $i$  represents each scattering process, provided that electron while undergoing one scattering event is not simultaneously affected by another.

The major scattering mechanisms that generally govern the electron transport in III-V semiconductors are also valid for ZnO. They are briefly listed as follows:

- (i) Ionized impurity scattering is due to deflection of free carriers by the long-range Coulomb potentials of the charged centers caused by defects or intentionally doped impurities. This can be thought as a local perturbation of the band edge, which affects the electron motion.
- (ii) Polar longitudinal optical phonon scattering is caused by the interaction of a moving charge with an electric field induced by electric polarization associated with lattice vibration due to ionic nature of the bonds in a polar semiconductor.
- (iii) Acoustic phonon scattering through deformation potential arises from the energy change of the band edges induced by strain associated with acoustic phonons, where the scattering rate increases with the wave vectors of the phonons.
- (iv) Piezoelectric scattering arises from the electric fields that are produced by the strain associated with phonons in a crystal without inversion symmetry.
- (v) If the density of dislocations and native defects are high in a semiconductor, dislocation scattering and scattering through defects are also considered as possible scattering mechanisms. Dislocation scattering is due to the fact that acceptor centers are introduced along the dislocation line, which capture electrons from the conduction band in an n-type semiconductor. The dislocation lines become negatively charged and a space charge region is

formed around it, which scatters electrons traveling across the dislocations, thus reducing the mobility.

Experimental investigation of the temperature-dependent carrier mobility and concentration can be used to determine the fundamental material parameters and understand the carrier scattering mechanisms along with an accurate comparison with theory. Table 1.12 gives the selected best values of electron mobility and corresponding carrier concentration in bulk and thin-film ZnO grown by various techniques. Even today, the electrical properties of ZnO are hard to quantify experimentally due to varying quality of the samples available.

The transport properties reported in the literature are mostly based on Hall effect measurements, assuming the Hall scattering factor to be unity. Using Monte Carlo simulations, Albrecht *et al.* [158] predicted the room-temperature electron mobility of ZnO to be  $\sim 300 \text{ cm}^2 \text{ V}^{-1} \text{ s}^{-1}$ . Nominally undoped ZnO with a wurtzite structure naturally becomes an n-type semiconductor due to the presence of intrinsic or extrinsic defects, which were generally attributed to native defects, such as the Zn-on-O antisite ( $\text{Zn}_\text{O}$ ), the Zn interstitial ( $\text{Zn}_\text{i}$ ) [169], and the O vacancy ( $\text{V}_\text{O}$ ). However, first-principles investigations based on density functional theory suggest that hydrogen in ZnO occurs exclusively in the positive charge state and is responsible for the n-type conductivity of ZnO [131] (discussed in Section 3.3.1). The highest room-temperature electron mobility for a bulk ZnO single crystal grown by vapor-phase transport method is reported to be about  $205 \text{ cm}^2 \text{ V}^{-1} \text{ s}^{-1}$  with a carrier concentration of  $6.0 \times 10^{16} \text{ cm}^{-3}$  [159]. This value is very close to the predicted mobility value. The Hall data obtained as a function of temperature are shown in Figure 1.34. The mobility data were fitted by using Rode's method of solving the Boltzmann transport equation by taking into consideration the major scattering mechanisms, such as polar optical phonon scattering, acoustic phonon scattering through deformation and piezoelectric potentials, and Coulomb scattering from ionized impurities or defects. It was argued that the conduction is dominated by hopping at 8 K due to the carrier freeze-out effect, where the resistivity was measured to be  $2.8 \times 10^4 \Omega \text{ cm}$ . For  $15 \text{ K} < T < 40 \text{ K}$ , the transport was determined by a combination of mixed band and hopping conduction, whereas above 40 K, the data were well fitted by using the usual statistical model (charge-balance equation) involving only the transport in the conduction band. The mobility showed a peak value of about  $2000 \text{ cm}^2 \text{ V}^{-1} \text{ s}^{-1}$  at 50 K.

For the carrier concentration data shown in Figure 1.35, a two-donor charge-balance equation was applied to fit the experimental data:

$$n + N_A = \sum_i \frac{N_{\text{D}i}}{1 + n/\phi_i}, \quad (1.44)$$

where  $\phi_i = (g_{0i}/g_{1i})N'_c \exp(\alpha_i/k)T^{3/2} \exp(-E_{\text{D}0i}/kT)$ , and  $g_{0i}$  ( $g_{1i}$ ) is the unoccupied (occupied) state degeneracy of donor  $i$ . The term  $N'_c$  is the effective conduction band density of states at  $T = 1 \text{ K}$  and  $\alpha_i$  is the temperature coefficient defined by  $E_{\text{D}i} = E_{\text{D}0i} - \alpha_i T$ , where  $E_{\text{D}i}$  is the activation energy of donor  $i$ . Although their origin was left unclear in this work [159], it has been determined that the dominant

**Table 1.12** A compilation of XRD results, electron mobilities, and corresponding carrier concentrations obtained in nominally undoped bulk and thin-film ZnO deposited on different substrates by various growth techniques.

Sample	FWHM of XRD rocking curves (arcsec)	Carrier concentration ( $\text{cm}^{-3}$ )	Electron mobility ( $\text{cm}^2 \text{V}^{-1} \text{s}^{-1}$ )	References
Monte Carlo calculation	—	—	300	[158]
Bulk ZnO grown by vapor-phase transport method	n/a	$6.0 \times 10^{16}$	205	[159]
Bulk ZnO grown by pressurized melt method	49 (0 0 0 2)	$5.05 \times 10^{17}$ (296 K), $3.64 \times 10^{16}$ (77 K)	131 (296 K), 298 (77 K)	[160]
Bulk ZnO grown by hydrothermal method	18 (0 0 0 2)	$8 \times 10^{13}$ (Li compensated)	200	[161]
ZnO thin films grown on <i>c</i> -plane sapphire substrates by PLD	151 (0 0 0 2)	$2.0 \times 10^{16}$	155	[162]
ZnO thin films grown on <i>c</i> -plane sapphire grown by MBE	42 (0 0 0 2)	$1.2 \times 10^{17}$	130	[163]
ZnO thin films grown on <i>a</i> -plane sapphire by MBE	n/a	$7.0 \times 10^{16}$	120	[164]
$\text{Zn}_{0.9}\text{Mn}_{0.1}\text{O}$ /ZnO heterostructure grown on <i>c</i> -plane sapphire by PLD	n/a	$8.8 \times 10^{12}$ (areal concentration $\text{cm}^{-2}$ )	130	[165]
ZnO thin films grown on <i>c</i> -plane sapphire with ZnO/MgO double-buffer layers grown by MBE	18 (0 0 0 2), 1076 (1 0 $\bar{1}$ 1)	$1.2 \times 10^{17}$	145	[166, 167]
ZnO thin films grown on MgZnO-buffered SCAIMgO <sub>4</sub> substrates by PLD	<12 (0 0 0 2), <12 (1 0 $\bar{1}$ 1)	$1 \times 10^{16}$	440	[168]

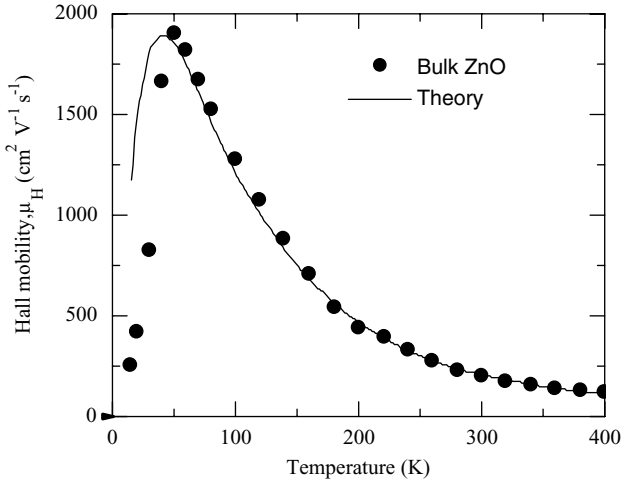


**Figure 1.34** Experimental (circles) and theoretical (solid line) Hall mobility as a function of temperature in bulk ZnO. (After Ref. [159].)

hydrogenic shallow donor had a concentration of about  $1 \times 10^{17} \text{ cm}^{-3}$  and an energy of about 60 meV, whereas the total acceptor concentration was much lower, about  $2 \times 10^{15} \text{ cm}^{-3}$ , resulting in a lower compensation ratio of 0.02. However, the shallower donor that was ruled out due to its smaller concentration (about one order of magnitude less than the deeper donor) at an energy of  $\sim 31 \text{ meV}$  was further investigated later by the same group [169]. They reported that high-energy electron irradiation in ZnO produces shallow donors at about 30 meV. Because the process was found to depend on polarity, where the production rate is much higher for

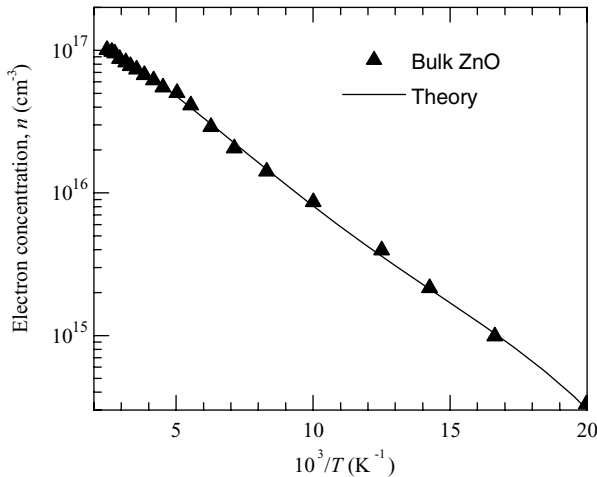


**Figure 1.35** Experimental carrier concentration (triangles) corrected for Hall  $r$ -factor and theoretical fit (solid line) as a function of inverse temperature for bulk ZnO. (After Ref. [159].)

Zn-face  $[000\bar{1}]$  than O-face  $[000\bar{1}]$  irradiation, it has been concluded that this native shallower donor is related to a Zn sublattice defect, most likely the interstitial  $Zn_i$  or a  $Zn_i$ -related complex.

Regarding the ZnO epilayers grown by various growth techniques on different substrates, room-temperature mobilities are relatively poor [170] (typically below  $100\text{ cm}^2\text{ V}^{-1}\text{ s}^{-1}$ ) compared to bulk ZnO, particularly the variety grown by the vapor-phase transport method. However, as listed in Table 1.12, some room-temperature mobility values are comparable to the best reported value for bulk ZnO. Kaidashev *et al.* [162] reported the best reproducible electron mobilities from 115 up to  $155\text{ cm}^2\text{ V}^{-1}\text{ s}^{-1}$  at 300 K in a narrow carrier concentration range from 2 to  $5 \times 10^{16}\text{ cm}^{-3}$  for nominally undoped ZnO thin films of total thickness of 1–2  $\mu\text{m}$  grown on *c*-plane sapphire substrates by a multistep PLD technique. They attributed this success to the multistep PLD process, which includes the insertion of 30 nm thin ZnO relaxation layers deposited at a reduced substrate temperature. The topographical properties of the films were correlated with the corresponding electrical properties. The high-mobility samples showed atomically flat surface structure with grain size of about 0.5–1  $\mu\text{m}$ , whereas the surfaces of low-mobility films consisted of clearly resolved hexagonally faceted columnar grains of only 200 nm size. The observation of the excitonic features in low-temperature photoluminescence spectra also reflects the quality of the samples, which is of primary importance to improve the electrical properties of ZnO.

Kato *et al.* [163] and Iwata *et al.* [164] have performed similar studies on ZnO heteroepitaxial layers grown using plasma-assisted MBE and radical-source MBE techniques. Kato *et al.* [163] used  $(1\bar{1}20)$ -*a*-plane sapphire substrates and high-temperature growth with low-temperature buffer layers for high-quality undoped ZnO epitaxial films. They obtained electron mobilities as high as  $120\text{ cm}^2\text{ V}^{-1}\text{ s}^{-1}$  and residual carrier concentrations as low as  $7 \times 10^{16}\text{ cm}^{-3}$ . With further optimization of the growth condition such as O/Zn flux ratio, a maximum mobility of  $130\text{ cm}^2\text{ V}^{-1}\text{ s}^{-1}$  with a residual carrier concentration of  $1.2 \times 10^{17}\text{ cm}^{-3}$  was reported [171]. It has been suggested that stoichiometric ZnO films have the lowest dislocation density and the highest electron mobility compared to ZnO films grown under nonstoichiometric flux conditions [163]. Iwata *et al.* [164] used ZnO/MgO double-buffer layers for high electron mobility ZnO epilayers grown on *c*-plane sapphire. It has been argued that the precisely controlled low growth rate of the double-buffer layers was crucial for the improvement of electrical properties. The highest electron mobility of  $145\text{ cm}^2\text{ V}^{-1}\text{ s}^{-1}$  in MBE-grown ZnO film was reported at room temperature [166]. This improvement was attributed to a decrease in dislocation density, based on both X-ray diffraction omega rocking curve measurements and calculated electron mobilities.

ZnO-based heterostructures, which contain magnetic impurities in the barrier layer, were grown on *c*-cut sapphire substrates by pulsed laser deposition by Edahiro *et al.* [165]. The temperature dependence of the mobility of the  $Zn_{0.9}Mn_{0.1}O/ZnO$  heterostructure exhibits the suppression of ionized impurity scattering below 100 K as shown in Figure 1.36. The carrier concentration and the mobility measured at 1.85 K are  $4.0 \times 10^{12}\text{ cm}^{-2}$  and  $360\text{ cm}^2\text{ V}^{-1}\text{ s}^{-1}$ , respectively. These transport

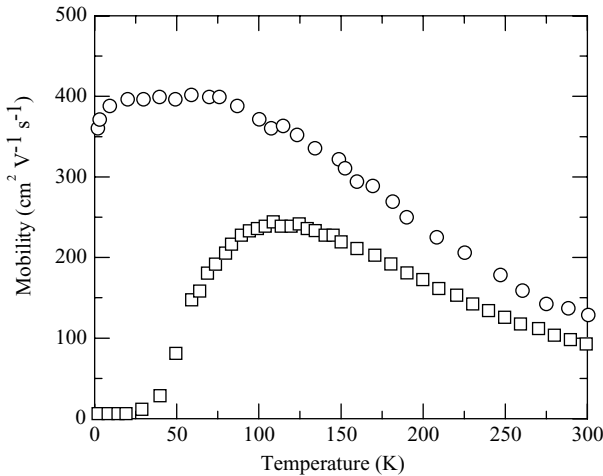


**Figure 1.36** Temperature dependence of the mobility of the ZnMnO/ZnO heterostructure (circles) and the 1  $\mu\text{m}$  thick ZnO single layer (squares) control sample. (After Ref. [165].)

properties revealed that two-dimensional electron gas is successfully formed at the  $\text{Zn}_{0.9}\text{Mn}_{0.1}\text{O}/\text{ZnO}$  interface.

### 1.7.2

#### High-Field Transport

Ensemble Monte Carlo (MC) simulations have been the popular tools to investigate the steady-state and transient electron transport in semiconductors theoretically. In particular, the steady-state velocity field characteristics have been determined using the Monte Carlo method for electric field strengths up to  $350 \text{ kV cm}^{-1}$  in bulk wurtzite structure ZnO at lattice temperatures of 300, 450, and 600 K [158]. The conduction bands of wurtzite-phase ZnO structure were calculated using FP-LMTO-LDA method. For the MC transport simulations, the lowest  $\Gamma$  valley ( $\Gamma_1$  symmetry) and the satellite valleys located at  $\Gamma$  ( $\Gamma_3$  symmetry) and at  $U$  point,  $U_{\min}$  ( $U_1$  symmetry), which is located two-thirds of the way between the  $M$  and  $L$  symmetry points on the edge of the Brillouin zone, have been considered.

The calculated electron drift velocity versus electric field characteristics are plotted in Figure 1.37 for wurtzite-phase ZnO along with GaN for comparison. The first change in the differential mobility curve near  $50 \text{ kV cm}^{-1}$  has been attributed to the onset of significant spontaneous polar optical phonon emission as the electrons are accelerated to energies greater than the longitudinal optical phonon energy of 72 meV. At higher temperatures, this effect reduces and becomes almost negligible at 600 K because the emission and absorption rates are of comparable magnitude at elevated lattice temperatures. With increasing electric field, the drift velocity increases and reaches a peak value of  $3 \times 10^7 \text{ cm s}^{-1}$  at 250 K. Further increase of electric field results in negative differential effect. However, from examination of the

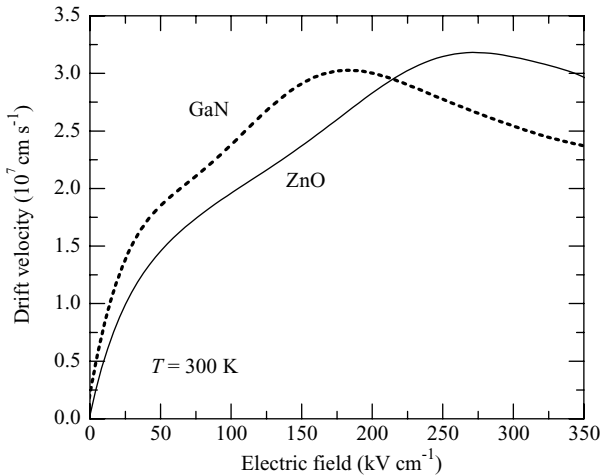


**Figure 1.37** Comparison of calculated electron drift velocity versus electric field for wurtzite structure ZnO (solid) and GaN (dashed) at 300 K. (After Ref. [158].)

electron energy distributions that showed only insignificant transfer of electrons to the higher valleys, the strong decrease of the differential mobility with increasing electric field was attributed to the pronounced nonparabolicity of the central valley. A comparison of the drift velocity of ZnO to the calculated drift velocity of wurtzite GaN although shows comparable peak velocities (see Ref. [91] for details regarding GaN), the peak fields differ considerably, with the peak field for GaN being about  $100 \text{ kV cm}^{-1}$  lower than that of ZnO. It has been argued that this difference arises mainly from the lower satellite valleys in GaN, which have been demonstrated to exhibit a transferred electron effect, and from the stronger Fröhlich coupling in ZnO. Experimental investigations or any other theoretical work related to the high-field transport and energy and momentum relaxation in ZnO are not available in the literature. If the hot phonon effects prevalent in GaN were also to take place in ZnO, which is more than likely, much more refined work is needed on the theoretical side as well to get a representative velocity figure in ZnO at high fields (see Ref. [91] for a detailed discussion of hot phonon effects on heat dissipation and carrier transport).

## References

- 1 Leszczynski, M. (1999) Common crystal structure of the group III-nitrides, in *Properties, Processing and Applications of Gallium Nitride and Related Semiconductors* (eds J.H. Edgar, S. Strite, I. Akasaki, H. Amano and C. Wetzel), *EMIS Databooks Series No. 23*, INSPEC, The Institution of Electrical Engineers, Stevenage, UK, pp. 3–5.
- 2 Ambacher, O., Majewski, J., Miskys, C., Link, A., Hermann, M., Eickhoff, M., Stutzmann, M., Bernardini, F.,

- Fiorentini, V., Tilak, V., Schaff, B. and Eastman, L.F. (2002) Pyroelectric properties of Al(In)GaN/GaN hetero- and quantum well structures. *Journal of Physics: Condensed Matter*, **14**, 3399.
- 3 Leszczynski, M., Suski, T., Perlin, P., Teisseyre, H., Grzegory, I., Bockowski, M., Jun, J., Porowski, S., Pakula, K., Baranowski, J.M., Foxon, C.T. and Cheng, T.S. (1996) *Applied Physics Letters*, **69**, 73.
- 4 Kisi, E. and Elcombe, M.M. (1989) *Acta Crystallographica Section C. Crystal Structure Communications*, **45**, 1867.
- 5 Kogure, T. and Bando, Y. (1993) *Journal of Electron Microscopy*, **47**, 7903.
- 6 Ashrafi, A.B.M.A., Ueta, A., Avramescu, A., Kumano, H., Suemune, I., Ok, Y.-W. and Seong, T.-Y. (2000) *Applied Physics Letters*, **76**, 550.
- 7 Kim, S.-K., Jeong, S.-Y. and Cho, C.-R. (2003) *Applied Physics Letters*, **82**, 562.
- 8 Bates, C.H., White, W.B. and Roy, R. (1962) *Science*, **137**, 993.
- 9 Gerward, L. and Olsen, J.S. (1995) *Journal of Synchrotron Radiation*, **2**, 233.
- 10 Recio, J.M., Blanco, M.A., Luaña, V., Pandey, R., Gerward, L. and Staun Olsen, J. (1998) Compressibility of high-pressure rock salt phase of ZnO. *Physical Review B: Condensed Matter*, **58**, 8949.
- 11 Jamieson, J.C. (1970) *Physics of the Earth and Planetary Interiors*, **3**, 201.
- 12 Desgreniers, S. (1998) High-density phases of ZnO: structural and compressive parameters. *Physical Review B: Condensed Matter*, **58**, 14102.
- 13 Karzel, H., Potzel, W., Köfferlein, M., Schiessl, W., Steiner, M., Hiller, U., Kalvius, G.M., Mitchell, D.W., Das, T.P., Blaha, P., Schwarz, K. and Pasternak, M.P. (1996) *Physical Review B: Condensed Matter*, **53**, 11425.
- 14 Ahuja, R., Fast, L., Eriksson, O., Wills, J.M. and Johansson, B. (1998) *Journal of Applied Physics*, **83**, 8065.
- 15 Recio, J.M., Pandey, R. and Luana, V. (1993) *Physical Review B: Condensed Matter*, **47**, 3401.
- 16 Wilson, M. and Madden, P.A. (1997) *Molecular Physics*, **90**, 75.
- 17 Liu, L.-G. and Bassett, W.A. (1986) *Elements, Oxides and Silicates: High-Pressure Phases with Implications for the Earth's Interior*, Oxford University Press, New York.
- 18 Jaffe, J.E., Snyder, J.A., Lin, Z. and Hess, A.C. (2000) *Physical Review B: Condensed Matter*, **62**, 1660.
- 19 Zaoui, A. and Sekkal, W. (2002) *Physical Review B: Condensed Matter*, **66**, 174106.
- 20 Jaffe, J.E. and Hess, A.C. (1993) *Physical Review B: Condensed Matter*, **48**, 7903.
- 21 Weast, R.C. (1997) *CRC Handbook of Chemistry and Physics*, 58th edn, CRC Press, Boca Raton, FL.
- 22 Bunn, C.W. (1935) *Proceedings of the Physical Society*, **47**, 836.
- 23 Braekken, H. and Jore, C. (1935) *Det Norske Videnskabers Skifter (The Norwegian Science Scripts)*, **NR8**, 1 (in Norwegian).
- 24 Heller, R.B., McGannon, J. and Weber, A.H. (1950) *Journal of Applied Physics*, **21**, 1283.
- 25 Rymer, T.B. and Archard, G.D. (1952) *Research (London)*, **5**, 292.
- 26 Cimino, A., Marezio, M. and Santoro, A. (1957) *Naturwissenschaften*, **12**, 348.
- 27 Gray, T.J. (1954) *Journal of the American Ceramic Society*, **37**, 534.
- 28 Mohatny, G.P. and Azaroff, L.V. (1961) *Journal of Chemical Physics*, **35**, 1268.
- 29 Khan, A.A., (1968) *Acta Crystallographica Section A*, **24**, 403.
- 30 Reeber, R.R. (1970) *Journal of Applied Physics*, **41**, 5063.
- 31 Bond, W.L. (1960) *Acta Crystallographica*, **13**, 814.
- 32 Catti, M., Noel, Y. and Dovesi, R. (2003) *Journal of Physics and Chemistry of Solids*, **64**, 2183.
- 33 Noel, Y., Zicovich-Wilson, C.M., Civalleri, B., D'Arco, Ph. and Dovesi, R. (2001) *Physical Review B: Condensed Matter*, **65**, 014111.

- 34 Himpsel, F.J. (1983) *Advances in Physics*, **32**, 1.
- 35 Rössler, U. (1969) Energy band of hexagonal II–VI semiconductors. *Physical Review*, **184**, 733.
- 36 Langer, D.W. and Vesely, C.J. (1970) *Physical Review B: Condensed Matter*, **2**, 4885.
- 37 Powell, R.A., Spicer, W.E. and McMenamin, J.C. (1971) *Physical Review Letters*, **27**, 97.
- 38 Powell, R.A., Spicer, W.E. and McMenamin, J.C. (1972) *Physical Review B: Condensed Matter*, **6**, 3056.
- 39 Ley, L., Pollak, R.A., McFeely, F.R., Kowalezyk, S.P. and Shirley, D.A. (1974) *Physical Review B: Condensed Matter*, **9**, 600.
- 40 Vesely, C.J., Hengehold, R.L. and Langer, D.W. (1972) *Physical Review B: Condensed Matter*, **5**, 2296.
- 41 Bloom, S. and Ortenburger, I. (1973) *Physica Status Solidi b: Basic Research*, **58**, 561.
- 42 Chelikowsky, J.R. (1977) *Solid State Communications*, **22**, 351.
- 43 Ivanov, I. and Pollmann, J. (1981) *Physical Review B: Condensed Matter*, **24**, 7275.
- 44 Lee, D.H. and Joannopoulos, J.D. (1981) *Physical Review B: Condensed Matter*, **24**, 6899.
- 45 Schröer, P., Krüger, P. and Pollmann, J. (1993) *Physical Review B: Condensed Matter*, **47**, 6971.
- 46 Massidda, S., Resta, R., Posternak, M. and Baldereschi, A. (1995) *Physical Review B: Condensed Matter*, **52**, R16977.
- 47 Schröer, P., Krüger, P. and Pollmann, J. (1994) *Physical Review B: Condensed Matter*, **49**, 17092.
- 48 Vogel, D., Krüger, P. and Pollmann, J. (1995) *Ab initio* electronic-structure calculations for II–VI semiconductors using self-interaction-corrected pseudopotentials. *Physical Review B: Condensed Matter*, **52**, R14316.
- 49 Girard, R.T., Tjernberg, O., Chiaia, G., Söderholm, S., Karlsson, U.O., Wigren, C., Nylén, H. and Lindau, I. (1997) *Surface Science*, **373**, 409.
- 50 Duke, C.B., Lubinsky, A.R., Chang, S.C., Lee, B.W. and Mark, P. (1977) *Physical Review B: Condensed Matter*, **15**, 4865.
- 51 Duke, C.B., Meyer, R.J., Paton, A. and Mark, P. (1978) *Physical Review B: Condensed Matter*, **18**, 4225.
- 52 Wang, Y.R. and Duke, C.B. (1987) *Surface Science*, **192**, 309.
- 53 Göpel, W., Pollmann, J., Ivanov, I. and Reihl, B. (1982) *Physical Review B: Condensed Matter*, **26**, 3144.
- 54 Zwicker, G. and Jacobi, K. (1985) *Solid State Communications*, **54**, 701.
- 55 Ozawa, K., Sawada, K., Shirotori, Y., Edamoto, K. and Nakatake, M. (2003) Angle-resolved photoelectron spectroscopy study of the anion-derived dangling-bond band on ZnO (10  $\bar{1}$  0). *Physical Review B: Condensed Matter*, **68**, 125417.
- 56 Wei, S.H. and Zounger, A. (1988) *Physical Review B: Condensed Matter*, **37**, 8958.
- 57 Martins, J.L., Troullier, N. and Wei, S.H. (1991) *Physical Review B: Condensed Matter*, **43**, 2213.
- 58 Xu, Y.-N. and Ching, W.Y. (1993) *Physical Review B: Condensed Matter*, **48**, 4335.
- 59 Zakharov, O., Rubio, A., Blasé, X., Cohen, M.L. and Louie, S.G. (1994) *Physical Review B: Condensed Matter*, **50**, 10780.
- 60 Lambrecht, W.R.L., Rodina, A.V., Limpijumngong, S., Segall, B. and Meyer, B.K. (2002) *Physical Review B: Condensed Matter*, **65**, 075207.
- 61 Reynolds, D.C., Look, D.C., Jogai, B., Litton, C.W., Cantwell, G. and Harsch, W.C. (1999) Valence band ordering in ZnO. *Physical Review B: Condensed Matter*, **60**, 2340.
- 62 Varshni, Y.P. (1967) *Physica*, **34**, 149.
- 63 Landolt-Börnstein, *Numerical Data and Functional Relationships in Science and Technology*, Vols III/17b and III/41, Springer-Verlag, Berlin.
- 64 Ko, H.J., Chen, Y.F., Zhu, Z., Yao, T., Kobayashi, I. and Uchiki, H. (2000) Photoluminescence properties of ZnO epilayers grown on CaF<sub>2</sub>(1 1 1)

- by plasma assisted molecular beam epitaxy. *Applied Physics Letters*, **76**, 1905.
- 65** Mang, A., Reimann, K. and Rübenacke, St. (1995) *Solid State Communications*, **94**, 251.
- 66** Oshikiri, M., Aryasetiawan, F., Imanaka, Y. and Kido, G. (2002) *Physical Review B: Condensed Matter*, **66**, 125204.
- 67** Cardona, M. (1963) *Journal of Physics and Chemistry of Solids*, **24**, 1543.
- 68** Oshikiri, M., Imanaka, Y., Aryasetiawan, F. and Kido, G. (2001) *Physica B*, **298**, 472.
- 69** Ren, C.-Y., Chiou, S.-H. and Hsue, C.-S. (2004) *Physica B*, **349**, 136.
- 70** Fan, W.J., Abiyasa, A.P., Tan, S.T., Yu, S.F., Sun, X.W., Xia, J.B., Yeo, Y.C., Li, M.F. and Chong, T.C. (2006) *Journal of Crystal Growth*, **287**, 28.
- 71** Karazhanov, S.Zh., Ravindran, P., Grossner, U., Kjekshus, A., Fjellvåg, H. and Svensson, B.G. (2006) *Solid State Communications*, **139**, 391.
- 72** Weiher, R.L. (1966) *Physical Review*, **152**, 736.
- 73** Baer, W.S. (1967) *Physical Review*, **154**, 785.
- 74** Dinges, R., Fröhlich, D., Staginnus, B. and Staude, W. (1970) *Physical Review Letters*, **25**, 922.
- 75** Button, K.J., Cohn, D.R., von Ortenbert, M., Lax, B., Mollwo, E. and Helbig, R. (1972) *Physical Review Letters*, **28**, 1637.
- 76** Landolt-Börnstein (1982) *Numerical Data and Functional Relationships in Science and Technology*, Vol. 22a, Group III (ed. K.-H. Hellwege), Springer-Verlag, Berlin.
- Hümmer, K. (1973) *Physica Status Solidi b: Basic Research*, **56**, 249.
- 77** Oshikiri, M., Tanehaka, K., Asano, T. and Kido, G. (1996) *Physica B*, **216**, 351.
- 78** Imanaka, Y., Oshikiri, M., Takehana, K., Takamasu, T. and Kido, G. (2001) *Physica B*, **298**, 211.
- 79** Shokhovets, S., Gobsch, G. and Ambacher, O. (2006) *Superlattices and Microstructures*, **39**, 299.
- 80** Adachi, S. (2005) *Properties of Group-IV, III-V and II-VI Semiconductors*, John Wiley & Sons, Ltd, West Sussex, UK.
- 81** Jellison, G.E. and Boatner, L.A. (1998) *Physical Review B: Condensed Matter*, **58**, 3586.
- 82** Hill, N.A. and Waghmare, U. (2000) *Physical Review B: Condensed Matter*, **62**, 8802.
- 83** Jaffe, J.E., Pandey, R. and Kunz, A.B. (1991) *Physical Review B: Condensed Matter*, **43**, 14030.
- 84** Hückel, E. (1931) *Zeitschrift für Physik*, **70**, 204.
- 85** Polian, A., Grimsditch, M. and Grzegory, I. (1996) *Journal of Applied Physics*, **79**, 3343.
- 86** Bateman, T.B. (1962) *Journal of Applied Physics*, **33**, 3309.
- 87** Murnaghan, F.D. (1944) *Proceedings of the National Academy of Sciences of the United States of America*, **30**, 244.
- 88** Dal Corso, A., Posternak, M., Resta, R. and Baldereschi, A. (1994) *Physical Review B: Condensed Matter*, **50**, 10715.
- 89** Nye, J.F. (1975) *Physical Properties of Crystals*, Clarendon, Oxford.
- 90** Bernardini, F., Fiorentini, V. and Vanderbilt, D. (1997) *Physical Review B: Condensed Matter*, **56**, R10024.
- 91** Morkoç, H. (2008) *Handbook of Nitride Semiconductors and Devices*, Vol. 1, Wiley-VCH Verlag GmbH, Weinheim.
- 92** Decremps, F., Zhang, J., Li, B. and Liebermann, R.C. (2001) *Physical Review B: Condensed Matter*, **63**, 224105.
- Decremps, F., Pellicer-Porres, J., Marco Saitta, A., Chervin, J.-C. and Polian, A. (2002) High pressure Raman spectroscopy study of wurtzite ZnO. *Physical Review B: Condensed Matter*, **65**, 092101.
- 93** Soga, N. and Anderson, O.L. (1967) *Journal of Applied Physics*, **38**, 2985.
- 94** Kucheyev, S.O., Bradby, J.E., Williams, J.S., Jagadish, C., Toth, M., Phillips, M.R. and Swain, M.V. (2000) *Applied Physics Letters*, **77**, 3373.

- 95 Phillips, J.C. (1973) *Bonds and Bands in Semiconductors*, Academic Press, New York.
- 96 Carlotti, G., Fioretto, D., Socino, G. and Verona, E. (1995) *Journal of Physics: Condensed Matter*, **7**, 9147.
- 97 Carlotti, G., Socino, G., Petri, A. and Verona, E. (1987) *Applied Physics Letters*, **51**, 1889.
- 98 Azuhata, T., Takesada, M., Yagi, T., Shikanai, A., Torii, K., Nakamura, A., Sota, T., Cantwell, G., Eason, D.B. and Litton, C.W. (2003) *Journal of Applied Physics*, **94**, 968.
- 99 Kobiakov, I.B. (1980) *Solid State Communications*, **35**, 305.
- 100 Aoumeur, F.Z., Benkabou, Kh. and Belgoumène, B. (2003) *Physica B*, **337**, 292.
- 101 Kucheyev, S.O., Bradby, J.E., Williams, J.S., Jagadish, C. and Swain, M.V. (2002) *Applied Physics Letters*, **80**, 956.
- 102 Martin, R.M. (1972) *Physical Review B: Condensed Matter*, **5**, 1607.
- 103 Yu, P. and Cardona, M. (1996) *Fundamentals of Semiconductors*, Springer-Verlag, Berlin.
- 104 Gorla, C.R., Emanetoglu, N.W., Liang, S., Mayo, W.E., Lu, Y., Wraback, M. and Shen, H. (1999) Structural, optical, and surface acoustic wave properties of epitaxial ZnO films grown on (0 1 1̄2) sapphire by metalorganic chemical vapor deposition. *Journal of Applied Physics*, **85**, 2595.
- 105 Damen, T.C., Porto, S.P.S. and Tell, B. (1966) *Physical Review*, **142**, 570.
- 106 Arguello, C.A., Rousseau, D.L. and Porto, S.P.S. (1969) *Physical Review*, **181**, 1351.
- 107 Callender, R.H., Sussman, S.S., Selders, M. and Chang, R.K. (1973) *Physical Review B: Condensed Matter*, **7**, 3788.
- 108 Calleja, J.M. and Cardona, M. (1977) *Physical Review B: Condensed Matter*, **16**, 3753.
- 109 Tsuboi, M. and Wada, A. (1968) *Journal of Chemical Physics*, **48**, 2615.
- 110 Porto, S.P.S. and Krishnan, R.S. (1967) *Journal of Chemical Physics*, **47**, 1009.
- 111 Mitra, S.S., Brafman, O., Daniels, W.B. and Crawford, R.K. (1969) *Physical Review*, **186**, 942.
- 112 Cardona, M. (1982) *Light Scattering in Solids II*, in *Springer Topics in Applied Physics*, Vol. 50 (eds M. Cardona and G. Güntherodt), Springer, Berlin, pp. 19–178.
- 113 Stroschio, M.A. and Dutta, M. (2001) *Phonons in Nanostructures*, Cambridge University Press.
- 114 Harima, H. (2002) Properties of GaN and related compounds studied by means of Raman scattering. *Journal of Physics: Condensed Matter*, **14**, R967.
- 115 Koyano, M., QuocBao, P., ThanhBinh, L.T., HongHa, L., NgocLong, N. and Katayama, S. (2002) *Physica Status Solidi a: Applied Research*, **193**, 125.
- 116 Venger, E.F., Melnichuk, A.V., Melnichuk, Lu. and Pasechnik, Yu.A. (1995) *Physica Status Solidi b: Basic Research*, **188**, 823.
- 117 Bundesmann, C., Ashkenov, N., Schubert, M., Rahm, A., Von Wenckstern, H., Kaidashev, E.M., Lorenz, M. and Grundmann, M. (2004) *Thin Solid Films*, **455–456**, 161.
- 118 Manjon, F.J., Mari, B., Serrano, J. and Romero, A.H. (2005) *Journal of Applied Physics*, **97**, 053516.
- 119 Duboz, J.Y. (2002) Hot photoluminescence in GaN: carrier energy relaxation and hot phonon effects. *Journal of Applied Physics*, **92**, 4312.
- 120 Lee, B.C., Kim, K.W., Dutta, M. and Stroschio, M.A. (1997) *Physical Review B: Condensed Matter*, **56**, 997.
- 121 Bairamov, B.H., Heinrich, A., Irmer, G., Toporov, V.V. and Ziegler, E. (1983) *Physica Status Solidi b: Basic Research*, **119**, 227.
- 122 Lu, Y.F., Ni, H.Q. and Ren, Z.M. (2000) *Journal of Applied Physics*, **88**, 498.
- 123 Ashkenov, N., Mbenkum, B.N., Bundesmann, C., Riede, V., Lorenz, M., Spemann, D., Kaidashev, E.M., Kasic, A., Schubert, M., Grundmann, M., Wagner, G., Neumann, H., Darakchieva, V., Arwin,

- H. and Monemar, B. (2003) Infrared dielectric functions of phonon modes of high-quality ZnO films. *Journal of Applied Physics*, **93**, 126.
- 124** Rajalakshmi, M., Arora, A.K., Bendre, B.S. and Mahamuni, S. (2000) *Journal of Applied Physics*, **87**, 2445.
- 125** Minomura, S. (1984) Proceedings of the Ninth AIRAPT International High Pressure Conference on High Pressure in Science and Technology (eds C. Homan, R.K. MacCrane, and E. Whalley), North-Holland, New York, p. 277.
- 126** Limpijumnong, S. and Lambrecht, W.R.L. (2001) *Physical Review Letters*, **86**, 91.
- 127** Serrano, J., Rubio, A., Hernández, E., Muñoz, A. and Mujica, A. (2000) *Physical Review B: Condensed Matter*, **62**, 16612.
- 128** Kaschner, A., Habocek, U., Strassburg, M., Strassburg, M., Kaczmarczyk, G., Hoffmann, A., Thomsen, C., Zeuner, A., Alves, H.R., Hofmann, D.M. and Meyer, B.K. (2002) *Applied Physics Letters*, **80**, 1909.
- 129** Bundesmann, C., Ashkenov, N., Schubert, M., Spemann, D., Butz, T., Kaidashev, E.M., Lorenz, M. and Grundmann, M. (2003) *Applied Physics Letters*, **83**, 1974.
- 130** Manjón, F.J., Mari, B., Serrano, J. and Romero, A.H. (2005) *Journal of Applied Physiology*, **97**, 053516.
- 131** Van de Walle, C.G. (2000) *Physical Review Letters*, **85**, 1012.
- 132** McCluskey, M.D., Jokela, S.J., Zhuravlev, K.K., Simpson, P.J. and Lynn, K.G. (2002) *Applied Physics Letters*, **81**, 3807.
- 133** Lavrov, E.V., Weber, J., Börrnert, F., Van de Walle, C.G. and Helbig, R. (2002) *Physical Review B: Condensed Matter*, **66**, 165205.
- 134** Lavrov, E.V. (2003) *Physica B*, **340–342**, 195.
- 135** Jokela, S.J., McCluskey, M.D. and Lynn, K.G. (2003) *Physica B*, **340–342**, 221.
- 136** Nickel, N.H. and Fleischer, K. (2003) Hydrogen local vibrational modes in zinc oxide. *Physical Review Letters*, **90**, 197402.
- 137** Wolk, J.A., Ager, J.W., III, Duxstad, K.J., Haller, E.E., Taskar, N.R., Dorman, D.R. and Olego, D.J. (1993) *Applied Physics Letters*, **63**, 2756.
- 138** Ibach, H. (1969) *Physica Status Solidi*, **33**, 257.
- 139** Touloukina, Y.S., Kirby, R.K., Taylor, R.E. and Lee, T.Y. (1977) *Thermal Expansion. Thermal Properties of Matter*, Vol. 13, Plenum, New York.
- 140** Iwanaga, H., Kunishige, A. and Takeuchi, S. (2000) Anisotropic thermal expansion in wurtzite-type crystals. *Journal of Materials Science*, **35**, 2451.
- 141** Han, M.-Y. and Jou, J.-H. (1995) *Thin Solid Films*, **260**, 58.
- 142** Bhandari, C.M. and Rowe, D.M. (1988) *Thermal Conduction in Semiconductors*, John Wiley & Sons, Inc., New York.
- 143** Kittel, C. (1986) *Introduction to Solid State Physics*, 6th edn., John Wiley & Sons, Inc., New York, p. 150.
- 144** Florescu, D.I., Asnin, V.M., Pollak, F.H., Molnar, R.J. and Wood, C.E.C. (2000) *Journal of Applied Physics*, **88**, 3295.
- 145** Florescu, D.I., Asnin, V.M., Pollak, F.H., Jones, A.M., Ramer, J.C., Schurman, M.J. and Ferguson, I. (2000) *Applied Physics Letters*, **77**, 1464.
- 146** Florescu, D.I., Mourokh, L.G., Pollak, F.H., Look, D.C., Cantwell, G. and Li, X. (2002) *Journal of Applied Physics*, **91**, 890.
- 147** Özgür, Ü., Gu, X., Spradlin, J., Cho, S.-J., Morkoç, H., Pollak, F.H., Nemeth, B. and Nause, J. (2006) *Journal of the Electrochemical Materials*, **85**, 550.
- 148** Olorunoyemi, T., Birnboim, A., Carmel, Y., Wilson, O.C., Jr and Lloyd, I.K. (2002) *Journal of the American Ceramic Society*, **85**, 1249.
- 149** Tsubota, T., Ohtaki, M., Eguchi, K. and Arai, H. (1997) *Journal of Materials Chemistry*, **7**, 85.
- 150** Ohtaki, M., Tsubota, T., Eguchi, K. and Arai, H. (1996) *Journal of Applied Physics*, **79**, 1816.
- 151** Katsuyama, S., Takagi, Y., Ito, M., Majima, K., Nagai, H., Sakai, H., Yoshimura, K.

- and Kosuge, K. (2002) *Journal of Applied Physics*, **92**, 1391.
- 153** Tsubota, T., Ohtaki, M. and Eguchi, K., Arai, H. (1998) *Journal of Materials Chemistry*, **8**, 409.
- 153** Cai, K.F., Müller, E., Drašar, C. and Mrotzek, A. (2003) *Materials Science and Engineering B*, **104**, 45.
- 154** Lawless, W.N. and Gupta, T.K. (1986) *Journal of Applied Physics*, **60**, 607.
- 155** Zook, J.D. and Liu, S.T. (1973) Pyroelectric effects in thin film. *Journal of Applied Physics*, **49**, 4604.
- 156** Newnham, R.E. (2005) *Properties of Materials: Anisotropy, Symmetry, Structure*, Oxford University Press, New York.
- 157** Ye, C.-P., Tamagawa, T. and Polla, D.L. (1991) Experimental studies on primary and secondary pyroelectric effects in Pb ( $Zr_xTi_{1-x}$ )O<sub>3</sub>, PbTiO<sub>3</sub>, and ZnO thin films. *Journal of Applied Physics*, **70**, 5538.
- 158** Albrecht, J.D., Ruden, P.P., Limpijumngong, S., Lambrecht, W.R.L. and Brennan, K.F. (1999) *Journal of Applied Physics*, **86**, 6864.
- 159** Look, D.C., Reynolds, D.C., Sizelove, J.R., Jones, R.L., Litton, C.W., Cantwell, G. and Harsch, W.C. (1998) *Solid State Communications*, **105**, 399.
- 160** Nause, J. and Nemeth, B. (2005) *Semiconductor Science and Technology*, **20**, S45.
- 161** Maeda, K., Sato, M., Niikura, I. and Fukuda, T. (2005) *Semiconductor Science and Technology*, **20**, S49.
- 162** Kaidashev, E.M., Lorenz, M., Von Wenckstern, H., Rahm, A., Semmelhack, H.-C., Han, K.-H., Benndorf, G., Bundesmann, C., Hochmuth, H. and Grundmann, M. (2003) *Applied Physics Letters*, **82**, 3901.
- 163** Kato, H., Sano, M., Miyamoto, K. and Yao, T. (2003) *Japanese Journal of Applied Physics, Part 1: Regular Papers, Short Notes & Review Papers*, **42**, 2241.
- 164** Iwata, K., Fons, P., Niki, S., Yamada, A., Matsubara, K., Nakahara, K. and Takasu, H. (2000) *Physica Status Solidi a: Applied Research*, **180**, 287.
- 165** Edahiro, T., Fujimura, N. and Ito, T. (2003) *Journal of Applied Physics*, **93**, 7673.
- 166** Miyamoto, K., Sano, M., Kato, H. and Yao, T. (2004) *Journal of Crystal Growth*, **265**, 34.
- 167** Cho, M.V., Setiawan, A., Ko, K.J., Hong, S.K. and Yao, T. (2005) *Semiconductor Science and Technology*, **20**, S13.
- 168** Ohmoto, A. and Tsukazaki, A. (2005) *Semiconductor Science and Technology*, **20**, S1.
- 169** Look, D.C., Hemsley, J.W. and Sizelove, J.R. (1999) *Physical Review Letters*, **82**, 2552.
- 170** Ginley, D.S. and Bright, C. (2000) *Materials Research Bulletin*, **25**, 15.
- 171** Miyamoto, K., Sano, M., Kato, H. and Yao, T. (2002) *Japanese Journal of Applied Physics, Part 2: Letters*, **41**, L1203.